

**SAKARYA UNIVERSITY
INSTITUTE OF SCIENCE AND TECHNOLOGY**

**SIMULATION STUDY OF COSMIC MUONS
IN THE EARTH'S ATMOSPHERE AND
UNDERGROUND USING GEANT4**

Ph.D. THESIS

Halil ARSLAN

Department : PHYSICS

Supervisor : Prof. Dr. Mehmet BEKTASOGLU

January 2015

SAKARYA UNIVERSITY
INSTITUTE OF SCIENCE AND TECHNOLOGY

**SIMULATION STUDY OF COSMIC MUONS
IN THE EARTH'S ATMOSPHERE AND
UNDERGROUND USING GEANT4**

Ph.D. THESIS

Halil ARSLAN

Department : PHYSICS

This thesis has been unanimously accepted by the examination committee on the date January 20th, 2015.

**Prof. Dr.
Mehmet BEKTASOGLU
Chair of the Committee**



**Prof. Dr.
Ilhan TAPAN**



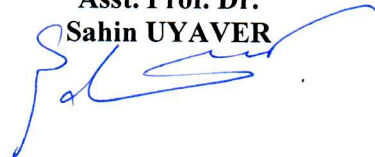
**Prof. Dr.
Mehmet OZEN**



**Assoc. Prof. Dr.
Ali Serdar ARIKAN**



**Asst. Prof. Dr.
Sahin UYAYER**



ACKNOWLEDGEMENTS

I would like to first thank my advisor Prof. Mehmet Bektasoglu for his extraordinary support during all phases of my graduate work. I want to also express my deep and sincere gratitude to him for his great efforts to explain things clearly, for giving me the freedom to find my own way in my study, and for always being kind, supportive and patient towards me.

My special thanks go to my wife and children for their patience and support. Their encouragement has always been a key motivation throughout my graduate studies.

Some of the numerical calculations reported in this dissertation have been performed at TUBITAK ULAKBIM, High Performance and Grid Computing Center (TRUBA Resources).

This dissertation is partially funded by Sakarya University Scientific Research Projects Coordination Department (Project Number: 2012-50-02-033).

TABLE OF CONTENTS

ACKNOWLEDGEMENTS	ii
TABLE OF CONTENTS	iii
LIST OF FIGURES.....	vi
LIST OF TABLES.....	xi
ABSTRACT.....	xii
ÖZET	xiii
CHAPTER 1.	
INTRODUCTION.....	1
CHAPTER 2.	
COSMIC RAYS	3
2.1. A Brief History of Cosmic Rays	3
2.2. General Properties of Cosmic Rays	8
2.2.1. Energy spectra of the primaries	8
2.2.2. Chemical composition.....	14
2.2.3. Their origin	19
2.3. Cosmic Rays in the Earth's Atmosphere.....	22
2.4. Effects of the Magnetic Fields on Cosmic Rays	25
2.4.1. Heliospheric magnetic fields.....	25
2.4.2. Geomagnetic fields	29
2.5. Effects of the Cosmic Rays	32
2.5.1. Effects on the human health.....	32
2.5.2. Effects on the atmosphere	34
2.5.3. Effects on the electronic devices.....	36
2.5.4. Usage of cosmic rays	36

CHAPTER 3.

MUONS	38
3.1. Discovery of the Muon	38
3.2. General Properties of the Muon	42
3.2.1. Energy loss of muons in matter.....	46
3.2.2. Cosmic ray muons.....	49
3.3. Cosmic Muons at Ground Level	50
3.3.1. Angular dependence of the muon intensity.....	54
3.3.2. Muon charge ratio	58
3.4. Cosmic Muons in the Atmosphere	60
3.5. Underground Muons	62
3.5.1. Depth-intensity relation.....	64
3.5.2. Angular dependence of underground muon intensity	67

CHAPTER 4.

GEANT4 MONTE CARLO SIMULATION TOOLKIT	69
4.1. Monte Carlo Method.....	69
4.2. Geant4 Simulation Package	71
4.2.1. Geometry and materials	72
4.2.2. Particles in Geant4	74
4.2.3. Geant4 physics models	75
4.2.3.1. Electromagnetic interaction models.....	75
4.2.3.2. Hadronic interaction models	76
4.2.3.3. Cuts	79

CHAPTER 5.

SIMULATION	80
5.1. Model of the Earth's Atmosphere	80
5.1.1. Earth's atmosphere.....	80
5.1.2. Atmosphere model	84
5.1.3. Electromagnetic fields	85
5.2. Models for the Earth's Crust	86
5.2.1. Standard rock	86

5.2.2. Slanic salt mine	87
5.3. Primary Particles	89
5.4. Physics Models	91
CHAPTER 6.	
RESULTS AND DISCUSSION	93
6.1. Cosmic Muons at Ground Level	93
6.1.1. Muon spectrum and charge ratio.....	93
6.1.2. Relation to the parent primaries	95
6.1.3. Zenith angle dependence of the muon intensity.....	100
6.1.4. Azimuth angle dependence of the muon charge ratio	109
6.2. Cosmic Muons in the Atmosphere	113
6.2.1. Flux variations with the altitude	113
6.2.2. Zenith angle dependences in the atmosphere.....	116
6.3. Underground Muons	118
6.3.1. Muon intensities in a salt mine	118
6.3.2. Zenith angle dependence of muon intensities in a salt mine	121
6.3.3. Muon intensities at various depths in standard rock	123
6.3.4. Zenith angle dependence of muon intensities in standard rock ..	125
CHAPTER 7.	
CONCLUSION	127
REFERENCES.....	129
RESUME.....	145

LIST OF FIGURES

Figure 2.1. Schematic view (left) and photograph (right) of the Wulf's electroscope. In the schematic view; Q: quartz fibres, B: amber for electrical isolation, J: container for the metallic rod to charge the fibres, F: microscope to measure the fibre distance, S: mirror, E: windows.....	4
Figure 2.2. Ion density rates as a function of the balloon height measured by Hess and Kolhörster	5
Figure 2.3. Track of the positron in a cloud chamber operated in a strong magnetic field.....	7
Figure 2.4. Differential energy spectrum of all the charged cosmic ray particles	9
Figure 2.5. The all-particle spectrum multiplied by $E^{2.7}$	11
Figure 2.6. Energy of cosmic protons with different initial energies as a function of propagation distance	13
Figure 2.7. The all-particle spectrum of primary cosmic rays multiplied by E^3 from AGASA and the HiRes experiments	13
Figure 2.8. The relative abundances of elements (He – Ni) in cosmic rays (solid circles: low energy data, open circles: high energy data) and the solar system (open diamonds).....	15
Figure 2.9. Differential energy spectra of the primary cosmic H, He, C and Fe nuclei	16
Figure 2.10. Fractions of some typical cosmic ray elements relative to the total differential intensity as a function of energy per nucleon	17
Figure 2.11. The mean logarithmic mass number of the primary cosmic rays as a function of the energy.....	18
Figure 2.12. Some examples for the orbits of the charged cosmic rays affected by the Earth's magnetic field	20
Figure 2.13. Development of an air shower in the Earth's atmosphere.....	22

Figure 2.14. Vertical fluxes of cosmic rays in the atmosphere with energies above 1 GeV as a function of altitude. Markers show the measured negative muon fluxes	24
Figure 2.15. A sketch of the solar magnetic field in the ecliptic plane	26
Figure 2.16. Cosmic ray variations as a function of time indicating the Forbush Effect	26
Figure 2.17. Cosmic ray intensity and 10.7 cm solar flux variation in years 1951–2006.....	28
Figure 2.18. Galactic cosmic proton spectra obtained from the PAMELA experiment performed between the years 2006 and 2009.....	29
Figure 2.19. a) Magnetic field lines of the Earth near the surface b) Earth's magnetosphere shaped by the solar winds.....	30
Figure 2.20. The differential energy spectra of protons at different values of the geomagnetic cut-off (G) obtained in the PAMELA experiment	31
Figure 3.1. The decay of π -meson observed in a photographic emulsion.....	40
Figure 3.2. The decay chain of $\pi \rightarrow \mu \rightarrow \eta$ in photographic emulsion where η represents the electron	41
Figure 3.3. The Feynman diagram for the muon decay	42
Figure 3.4. Experimental points and theoretical curve for the momentum spectrum of the positron in the decay of μ^+	43
Figure 3.5. Disintegration curves for positive and negative muons in aluminum ...	45
Figure 3.6. Some measurements and calculation results for the energy spectrum of the cosmic muons at the ground	51
Figure 3.7. BESS results for the negative and positive muon spectra at two different locations.....	52
Figure 3.8. BESS results for the annual variation of the muon flux in Lynn Lake	53
Figure 3.9. Momentum spectrum of muons with zenith angle $\theta = 75^\circ$ (blank diamonds) and those of the vertical muons (the rest of the markers)....	55
Figure 3.10. Monte Carlo calculations of the ratio of the inclined muon flux to the vertical muon flux at ground level as a function of cosine of the zenith angle for different muon momenta.....	56

Figure 3.11. The azimuthal angular dependence of the muon fluxes for the zenith angles $40^\circ \pm 5^\circ$ for different momentum intervals. Open and full triangular markers represent the positive and negative muon flux respectively. The circular marker is for the total flux, and the dashed lines are the fit curves.....	57
Figure 3.12. Experimental muon charge ratio as a function of the muon momentum.....	58
Figure 3.13. The azimuthal dependence of the muon charge ratio for zenith angles 20° and 40° in the momentum range $1 - 2 \text{ GeV}/c$	59
Figure 3.14. Momentum spectra of negative muons for several atmospheric depths. Solid lines are the fit to power law	61
Figure 3.15. Muon flux as a function of the atmospheric depth for different momentum ranges	62
Figure 3.16. Vertical intensity of underground muons as a function of depth	65
Figure 3.17. Local differential energy spectra of the underground muons at various depths. Each spectrum was normalized to the vertical muon intensity at the corresponding depth	66
Figure 3.18. Variation of the exponent as a function of depth below the top of the atmosphere.....	68
Figure 4.1. The time for solution of the problems, depending on their complexity, using the Monte Carlo method and analytic approach.....	70
Figure 4.2. Several geometrical shapes defined in Geant4 simulation package.....	73
Figure 4.3. Some of the hadronic models used in Geant4	76
Figure 4.4. Energy intervals of QGSP_BERT for various particles.....	78
Figure 5.1. Change in the atmospheric pressure depending on the altitude	81
Figure 5.2. Thermal structure of the atmosphere up to 140 km altitude.....	82
Figure 5.3. Geant4 view of the atmosphere model consisting of 100 layer, each having 1 km of thickness.....	84
Figure 5.4. An artistic representation of the Slanic salt mine.....	87
Figure 5.5. Schematic drawing of the Unirea mine	88
Figure 5.6. A Geant4 representation of a part of the Unirea mine.....	89
Figure 5.7. Energy spectra of the primary protons used in the simulation and the BESS measurement results.....	90

Figure 5.8. Ground level muon distributions; measurements by Rastin and primaries used in the simulations	91
Figure 5.9. Visualization of the cosmic ray shower inside the modeled atmosphere.....	92
Figure 6.1. Geant4 simulation outputs for the vertical differential momentum spectra of muons in Lynn Lake and Tsukuba together with the experimental values	94
Figure 6.2. The simulated and experimental muon charge ratios as a function of muon momentum in Tsukuba.....	95
Figure 6.3. Interrelation between the zenith angles of the sea level muons and those of their parent primaries for threshold muon momenta 1 GeV/c (left) and 10 GeV/c (right).....	96
Figure 6.4. Response curves as a function of the primary proton energy for $E_\mu=1$ GeV, 14 GeV and 100 GeV.....	97
Figure 6.5. E_{median}/E_μ as a function of the threshold energy for the vertical muons	98
Figure 6.6. E_{median}/E_μ as a function of the threshold energies for the muons with different zenith angles	99
Figure 6.7. Muon counting rates measured using a Berkeley Lab cosmic ray detector and the normalized output from the Geant4 simulation	101
Figure 6.8. Geant4 simulation output for muon events as a function of the zenith angle	102
Figure 6.9. Simulation results for the muon counts as a function of the zenith angle for mean momenta 1–40 GeV/c in the western azimuth of Calcutta ..	103
Figure 6.10. Simulated values of the exponent n for the western and eastern azimuths in Calcutta, together with the experimental ones for the West at the same location as a function of the muon momentum.....	105
Figure 6.11. Simulation results for the muon counts as a function of zenith angle for mean momenta 1–40 GeV/c in the western azimuth of Melbourne....	106
Figure 6.12. Simulated values of the exponent n for the western and eastern azimuths in Melbourne, together with the experimental ones for the same azimuths as a function of the muon momentum.....	108

Figure 6.13. The simulated and experimental azimuth angle dependence of the charge ratio of low-energy cosmic muons reaching the ground with the mean momentum of 0.5 GeV/c	110
Figure 6.14. Muon charge ratio in the western and eastern directions below 1 GeV/c as a function of the muon momentum	111
Figure 6.15. The East–West asymmetry of the muon charge ratio below 1 GeV/c as a function of the muon momentum	112
Figure 6.16. Momentum spectra of the atmospheric muons at various atmospheric depths.....	113
Figure 6.17. Fluxes of vertical muons above 0.58 GeV/c as a function of the atmospheric depth.....	114
Figure 6.18. Muon charge ratios at various atmospheric depths as a function of the muon momentum.....	115
Figure 6.19. Muon charge ratios for two momentum intervals as a function of atmospheric depth.....	116
Figure 6.20. The exponent n as a function of the atmospheric depth for different muon momenta	117
Figure 6.21. Ground level momentum distributions of the muons reaching various depths in salt.....	118
Figure 6.22. Flux of nearly vertical muons at two different levels of the Cantacuzino mine	119
Figure 6.23. Flux of nearly vertical muons at the Unirea mine	120
Figure 6.24. Muon intensities for site of the Slanic salt mine as a function of the zenith angle.....	122
Figure 6.25. The simulated normalized local spectra of the underground muons in various depths of standard rock.....	123
Figure 6.26. Integrated intensity of the underground muons in standard rock as a function of depth	124
Figure 6.27. The exponent n as a function of depth in standard rock.....	126

LIST OF TABLES

Table 2.1. Spectral indices of some primary cosmic elements.....	17
Table 2.2. Decay modes of some unstable particles and their probabilities	23
Table 2.3. Average annual radiation exposure from the natural sources	33
Table 3.1. Mean lifetimes of the μ^- in several materials	46
Table 3.2. The energy loss parameters α and β calculated for standard rock.....	47
Table 3.3. Best-fit for differential and integral muon spectra for the vertical direction.....	50
Table 3.4. Average of the rock parameters ρ , Z/A and Z^2/A for several underground sites.....	63
Table 5.1. Calculated geomagnetic field components and cut-off rigidities at various experimental sites	85
Table 6.1. Calculated and simulated $E_{\text{median}}/E_{\mu}$ ratios for two different muon threshold energies.....	98
Table 6.2. Simulated and measured values of the exponent n for Calcutta in different azimuths.....	104
Table 6.3. Simulated and measured values of the exponent n for Melbourne in different azimuths.....	107
Table 6.4. Simulated and measured fluxes at Unirea mine and at the two levels of the Cantacuzino mine	121
Table 6.5. The experimental and simulated parameters obtained from the fits to the Fréjus function.....	125

ABSTRACT

Keywords: Cosmic rays, Muon, Monte Carlo simulation, Geant4

In this dissertation, cosmic muon properties, such as the intensity, charge ratio and angular dependence, at sea level, at different altitudes in the Earth's atmosphere and various underground depths have been investigated using the Geant4 simulation package.

The energy spectrum and charge ratio of the sea level muons have been obtained for different geomagnetic locations. Energy and zenith angular distributions for parent primaries of the muons with different threshold energies, in addition to the angular dependence of muon intensities, have also been estimated for the ground level. Secondly, altitude dependent profiles of the muon spectra and charge ratios, together with the zenith angular dependence of muon intensities, have been obtained in this study. Finally, intensities and their zenith angular dependence have been investigated for underground muons at various depths of the standard rock and several levels of a salt mine.

The results obtained throughout this study have been found to be in general agreement with the available experimental data. The simulation studies have also been extended to describe the cases that have not been covered by the experiments.

DÜNYA ATMOSFERİ VE YER ALTINDAKİ KOZMİK MÜONLARIN GEANT4 SİMÜLASYON PROGRAMI İLE İNCELENMESİ

ÖZET

Anahtar kelimeler: Kozmik ışınlar, Müon, Monte Carlo simülasyonu, Geant4

Bu tezde, deniz seviyesi, Dünya atmosferinin farklı yükseltileri ve yer altındaki kozmik müonlara ait akı, yük oranı ve açısal bağlılık gibi özellikler Geant4 simülasyon programından yararlanılarak incelenmiştir.

Deniz seviyesindeki müonların enerji spektrumları ve yük oranları farklı bölgeler için elde edilmiştir. Farklı eşik enerjili müonları oluşturan birincil protonların enerji ve açısal dağılımlarına ek olarak müon akısının zenit açığı ve yük oranının azimut açığına bağlılıkları yine bu kısımda araştırılmıştır. Bunlara ek olarak, muon spektrumu, yük oranı ve zenit açığı bağımlılığının yerden yüksekliğe bağlı değişimleri de incelenmiştir. Son olarak, yer altına ulaşan müonlara ait akı ve zenit açığı bağımlılıkları standart kaya yapısının çeşitli derinlikleri ve bir tuz madeninin farklı seviyeleri için ayrı ayrı elde edilmiştir.

Çalışmanın her bir aşamasında elde edilen simülasyon sonuçlarının, benzer koşullarda elde edilmiş olan deneysel sonuçlarla uyumlu olduğu görülmüştür. Bu uyuma dayanarak, simülasyon çalışması deneysel verilerin olmadığı bazı durumları da içerecek şekilde genişletilmiştir.

CHAPTER 1. INTRODUCTION

Cosmic rays are very energetic charged particles that bombard the Earth's atmosphere. Protons and alpha particles are the main constituents of these particles. The origins of the cosmic rays are not fully known. However there are some predictions and categorizations based on their energies. Interactions of these cosmic particles with the nuclei in the atmosphere produce a large number of particles, which are mostly unstable mesons decaying into muons and neutrinos.

Cosmic rays had been used for the particle physics experiments before the particle accelerators were invented. First generations of the subatomic particles were mainly discovered by studying the cosmic rays' tracks left on the photographic films. Although many particle physics studies have been moved to the accelerator laboratories, cosmic rays are still extremely important for the field since their interactions with the atmospheric nuclei may occur in the kinematic regions that cannot be covered with the accelerator energies available today. As a field of interest in astrophysics, the origins and the acceleration mechanisms of the high energy cosmic rays are currently the subjects of much intense discussions.

Since the muon measurements are appropriate to determine the properties of the primary cosmic rays and to test the atmospheric neutrino flux calculations, many experiments have been carried out at various ground level and underground sites. In addition to the experiments, Monte Carlo simulations of the propagations and interactions of cosmic rays, based on the present knowledge on interactions, decays, and particle transport in matter, are also utilized to study the detailed cosmic ray shower development.

In this dissertation, cosmic muon properties in the Earth's atmosphere, at sea level and underground have been studied using the Geant4 simulation package, which uses the Monte Carlo methods. The contents of each chapter are briefly given below.

Chapter 2 in this thesis provides general information on the cosmic rays starting with a brief history followed by the description of the energy spectra, compositions and predictions on the origins of the primary cosmic rays. Then, the effects of the geomagnetic and heliospheric magnetic fields on the primaries are discussed. In addition, secondary particle production by the interactions of the primaries with the atmospheric nuclei is also handled in this chapter. Chapter 3 discusses general properties of the muons in addition to the cosmic muon distributions at ground level, in the atmosphere and underground separately. For ground level muons, the energy spectrum, charge ratio and dependence of the intensity on the zenith and azimuth angles are presented. For atmospheric and underground muons, changes in the intensities depending on the depth are also described. In Chapter 4, details of the Geant4 simulation toolkit are given together with a brief explanation of the Monte Carlo method. Chapter 5 introduces the models for the Earth's atmosphere and crust constructed using Geant4 in order to study the atmospheric and underground muons. Primary particle distributions and the selected physics models to describe the interactions in the simulations are also given in this chapter. Chapter 6 presents the simulation outputs obtained in this study under three sub categories, which contain the results for the cosmic muons at the ground, in the atmosphere and underground separately. Available experimental data are also provided in this chapter for comparison with the corresponding simulation results. Finally, a short summary of the results obtained in this study is given in Chapter 7.

CHAPTER 2. COSMIC RAYS

Cosmic rays are very high energy particles originated from the outer space and continuously bombard the Earth's atmosphere from almost all directions. They are dominantly ionized nuclei (~90% protons, ~9% alpha particles and the rest heavier nuclei [1]), in addition to very little electrons and positrons. Although most of them are relativistic (having energies somewhat greater than their rest mass energies), very rare of them have ultra-high energies ($>10^{18}$ eV). A particle detected by the Utah Fly's Eye cosmic-ray detector with an energy of 3×10^{20} eV is the highest energy cosmic ray ever recorded [2]. In order to realize the greatness of this energy, one should note that the human made accelerators constructed using current technologies are able to reach at most $10^{12} - 10^{13}$ eV energies [3]. Although the origins of cosmic rays and how they accelerate to such amazing energies are still not exactly known, there are some predictions and categorizations based on their energies.

2.1. A Brief History of Cosmic Rays

In the early 20th century, radioactivity and the related conductivity of air were intensely studied using the *electrometer* as the standard instrument. At those times, it was already known that an electrometer in the vicinity of a radioactive source would be discharged when radioactivity ionizes the gases inside the electrometer.

In 1900, C. T. R. Wilson [4] and J. Elster, together with H. Geitel [5], found out independently from each other that the electrometers away from a source of ionizing rays were still discharged at a slower rate. The losing charge of the electrometers was attributed to the small quantities of radioactive substances like pollutions embedded in the walls of the electrometer and in the surrounding environment. These findings gave way to investigations aiming at the understanding of the origin of that unknown ionizing radiation.

In 1907, T. Wulf invented a portable electrometer which enabled scientists to carry the search for the origin of the unknown radiation out of the laboratory. The schematic drawing and photograph of the Wulf's electroscope are shown in Figure 2.1. Wulf measured the radiation both at the base and the top of the Eiffel Tower. Assuming that the radiation was coming from the Earth's crust, decrease in the radiation was expected as getting away from the ground. However, he observed a smaller reduction in radiation at the top (at 300 m altitude) with respect to the theoretical estimates [6].

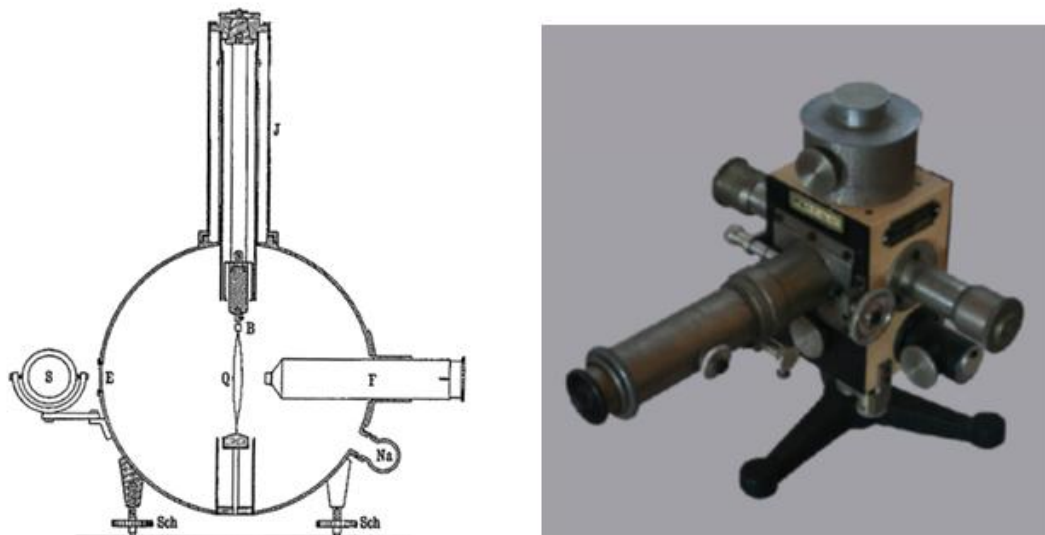


Figure 2.1. Schematic view (left) and photograph (right) of the Wulf's electroscope [7]. In the schematic view; Q:quartz fibres, B:amber for electrical isolation, J:container for the metallic rod to charge the fibres, F:microscope to measure the fibre distance, S:mirror, E:windows

In 1912, V. Hess performed radiation measurements using an enhanced version of Wulf's electrometer during the balloon flights up to the height of 5350 m. Hess performed the measurements with three independent electrometers during the flight. The electrometers used by Hess were isolated such that particle density inside the apparatus was kept constant, in spite of the change in the temperature and pressure during the balloon ascent. It was observed that intensity of the radiation causing air ionization at the height of ~5 km was several times higher than the one at ground level. This finding refuted the idea that the mentioned radiation results from the radioactive emanation from the ground. Furthermore, no significant decrease in the

radiation was observed during the night or solar eclipse, with the moon blocking most of the Sun's visible radiation. Hess concluded his observations by an assumption that a radiation with high penetration power enters the Earth's atmosphere from a source in the space apart from the Sun [8]. This discovery of Hess was awarded by Nobel Prize in physics in 1936 [9].

The measurements were extended by W. Kolhörster to higher altitudes. He performed the measurements in balloon flights up to altitudes exceeding 9 km above sea level. His observations clearly demonstrated an increase of the radiation intensity with increasing altitude [10], which confirmed that radiation has an extraterrestrial origin as originally suggested by Hess. Measurement results of Hess, together with the ones of Kolhörster, for the ion density rates as a function of balloon height are illustrated in Figure 2.2.

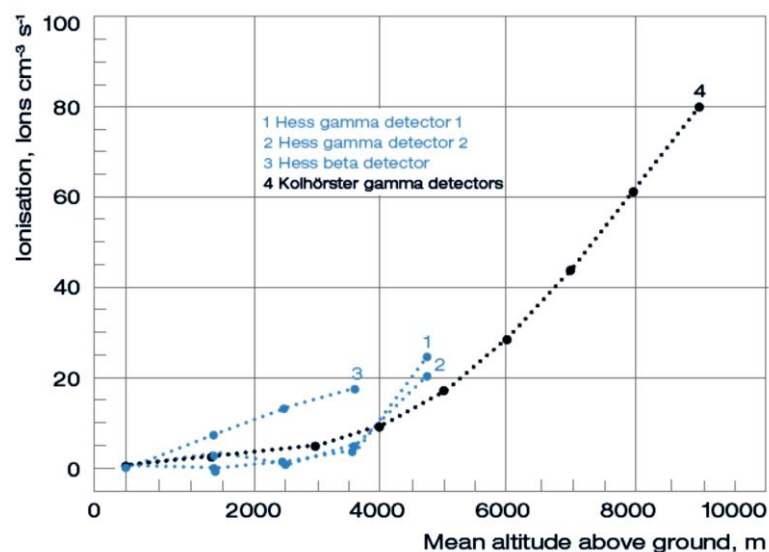


Figure 2.2. Ion density rates as a function of the balloon height measured by Hess and Kolhörster [11]

In 1926, R. Millikan and H. Cameron, based on their measurements from deep underwater to high altitudes, suggested that the radiations coming from the space were gamma rays (energetic photons). Moreover, they called the radiation as “*cosmic ray*” [12]. However, in 1927, J. Clay observed a variation in the intensity of the cosmic rays with geomagnetic latitude such a way that fewer cosmic rays arrive at the equatorial region [13]. This observation yielded the idea that the cosmic rays

entering the Earth's atmosphere are composed of charged particles and they are affected by the Earth's magnetic field. Although it was made clear that the radiation consists of particles, the name "ray" has not been given up.

In 1930, B. Rossi predicted that if the charges of cosmic rays entering the atmosphere were mainly one kind, there should have been a difference in the intensities measured from the eastern and western directions [14]. Then, some other researchers (T. H. Johnson [15], L. Alvarez and A. H. Compton [16]), in addition to Rossi [17], measured that the intensity of the cosmic rays coming from the western direction was greater than the one from the eastern direction. This directional asymmetry of the cosmic ray intensity, called the *East–West effect*, shows the cosmic radiation to be predominantly positively charged.

In 1939, P. Auger discovered that cosmic radiation events reach the ground level more or less simultaneously on very large scale. Based on this observation, Auger concluded that such events were associated with a single event, and called this cosmic ray induced particle showers as the *extensive air showers*. In other words, a particle shower could be produced when a very high energy particle from the space strikes into the Earth's atmosphere and interacts with the nuclei of the atmospheric gases. In addition, Auger estimated from the number of particles in the shower that energy of the incoming particle creating large air showers to be at least 10^{15} eV [18].

At the end of the 1930s, M. Schein and his coworkers made cosmic ray measurements in a series of balloon flights and determined that the cosmic radiation bombarding the Earth's atmosphere consists of mostly protons [19]. In the late 1940s, observations with photographic emulsions and cloud chambers carried by balloons near the top of the atmosphere showed the existence of nuclei of some atoms, such as helium (alpha particle), carbon and iron, in cosmic radiation [20, 21]. However, since the cosmic radiation that enters the atmosphere consists of only a very small fraction of electrons, they could not be directly detected until 1961 [22].

Observations of cosmic ray particles using cloud chambers near the ground were enabled the scientists to discover new kinds of particles. For example,

C. D. Anderson recognized the tracks of a particle that is positively charged twin of the electron in 1932, and he named it as the *positron* [23]. The track left in the cloud chamber by the first positron observed in cosmic rays is shown in Figure 2.3. The positron enters the chamber from below, which can be understood from the stronger bending of the track after having passed through the lead plate in the middle of the chamber because of the energy loss. Since the direction of the magnetic field in which the chamber was placed is pointing into the page, it was concluded that the particle must have been positively charged. Moreover, Anderson was able to find from the curvature of the track that the mass of the particle was close to that of the electron.

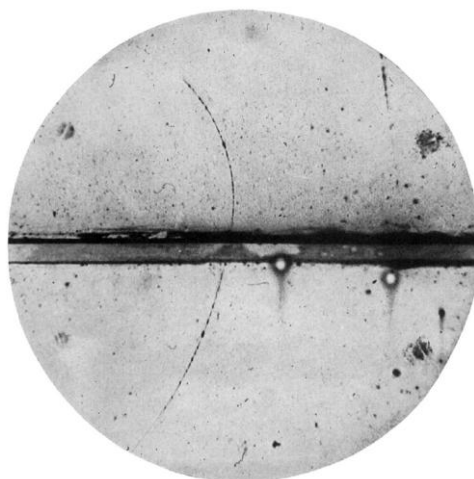


Figure 2.3. Track of the positron in a cloud chamber operated in a strong magnetic field [23]

Discovery of positron, whose existence was theoretically predicted by P. Dirac [24] previously, was awarded by the Nobel Prize in physics, together with the discovery of V. Hess [9], in 1936. Furthermore, Anderson, together with S. Neddermeyer, also discovered the *muon* while studying the tracks left in the cloud chambers by the cosmic rays in 1937 (details on the discovery of muons are given in Section 3.1). Positron and muon are the first of series of subatomic particles discovered, and their discoveries can be accepted as the birth of elementary particles physics science. After their discovery, some other elementary particles, such as pion, were discovered during cosmic ray researches (for details on the subject see, for example, [25]).

Cosmic rays were used for the research of elementary particle physics until the invention of particle accelerators in 1950s. With the movement of particle physics studies to the accelerator laboratories, cosmic ray studies started to take place in the field of astrophysics. Nevertheless, cosmic rays are still extremely important in particle physics since they are accelerated to extremely high energies in a huge “natural laboratory”.

2.2. General Properties of Cosmic Rays

Cosmic ray particles bombard the Earth’s atmosphere with the rate of arrival nearly 1000 per square meter per second [1]. Collisions of the cosmic rays with the atmospheric nuclei result in the production of new energetic particles. Some of these particles are able to reach the Earth’s surface and even deep underground. High energy cosmic particles accelerated in astrophysical sources are known as the *primary cosmic rays*. Namely, protons, alpha particles (helium nuclei) and heavier nuclei such as carbon and iron generated in stars are the primaries. On the other hand, the particles produced by the interaction of these primaries with the gas molecules in the interstellar media (or in the Earth’s atmosphere) are called as the *secondary cosmic rays*. In addition to some nuclei like lithium, beryllium and boron, unstable particles like pion and muon can be given as the examples of the secondaries.

2.2.1. Energy spectra of the primaries

Cosmic rays bombarding the Earth’s atmosphere have an enormous energy range, from about hundred MeV to greater than 10^{20} eV. The rate of the cosmic rays reaching the top of the atmosphere depends heavily on their energies such that the low energy ones are plentiful and the higher energy ones are rare. Differential energy spectrum, which is defined as the number of particles per unit area, per unit time, per unit solid angle and per unit energy, is the way of representing the intensities of the cosmic rays for each energy interval. The differential energy spectrum of all the cosmic ray charged particles is shown as a compilation in Figure 2.4.

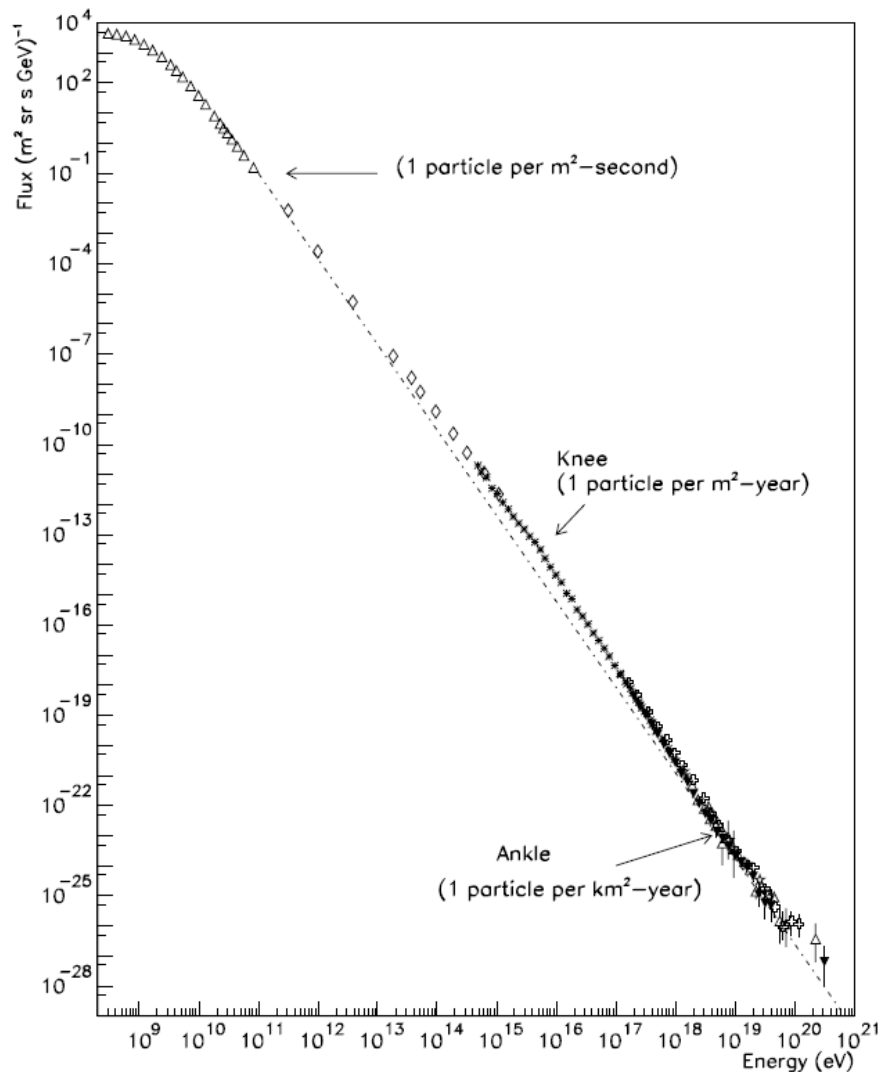


Figure 2.4. Differential energy spectrum of all the charged cosmic ray particles [26]

It can be seen from the figure that the spectrum decreases fast with increasing energy. While one cosmic particle per square meter per second bombards the atmosphere at $\sim 10^{11}$ eV energy, this rate decreases to only one particle per square meter per year for particles with energies between 10^{15} and 10^{16} eV, and one particle per square kilometer per year between 10^{18} and 10^{19} eV energy. Recent studies showed that the flux of the primaries with energies above 10^{19} eV is extremely low, in the order of one particle per square kilometer per century [27].

The energy spectrum and composition of the cosmic radiation up to the energy of $\sim 10^{14}$ eV were determined using the data from the balloon-borne measurements at the top of the Earth's atmosphere as well as the satellite measurements well outside

the atmosphere. In each case, primary cosmic ray data were collected by *direct measurements* using variety of detection systems since the flux of particles is sufficiently high. For higher energies, where the intensity is extremely low, direct measurements of the primaries are no longer practical. Therefore, *indirect methods* are used in order to get the information about such primaries. Interaction of the primary cosmic rays having energies greater than 10^{14} eV with the nuclei present in the air produces secondary cascades. These secondaries (extensive air shower) reach the ground in a broad range of area, and they can be measured by an array of detectors with dimensions of a fraction of a kilometer square. Based on the measurements performed using such detection systems, the energy and the nature of the primaries initiating the secondary cascade can be determined.

Flux of the primary cosmic rays reaches the maximum at the low energy region where the spectrum is flatter. Flux of the particles with lower energies ($< \sim 10$ GeV) is affected strongly by the solar winds and the 11 year solar cycle, known as the *solar modulation*. Therefore, the low energy part of the spectrum given in Figure 2.4 is valid for a particular date and the exact intensity at low energy changes continuously depending on the measurement date. At kinetic energies above ~ 10 GeV, the differential energy spectrum of primary the particles is well described by an inverse *power law* of the form

$$I(E) \propto E^{-\gamma}, \quad (2.1)$$

where I is the intensity, E is the kinetic energy per nucleon and γ is the spectral index of the power law. The value of γ is approximately 2.7 for all the nuclei with energies up to $\sim 4 \times 10^{15}$ eV, where the spectrum starts to steepen, and the spectral index reaches a value of ~ 3.1 for higher energies. The region that the slope of the spectrum changes was discovered in 1958 [28], and named as the *knee*. The spectrum flattens again above $\sim 4 \times 10^{18}$ eV energy, and this part of the spectrum is called the *ankle*, which was first realized in 1963 [29]. Furthermore, there has been some evidence for the existence of another feature, called the *second knee*, at $\sim 4 \times 10^{17}$ eV, where the spectrum exhibits a second steepening [30]. All-particle spectrum of the cosmic rays,

which is multiplied by a factor $E^{2.7}$ in order to emphasize the existence of the knee and the ankle, plotted in double logarithmic scale is shown in Figure 2.5. For the region $\gamma = 2.7$, the spectrum lies along the horizontal axis, and any change in the spectral index results in a rapid deviation from the horizontal.

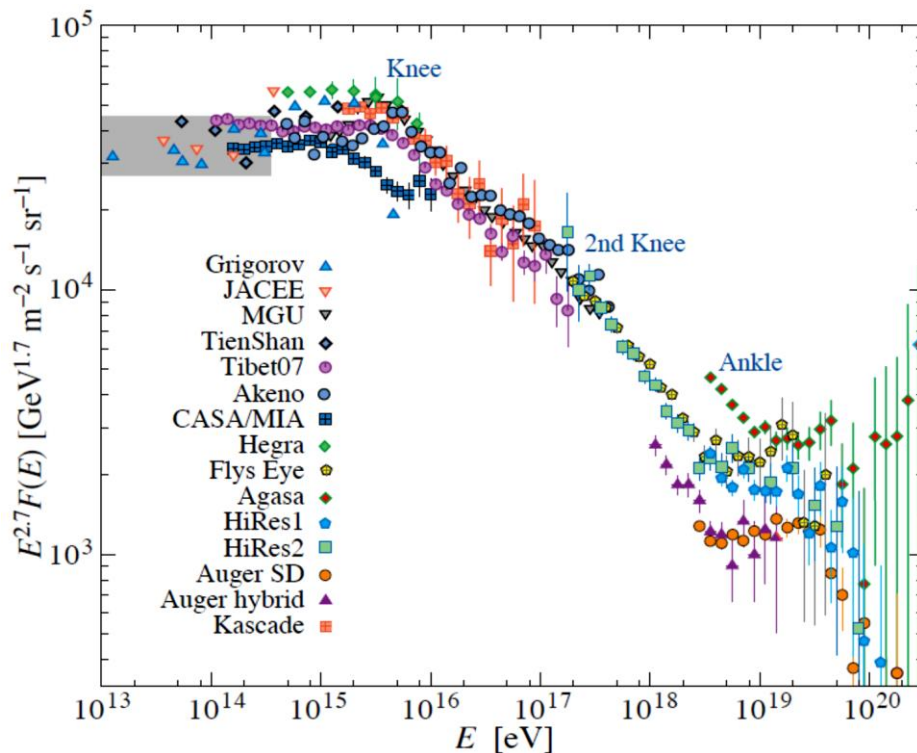


Figure 2.5. The all-particle spectrum multiplied by $E^{2.7}$ (see [31] and references therein)

Although many measurements have been made and many theories have been developed on the issue, the cause of these spectral index changes is still under discussion [32]. It is believed that this phenomenon will be clarified with the understanding of the primary particles' origins and acceleration mechanisms, which are still unclear. However, common to all the models is the prediction of a change of composition over the knee region. It is known that some constituents of the primary cosmic rays have different energy spectra such that their spectra drop more rapidly at high energies. As a result, the superposition of the spectra of different kind of primaries, which yields the all-particle spectrum, shows such an irregularity. Furthermore, flattening of the spectrum above the ankle is attributed to the transition from particles of galactic origin to those accelerated in extra-galactic sources.

For cosmic rays, a maximum energy of $\sim 5 \times 10^{19}$ eV is predicted from the calculations of K. Greisen [33]. G. T. Zatsepin and V. A. Kuz'min have also predicted the same maximum energy independently [34]. According to the theory, which is called the *Greisen–Zatsepin–Kuzmin (GZK) limit*, the extragalactic flux of protons with energies above the mentioned limit would be sharply reduced and the spectrum steepens abruptly. The reason for that behavior is that the protons with sufficient energy interact with the photons of the cosmic microwave background (CMB) radiation, which is the thermal radiation left over from the Big Bang. Collisions between the cosmic protons and the photons often result in the production of pions (π) via the decay of the Δ resonance according to



and



Minimum energy of the cosmic ray protons to produce this interaction was calculated to be $\sim 5 \times 10^{19}$ eV concerning the energy of the microwave photons. For every collision with the CMB photons, the cosmic ray protons lose energy.

The mean energies of the cosmic protons (with initial energies of 10^{20} eV, 10^{21} eV and 10^{22} eV) as a function of propagation distance are illustrated in Figure 2.6. It can be seen from the figure that the mean energy becomes essentially independent of the initial energy of the protons after travelling a distance of ~ 100 Mpc (Mega parsec) and reaches a value less than 10^{20} eV. (Note that parsec is an astronomical unit of distance with 1 pc is equal to 3.26 light years.) Therefore, it is expected to see very few cosmic rays above the GZK cut-off energy. Observation of the particles with energies higher than the GZK cut-off is attributed to the sources closer than ~ 100 Mpc. Getting rid of the GZK cut-off for cosmic rays may also imply new physics.

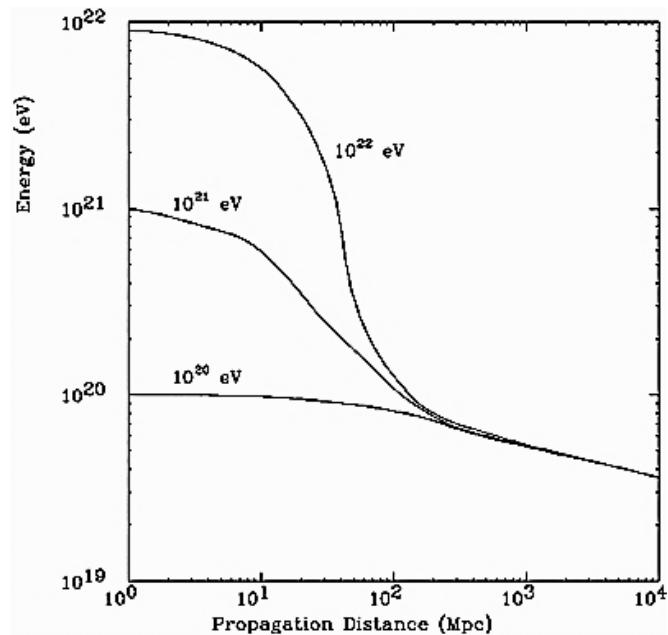


Figure 2.6. Energy of cosmic protons with different initial energies as a function of propagation distance [35]

It is still one of the most discussed questions in particle astrophysics whether the GZK cut-off exists or not. Although no GZK suppression has been observed in the measurement results of the *Akeno Giant Air Shower Array* (AGASA) [36, 37], the *High Resolution Fly's Eye* (HiRes) experiment observed the GZK cut-off with a statistical significance of five standard deviations [38]. The cosmic ray energy spectrum measured by the HiRes detectors, together with the one obtained in AGASA experiment, is illustrated in Figure 2.7.

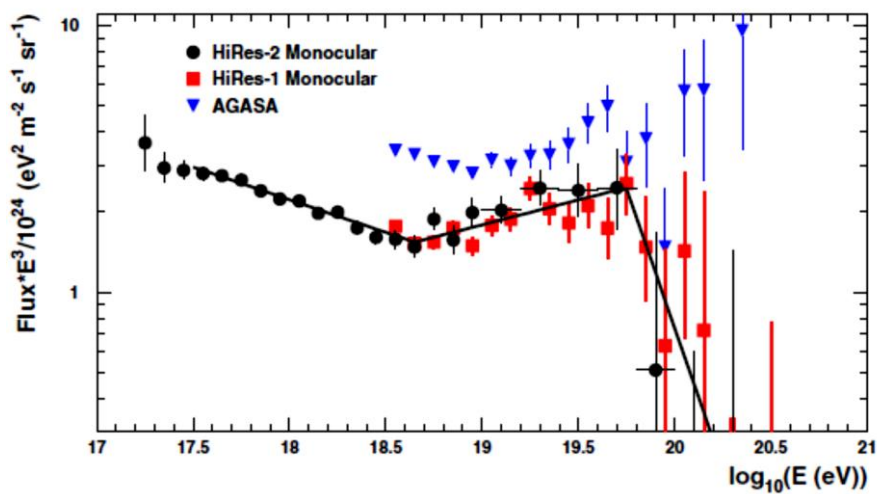


Figure 2.7. The all-particle spectrum of primary cosmic rays multiplied by E^3 from AGASA [37] and the HiRes [38] experiments

Later on, the Pierre Auger Observatory collaboration supported the HiRes results on the GZK cut-off [39]. However, more information on the mass spectrum and higher statistics are needed for a better understanding of the issue in the highest energy region.

2.2.2. Chemical composition

The chemical composition of the primary cosmic radiation is relatively well known at lower energies. However, because of the low counting rates and correspondingly of the large statistical errors, the information on the composition of the high energy cosmic rays is limited. According to the present knowledge that is experimentally confirmed, primary cosmic radiation with lower energies consists mostly of protons and alpha particles, in addition to little percentage ($\sim 1\%$) of the heavier elements up to the actinides.

The relative abundances of the elements (from H to Ni) in cosmic rays and in the solar system are shown in Figure 2.8. In the figure, the solid and open circles represent the low ($70 - 280 \text{ MeV}/n$) and high ($1000 - 2000 \text{ MeV}/n$) energy per nucleon data respectively, and the open diamonds are for the solar system.

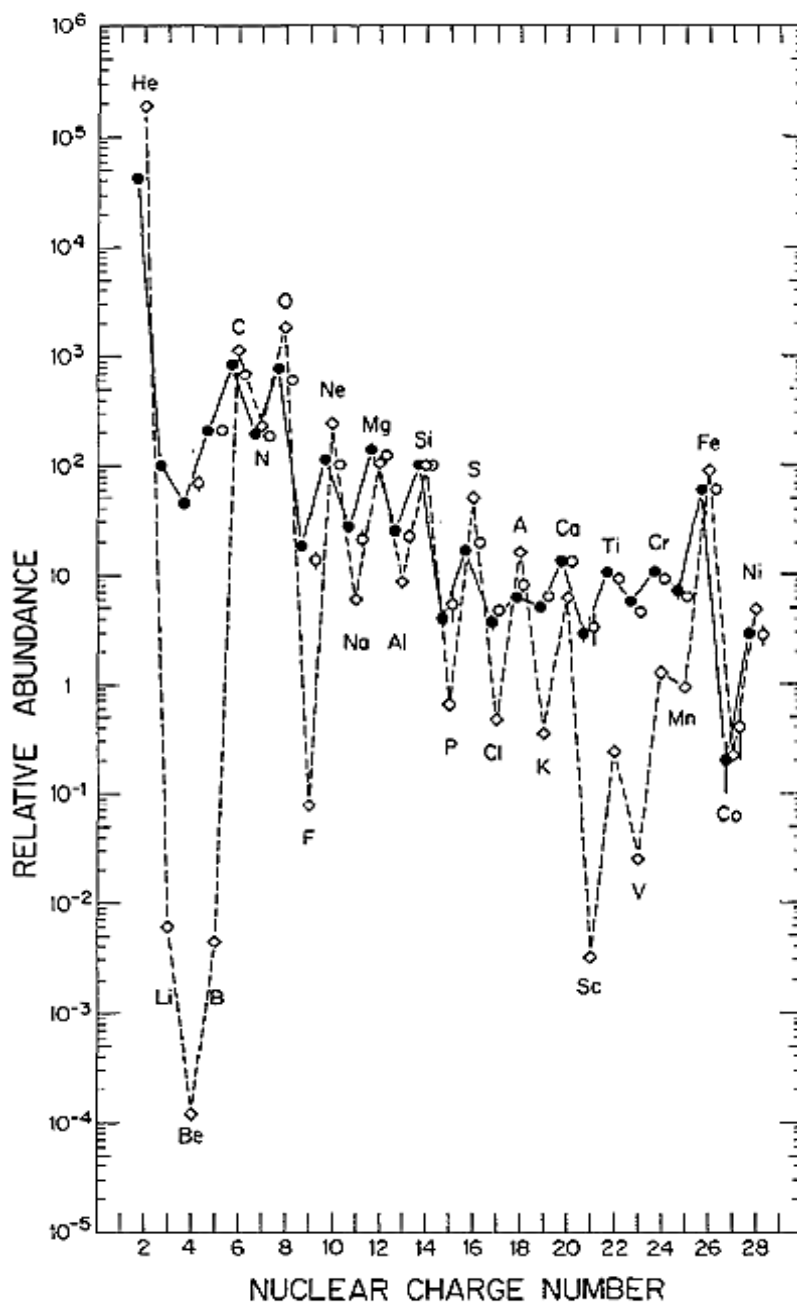


Figure 2.8. The relative abundances of elements (He – Ni) in cosmic rays (solid circles: low energy data, open circles: high energy data) and the solar system (open diamonds) [40]

Both cosmic rays and the solar system abundances show the *odd–even effect* such that the nuclei with even charge number are relatively more abundant because of their more tightly bound nuclear structure compared to those with odd charge number. Considering that the cosmic rays have similar elemental structure to those of the outer space, one can conclude that chemical composition of the extraterrestrial matter sample shows features similar to the elemental abundances in the solar

system. In spite of the similarities between the relative abundances of both cosmic rays and the solar system, two groups of elements, namely a group consisting of Li, Be and B, and the other one consisting of Sc, Ti, V, Cr and Mn, are much more abundant in the cosmic rays. Wealth of the mentioned elements in the cosmic radiation results from the fact that some of them are produced by the collisions of cosmic particles like C, O and Fe with the nuclei of the interstellar gas.

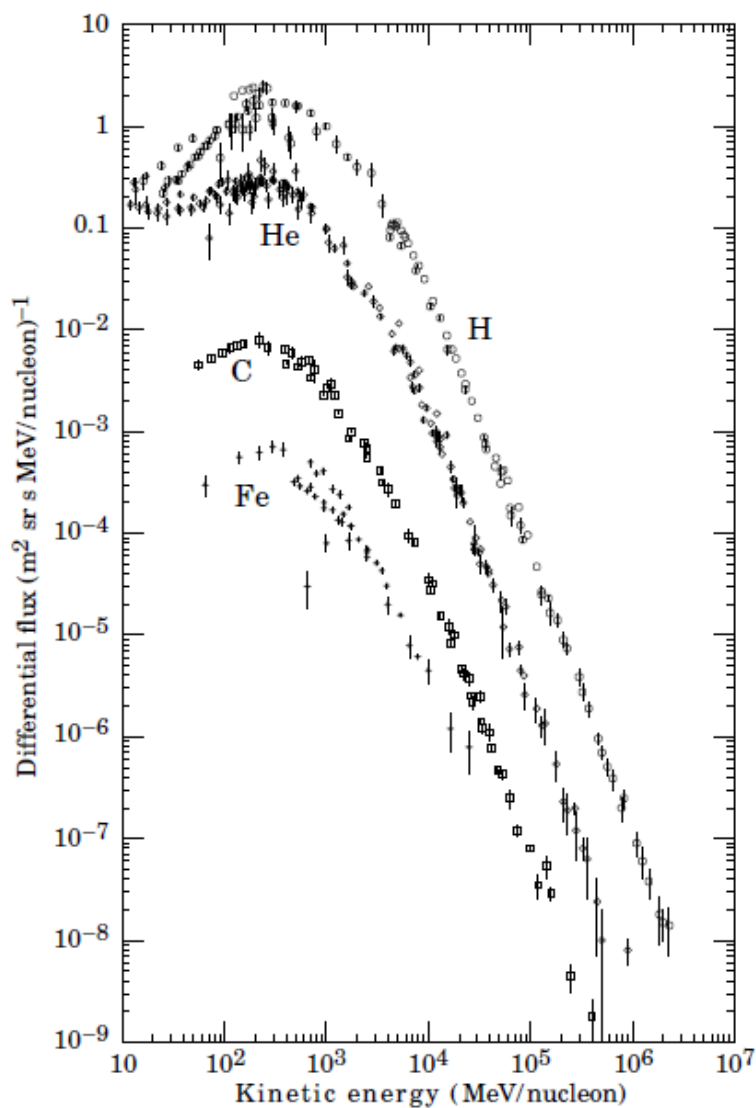


Figure 2.9. Differential energy spectra of the primary cosmic H, He, C and Fe nuclei [40]

Differential energy spectra of the major components (H, He, C and Fe) of the primary cosmic rays are illustrated in Figure 2.9. All the spectra in the figure follow the power law given by the relation (2.1) for the energies above $10Z$ GeV, where the

Z is the charge number. The spectral indices (γ) for some of the individual nuclei are given in Table 2.1.

Table 2.1. Spectral indices of some primary cosmic elements [41]

Element	Z	Γ
H	1	2.77 ± 0.02
He	2	2.64 ± 0.02
C	6	2.66 ± 0.02
Fe	26	2.60 ± 0.09
Ni	28	2.51 ± 0.18

It is seen that while the spectral index of the protons (H nuclei) is ~ 2.77 , heavier elements have somewhat smaller indices. Different spectral slopes show that the abundances of lighter elements such as proton and He decrease at higher energy, while heavier ones, particularly Fe, increase considerably.

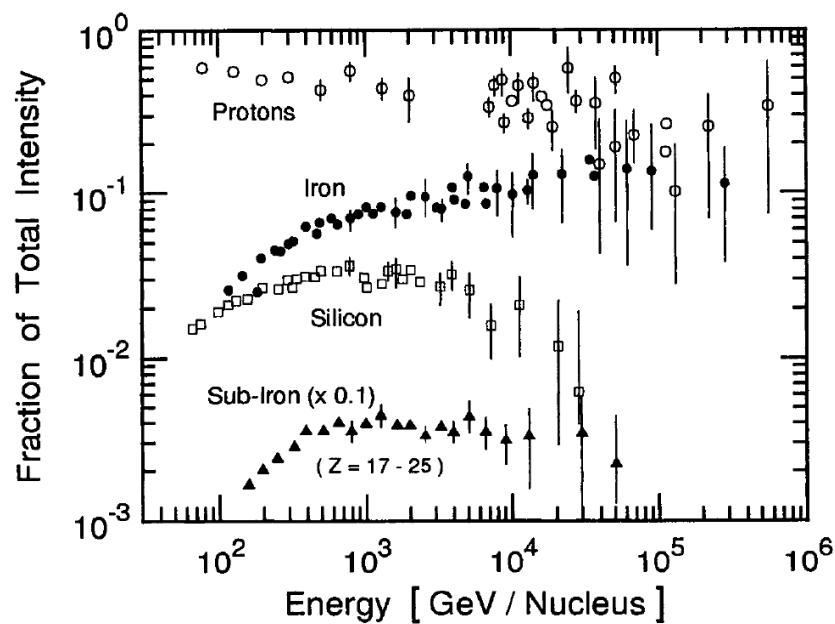


Figure 2.10. Fractions of some typical cosmic ray elements relative to the total differential intensity as a function of energy per nucleon (see [42] and references therein)

Fractions of typical primary cosmic ray elements relative to the total differential intensity are shown in Figure 2.10 as a function of energy per nucleus. Presence of the heavier elements in the primary radiation seems to have tendencies to increase with the increase in energy up to $\sim 10^{14}$ eV/n where the knee region of the all particle spectrum is approached.

Measurements of the high energy primary cosmic rays (beyond $\sim 10^{14}$ eV/n) could only be made using air shower techniques. However, since the results have large statistical uncertainties, it is difficult to conclude whether the fractions of the proton and iron components cross with each other or not. Moreover, at higher energies the mean mass of the primary radiation is investigated instead of the energy spectrum of an individual element. The mean logarithmic mass number is defined as

$$\langle \ln A \rangle = \sum_i a_i \ln A_i, \quad (2.4)$$

where a_i is the relative portion of the nucleus with the mass number A_i . The mean logarithmic mass numbers of the primary cosmic rays obtained from different experiments (ATIC-2, JACEE, KASCADE and HiRes) are illustrated in Figure 2.11 as a function of the energy. The solid and dashed lines in the figure correspond to the dip and ankle scenarios [43], respectively.

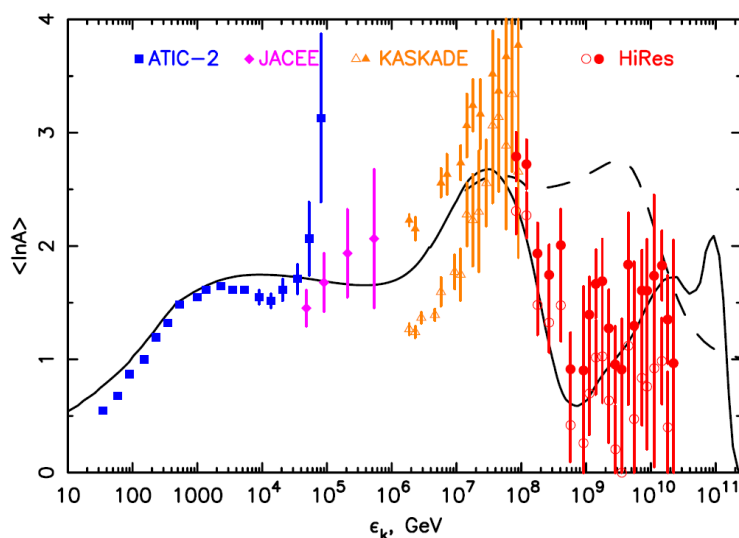


Figure 2.11. The mean logarithmic mass number of the primary cosmic rays as a function of the energy (see [44] and references therein)

Increase in the average primary mass number as a function of energy up to $\sim 10^{17}$ eV is seen from the figure. While $\langle \ln A \rangle \cong 2$ ($\langle A \rangle \cong 7.4$) before the knee ($\sim 10^{15}$ eV), it has a peak value of $\langle \ln A \rangle \cong 3.5$ ($\langle A \rangle \cong 33$) at the energy of $\sim 5 \times 10^{16}$ eV. For even higher energies, the primary composition seems to get lighter again and protons become dominant at the highest energies. This is also consistent with the theory that interactions of the nuclei having ultra-high energies with the cosmic microwave background radiation dissociate them.

Interactions of the primary cosmic rays with the interstellar medium produce both stable and unstable isotopes as the secondaries. Therefore, cosmic rays reaching the Earth's atmosphere contain not only primaries mentioned above, but also some unstable secondary elements like ^3He , ^{10}Be and ^{32}Si depending on the target material. The ratios of various elements and isotopes are important to determine the amount of matter the cosmic rays have traversed on their way from the source to the observer and to estimate the confinement time. For example, the age of the cosmic radiation, which means its average travel time, can be computed from the abundance of ^{10}Be (half-life of $\sim 1.5 \times 10^6$ year) in the radiation (see, for instance, [45]).

2.2.3. Their origin

The origin of the cosmic radiation is not yet fully known. However, it is known that the bulk of it comes from the sources present in the Milky Way galaxy. Although cosmic ray particles reach the Earth's atmosphere nearly isotropic, this does not mean that their sources are uniformly spread around the Earth. Since they are deflected and scattered by the magnetic fields present in the galaxy and by the Earth's magnetic field, they lose their original direction of motion. Some possible orbits of the charged cosmic rays under the influence of the Earth's magnetic field are illustrated in Figure 2.12. The complexity of the orbits depends heavily on the charge and the momentum of the particle.

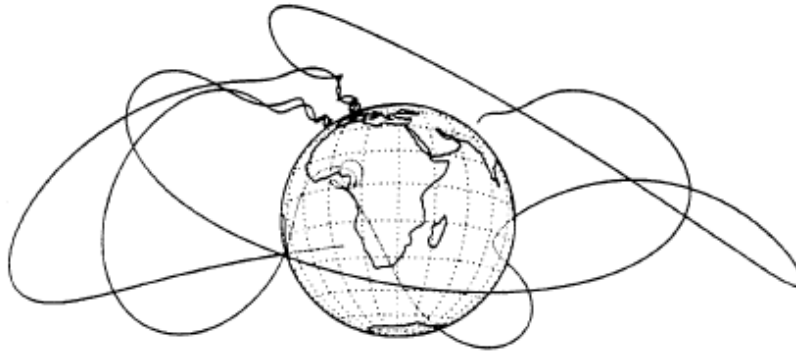


Figure 2.12. Some examples for the orbits of the charged cosmic rays affected by the Earth's magnetic field [46]

In spite of the uncertainties on the origins of the cosmic rays, they can be categorized according to their energies as the following:

- i. *Solar Cosmic Rays*
- ii. *Galactic Cosmic Rays*
- iii. *Extragalactic Cosmic Rays*

Solar cosmic rays concern the lowest energy part, extending up to ~ 10 GeV, of the cosmic ray spectrum. They have a composition similar to that of the Sun and they are ejected primarily in the solar flare events and coronal mass ejections. As the solar activity—flares increase, more particles are ejected, and the intensity of the solar cosmic rays increases. On the other hand, the solar wind and its associated magnetic field prevent the access of the low energy cosmic rays coming from outside to the inner solar system. Such a decrease in the galactic cosmic ray intensity, resulting from the solar activity, is known as the *Forbush decrease* [47], which is discussed in Section 2.4.1. As a result of the Forbush decrease, energy spectrum of the primary cosmic rays (Figure 2.4) is curved in the low energy region.

Galactic cosmic rays, which are the cosmic particles with energies extending up to $10^{17} - 10^{18}$ eV, come from outside the solar system, but within the Milky Way galaxy. They are accelerated to nearly the speed of light probably by the supernovae, which are the explosions of the stars of several times the mass of the Sun, occurred in the galaxy. When a star goes supernova, an expanding shell of the gas and dust, called the supernova remnant, is swept by the shock waves. Charged particles, mostly protons, are accelerated by the shockwaves to the high energies through a

process known as the *Fermi acceleration* [48]. According to the hypothesis, the energies of the atomic nuclei, crossing the supernova shock front, increase in the turbulent magnetic fields embedded in the shock. A particle may be deflected in such a way that it crosses the boundary of the shock many times, with an increase in energy at each passage, until it escapes as a cosmic ray. The direct evidence for that cosmic ray protons are accelerated in supernova remnants has recently been provided with the observations of synchrotron radiation by the Fermi Large Area Telescope [49]. The galactic magnetic field in the Milky Way galaxy is capable of confining the galactic cosmic rays. Therefore, it is possible that those cosmic rays have travelled many times across the galaxy before reaching the Earth's atmosphere.

Extragalactic cosmic rays constitute the highest energy part (greater than $\sim 10^{18}$ eV) of the cosmic ray spectrum. They are thought to be generated in some powerful objects like radiogalaxies and quasars in the universe. The idea that the very high energy cosmic rays must originate outside our galactic disk was previously suggested by G. Cocchini [50].

The *gyroradius* (or *Larmor radius*, R_L) of a relativistic particle with electric charge number Z and energy E in a magnetic field with a component B normal to the velocity vector is given by the expression

$$R_L = 1.08 \times 10^{-15} \frac{E}{ZB}. \quad (2.5)$$

If E and B in the equation have the units of eV and μGauss respectively, R_L is found to be in units of pc [51]. The equation is based on the equilibrium between the central and the Lorentz forces acting on a charged particle moving in a magnetic field. Using this equation, energy of a proton with a gyroradius of 300 pc (typical thickness of the Galactic disk) in the galactic magnetic field, whose strength is about 3 μGauss , is calculated to be about 10^{18} eV. Since the particles with energies higher than $\sim 10^{18}$ eV, which approximately correspond to the ankle of the all particle spectrum, could not be held within the galaxy by the magnetic field, they most probably are of the extragalactic origin [52].

2.3. Cosmic Rays in the Earth's Atmosphere

As a primary cosmic particle, moving towards the Earth, enters the atmosphere, it encounters an increasing density of gas molecules like nitrogen and oxygen. Although very few of them, if any, reach the ground unaffected, almost all of the primaries interact with the nuclei present in the air at the altitudes between 20 km and 30 km. If the energy of the incident particle is high enough (above a few GeV), its collisions with the nuclei result in either kicking out some nucleons or producing new particles mainly mesons like pions (π^- , π^+ and π^0) and kaons (K^- , K^+ and K^0). These secondary particles move in the same direction with the corresponding primaries and, if they have enough energy, continue to interact with the air molecules. The lower energy secondaries lose their energy by ionization during their travel in the atmosphere. As a result, the number of cosmic particles in the atmosphere reaches a maximum at an altitude of ~ 20 km, which is known as the *Pfotzer maximum* [53], and declines as approaching the Earth's surface. Such a cascade of the secondary cosmic rays initiated by the interaction between a high energy cosmic particle and air molecules is called the extensive air-shower. Development of an air shower in the Earth's atmosphere is shown in Figure 2.13 as a schematic drawing.

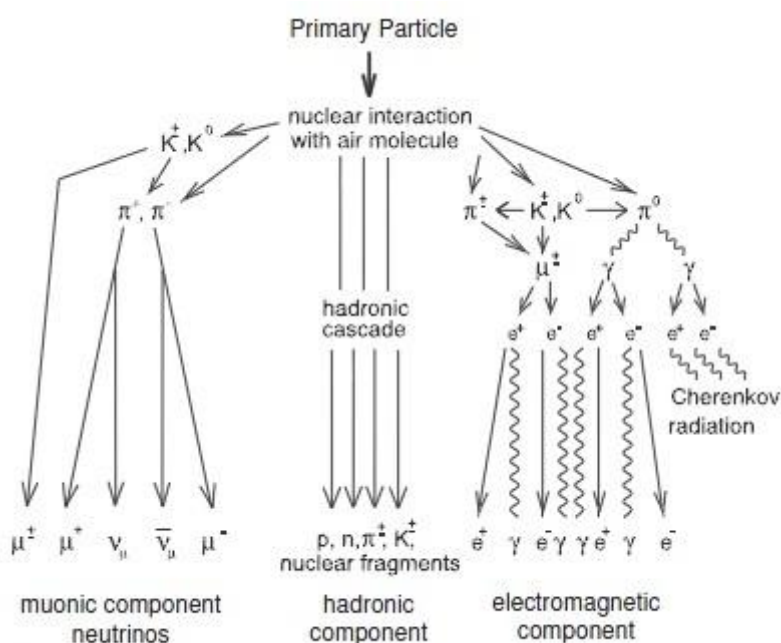


Figure 2.13. Development of an air shower in the Earth's atmosphere [54]

The extensive air shower can be divided into three components as the hadronic, the muonic, and the electromagnetic. Nucleons and other high energy hadrons, mainly pions and kaons, are members of the *hadronic component*. Electrons, positrons and photons constitute the electromagnetic component of the air shower. Since the members of the *electromagnetic component* are easily absorbed, they are also called as the *soft component*. The decay product of the mesons, muons and the neutrinos are known as the *muonic component* of the air shower. Since the muons weakly interact with the matter they propagate in, they can get through the entire atmosphere and higher energy ones are able to reach deep underground. For this reason, they are also called as the *hard component* of the cosmic rays.

Because of their very short lifetime (8.4×10^{-17} sec), neutral pions (π^0) decay almost instantly into two gamma photons (γ) which can produce electron-positron (e^-e^+) pairs. High energy electrons and positrons may emit Cherenkov and Bremsstrahlung radiations. In addition, charged pions, with a mean life of 2.6×10^{-8} sec, decay either into muon (μ^-) and muon anti-neutrino ($\bar{\nu}_\mu$) or into anti-muon (μ^+) and muon neutrinos (ν_μ) depending on their charges. μ^- (μ^+) is a lepton with mean lifetime of 2.2×10^{-6} sec, which is ~ 100 times greater than that of charged pions, and decays into an electron (a positron), a muon neutrino (a muon anti-neutrino) and an electron anti-neutrino (an electron neutrino). The most important decay modes, together with the corresponding decay probabilities, of main unstable secondary cosmic rays are given in Table 2.2.

Table 2.2. Decay modes of some unstable particles and their probabilities [55]

Decay Modes	Probability (%)
$\pi^\pm \longrightarrow \mu^\pm + \nu_\mu (\bar{\nu}_\mu)$	~ 100
$\pi^0 \longrightarrow \gamma + \gamma$	~ 98.8
$K^\pm \longrightarrow \mu^\pm + \nu_\mu (\bar{\nu}_\mu)$	~ 63.5
$K_L \longrightarrow \pi^\pm + e^\pm + \nu_e (\bar{\nu}_e)$	~ 38.7
$\mu^\pm \longrightarrow e^\pm + \bar{\nu}_\mu (\nu_\mu) + \nu_e (\bar{\nu}_e)$	~ 100

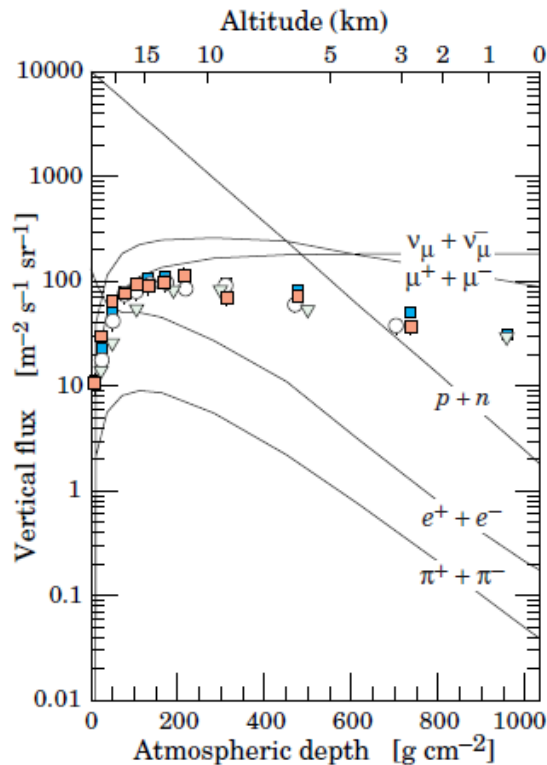


Figure 2.14. Vertical fluxes of cosmic rays in the atmosphere with energies above 1 GeV as a function of altitude. Markers show the measured negative muon fluxes (see [55] and references therein)

Calculated vertical fluxes of some cosmic ray particles in the atmosphere with energies above 1 GeV as a function of altitude (or atmospheric depth) are illustrated in Figure 2.14. Also in the figure are shown the negative muon flux measurements made by different groups. As it can be realized from the figure, each component of the secondaries has different altitude dependency since each has different decay and interaction properties. Below the altitude of ~ 20 km (the Pfozter maximum), fluxes of the secondaries other than neutrinos are reduced with different slopes as they approach the Earth's surface. This is because the interactions with the atmospheric nuclei, whose density increase with the decrease in the altitude, cause the cosmic particles to lose energy. The curve indicating the decrease in the muon flux is flatter than that of the other secondaries. This can be attributed to the fact that muons interact with the air molecules weakly and have relatively longer lifetime. On the other hand, the flux of the neutrino, which is a lepton with no charge and almost no mass, continuously increases. This is because the neutrinos could penetrate vast thicknesses of material without interaction and decays of the muons and some mesons contribute to their flux.

2.4. Effects of the Magnetic Fields on Cosmic Rays

Since the cosmic rays are mostly charged particles, they are deflected by the magnetic fields. As stated before, the galactic cosmic rays are confined in the galaxy thanks to the galactic magnetic field. Similarly, magnetic fields of the Sun and the Earth also affect the charged cosmic rays during their propagation in the interplanetary space and the atmosphere. For instance, measurements performed in a spacecraft travelling towards the boundary of the solar system show that intensity of the galactic cosmic rays increases with distance from the Sun [56]. This shows that interplanetary magnetic field embedded in the solar wind prevents the low energy cosmic rays to penetrate into the solar system. In addition, cosmic ray intensities in the polar and equatorial regions of the Earth differ from each other, which result from the magnetic field of the Earth. In the following two subsections, the effects of the magnetic fields originated from the Sun and the Earth will be discussed.

2.4.1. Heliospheric magnetic fields

The *heliosphere* is a large, roughly elliptical region of the space surrounding the Sun. In this region, the solar wind, the solar magnetic field and the matter ejections from the Sun dominate in controlling the behavior of the plasma inside the solar system. The heliosphere extends well beyond the orbit of the Pluto.

The solar magnetic field has a complex structure. Unlike the Earth, which has only one north and one south pole, there are many north and south polarities on the Sun scattered all over the surface. Magnetic field lines around the Sun extend between the opposite polarities. Since the solar wind is a kind of plasma and electrically conductive, magnetic field lines of the Sun is carried out through the solar system by the solar winds. Close to the Sun, the magnetic field dominates the plasma flow and it undergoes an important super-radial (or non-radial) expansion. Rotation of the Sun causes the field lines, remote from the surface, to have a shape like a rotating spiral, known as the *Parker spiral* [57], centered at the center of the Sun (see Figure 2.15).

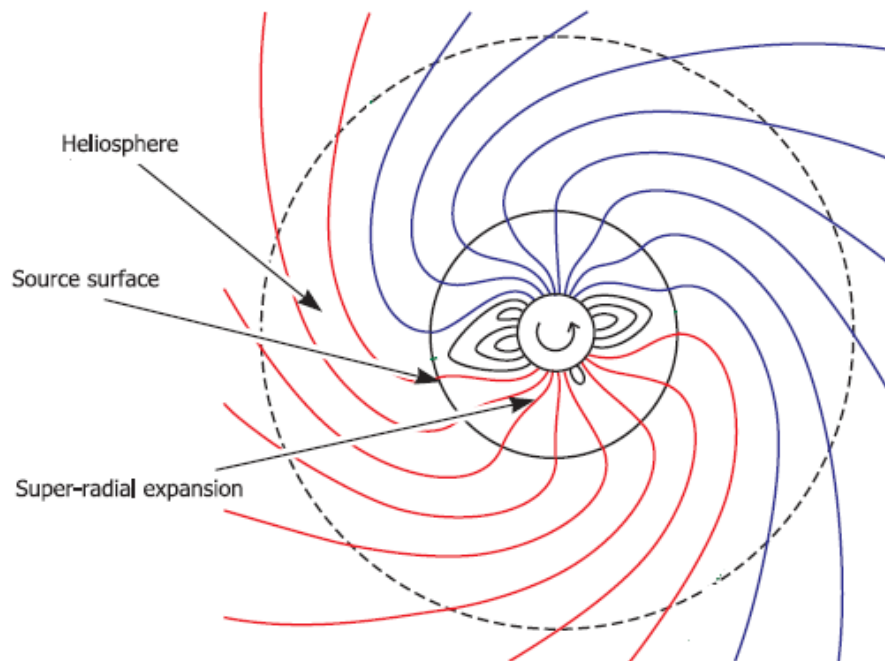


Figure 2.15. A sketch of the solar magnetic field in the ecliptic plane [58]

In the figure, the red and blue colored lines represent the opposite magnetic field polarities. At the source surface, shown in the figure with a circle having a radius of a few solar radii, the field lines become purely radial. In the heliosphere, rotation of the magnetic field lines within the solar wind creates a spiral geometry.

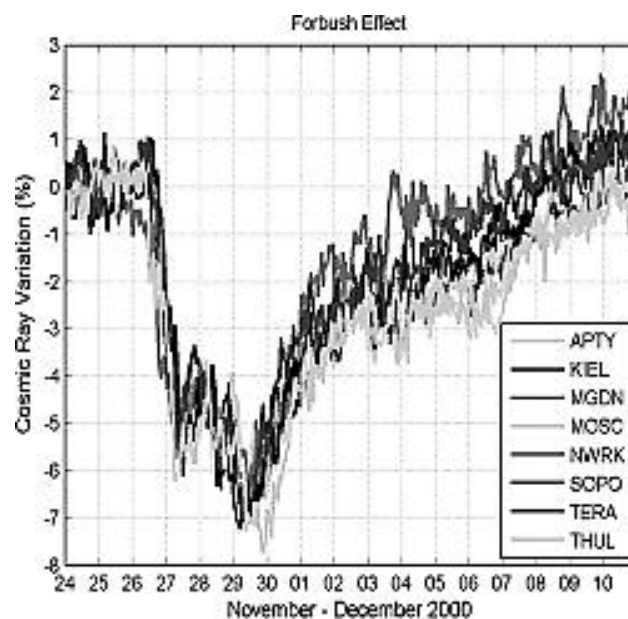


Figure 2.16. Cosmic ray variations as a function of time indicating the Forbush Effect (see [59] and references therein)

In addition to its complexity, magnetic field of the Sun changes in time. During the solar flares or coronal mass ejections, the ejected plasma reaches higher velocity yielding higher magnitude of the field in the heliosphere. Since the increased magnetic field prevents the access of more low energy galactic cosmic rays into the inner solar system, a decrease in the galactic cosmic ray intensity, known as the Forbush decrease [47], occurs. The decrease becomes rather suddenly, within a few hours, but reaches the previous normal level in days as shown in Figure 2.16.

Apart from the randomly occurring activities of the Sun, there are also some periodic occurrences that affect the cosmic rays. Intensity variations due to the both periodic and aperiodic solar activities are known as the *solar modulation effects* [60]. Two important examples of the periodic changes that the Sun undergoes are the 11-year solar cycle, and the closely related 22-year cycle.

Every 11 years, the Sun has a period of least, smaller sunspots and flares. This period is called the *solar minimum*. On the contrary, the Sun has more, larger sunspots and flares during the period known as the *solar maximum*. This periodic change in the Sun's activity was recognized firstly by M. Schwabe in 1843 [61], and is named as the *Schwabe cycle*. Solar cycles are numbered beginning with cycle 1, which started with a solar minimum in 1755 and ended in 1766 (with a solar maximum in 1761) [62]. A solar minimum was observed in 2008, which is the end of cycle 23 and the beginning of cycle 24 [63]. By measuring the cosmic ray flux over the years, it was realized that the average flux changes with a period of 11 years in such a way that it is anti-correlated with the level of solar activity. Namely, the cosmic ray intensity at Earth is low when the solar activity is high and there are lots of sunspots (solar maximum). Similarly, the cosmic ray intensity increases during the quiet Sun with fewer sunspots (solar minimum).

In addition, the magnetic polarity of the sunspot pairs reverses and then returns to its original state with a period of about 22 years. This cycle is named as the *Hale cycle* after G. Hale who discovered it [64]. As a result of such polarity reversal, cosmic ray fluxes and the shape of the spectra at Earth seem to be different in odd and even numbered Schwabe cycles [65].

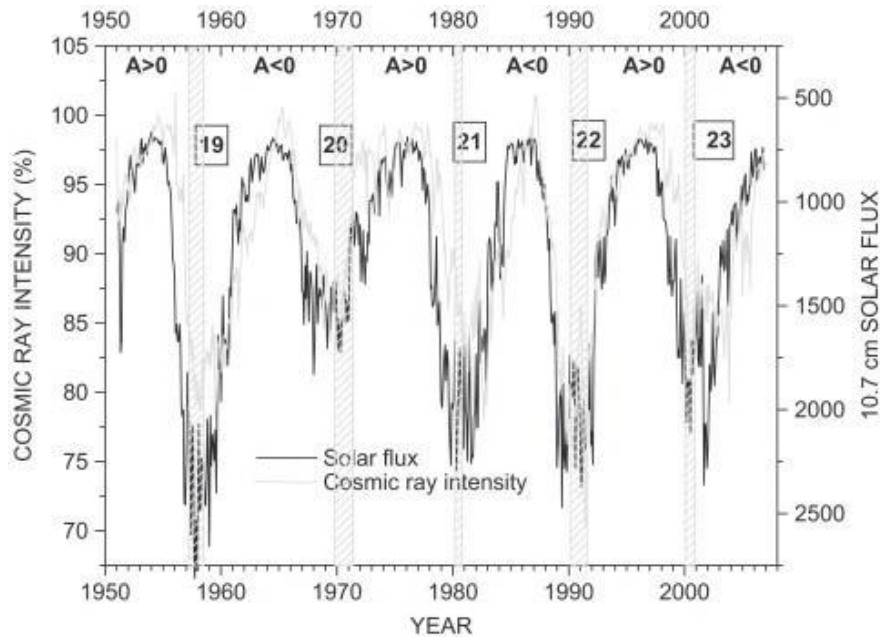


Figure 2.17. Cosmic ray intensity and 10.7 cm solar flux variation in years 1951–2006 [66]

The main features of the solar modulation of cosmic ray intensity related to the 11-year and 22-year solar cycles for the period 1951–2006 are shown in Figure 2.17. The period when the magnetic field is directed outwards in the northern hemisphere of the Sun is known as the positive polarity ($A > 0$), and the opposite situation known as negative polarity ($A < 0$). It can be concluded from the figure that the recoveries of cosmic ray intensity are rather rapid during the even cycles, whereas they are slow and take longer periods during the odd cycles.

Solar modulation affects the low energy part of the cosmic ray spectrum, especially below ~ 10 GeV. Spectra of the galactic cosmic protons and the helium nuclei obtained by the PAMELA detector between the years 2006 and 2009 are shown in Figure 2.18. It is clearly visible in the figure that fluxes of both primary protons and helium nuclei, with energies below ~ 10 GeV/n, increase for the years from 2006 to 2009 since the solar activities decrease in that period and reach a minimum in 2009. Also in the figure is seen that the primary spectra above ~ 10 GeV/n do not change in time, confirming the expectation that the solar activities do not affect the high energy cosmic rays.

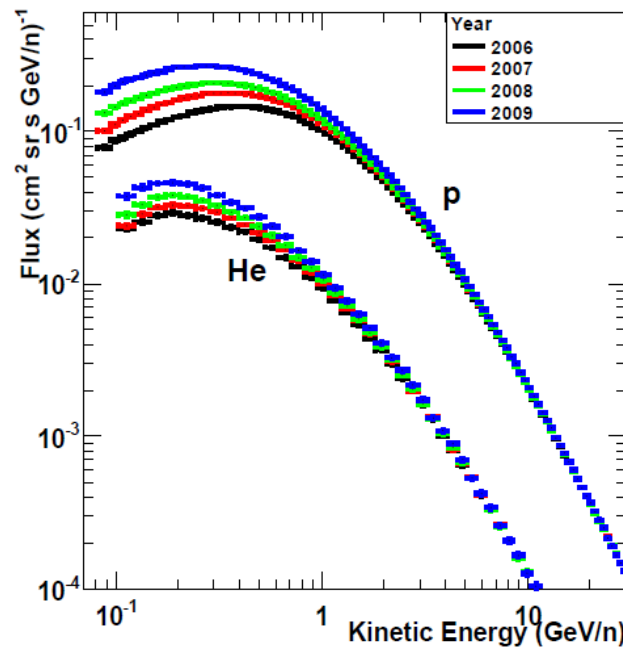


Figure 2.18. Galactic cosmic proton spectra obtained from the PAMELA experiment performed between the years 2006 and 2009 [67]

2.4.2. Geomagnetic fields

The magnetic field of the Earth, which is also known as the *geomagnetic field*, is generated by the electric currents produced by the rotation of the liquid metallic outer core. The magnetic field around the Earth is similar to that of a huge bar magnet located at its center, inclined with respect to its axis of rotation (see Figure 2.19 a). However, the geomagnetic field lines far away from the surface are affected by the solar wind in such a way that the magnetic field lines on the sunward side of the Earth is compressed towards the Earth, and the ones on the opposite side are extended like a long tail towards the night side. In this way, the geomagnetic field lines form a cavity, around which the solar wind flows (see Figure 2.19 b). This cavity, in which the Earth's magnetic field dominates, is called the *magnetosphere*. Although the edge of the magnetosphere on the sunward side is at a distance of ~ 10 Earth radii from the Earth's center, its tail extends more than 100 Earth radii on the night side.

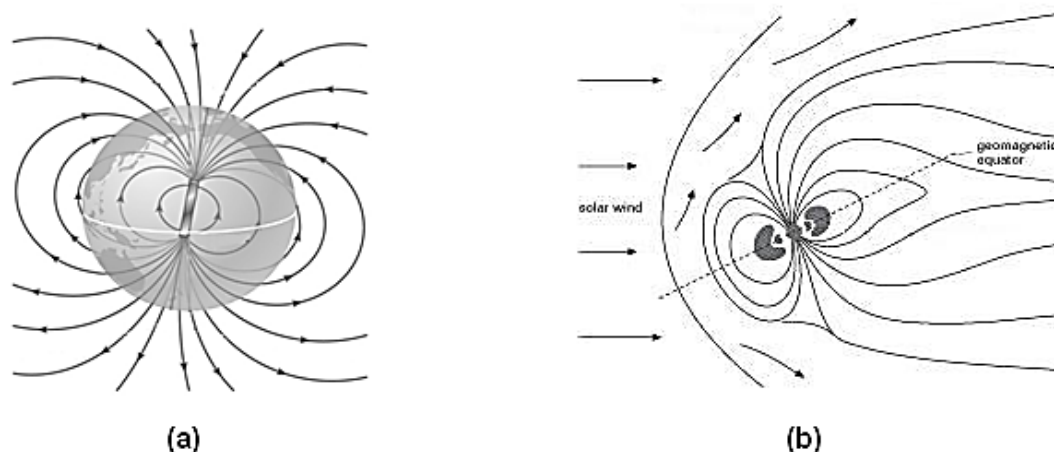


Figure 2.19. a) Magnetic field lines of the Earth near the surface b) Earth's magnetosphere shaped by the solar winds

The magnitude of the geomagnetic field has a maximum value of ~ 0.6 G ($60 \mu\text{Tesla}$) near the geomagnetic poles and a minimum value of ~ 0.3 G ($30 \mu\text{Tesla}$) near the equator at the Earth's surface [68]. The magnetic field lines are almost perpendicular (parallel) to the Earth's surface near the poles (equator). In addition to the dependency of the geomagnetic field near the Earth's surface on the location (latitude and longitude), the field slightly varies over the time, which is attributed to the changes in the activity with time in some intense regions of the core.

Cosmic ray particles approaching the Earth from the outer space are affected by the geomagnetic field and their trajectories are bent. Disregarding the existence of the atmosphere, arrival of a particle at the Earth's surface depends on the local geomagnetic field (magnitude and direction), energy, charge, and direction of propagation of the particle. In order to describe the geomagnetic shielding simply, the term *cut-off rigidity* is used. The cut-off rigidity (R_C) is defined as the lowest rigidity (momentum per unit charge) that a charged cosmic particle can still penetrate the geomagnetic field to reach a given location on the Earth's surface and given by

$$R_C = \frac{pc}{eZ}. \quad (2.6)$$

In the equation, p is the momentum of a relativistic particle in the unit of GeV/c and eZ is the electric charge of the particle. Hence, the corresponding unit of rigidity

becomes GV, which is independent of particle species or nuclear composition. Namely, it can be said that charged particles, regardless of type, with the same rigidity follow identical paths in a given magnetic field. Cut-off rigidity depends also on the zenith and azimuth angles of the particle's direction of propagation. However, cut-off rigidities are usually determined for the vertical incidence to the Earth's surface, which yields the minimum magnetic rigidity. Calculations show that the vertical cut-off rigidity near the geomagnetic equatorial region is around 16 GV, while it is less than 1 GV near the magnetic poles [69]. Since the geomagnetic cut-off rigidity forms a lower limit for the primary cosmic ray spectrum, the measurements performed in the polar region of the Earth yield the entire spectrum.

Cosmic ray proton fluxes measured in different cut-off regions obtained in a satellite borne experiment, PAMELA [70], are shown in Figure 2.20. For each spectrum, the part above the cut-off energy represents the primary component, whereas the part below the cut-off is for the secondary (re-entrant albedo) component of the cosmic ray protons. There is no secondary component observed near the poles, where the geomagnetic field is nearly perpendicular to the surface and the cut-off is very low. As moving toward the equatorial region, the geomagnetic cut-off increases and the two components become visible in the spectrum.

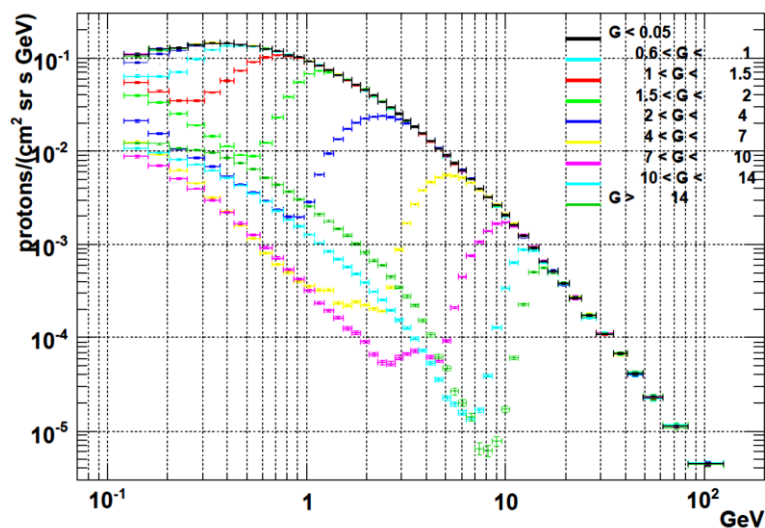


Figure 2.20. The differential energy spectra of protons at different values of the geomagnetic cut-off (G) obtained in the PAMELA experiment [70]

Another effect of the geomagnetic field on the cosmic ray is known as the East–West effect or the *East–West asymmetry*, which has been known since 1930s [14–17]. Although, the primary cosmic rays reach the vicinity of the Earth isotropically, the geomagnetic field bends the trajectories of the low energy ones in such a way that different number of particles arrive the Earth from the eastern and western directions because of the positive charge excess of the primaries. In particular, the low energy cosmic rays coming from the eastern direction are suppressed compared to those from the west. Although the East–West effect is the strongest at the top of the atmosphere, it becomes less pronounced at sea level as a result of the interaction with the atmospheric nuclei.

2.5. Effects of the Cosmic Rays

Cosmic rays generate a continuous radiation dose where they propagate in. They can interact with the atoms of the surrounding media like atmospheric gasses, living cells and electronic equipment. Their interaction with the media may cause changes in nuclear structure or may ionize some of the atoms leading to the dissociation of the molecules within the matter or organism. The effects of the cosmic rays on human health, atmospheric chemistry and electronic devices are discussed in three categories in the following subsections.

2.5.1. Effects on the human health

According to the reports of the United Nations Scientific Committee on the Effects of Atomic Radiation (UNSCEAR), the annual effective dose at the Earth’s surface from all the natural sources is 2.4 mSv (miliSievert) [71]. Note that, the *Sievert* is the SI unit of measuring the effective radiation dose and it is equivalent to Joule/kg. Cosmic rays contribute to a small fraction of the total annual dose with 0.39 mSv/yr., as shown in Table 2.3. Apart from the variation with the geomagnetic latitude and the solar activity, the dose rate of the cosmic radiation changes with the altitude in such a way that people living at higher altitudes are exposed to a greater dose compared to the ones living at lower altitudes.

Table 2.3. Average annual radiation exposure from the natural sources [71]

Source	Average dose (mSv)	Typical range (mSv)
Air (Radon etc.)	1.26	0.2 – 10.0
Terrestrial Radiation	0.48	0.3 – 1.0
Cosmic Radiation	0.39	0.3 – 1.0
Internal Radiation	0.29	0.2 – 1.0
Total	2.4	1.0 – 13.0

The Earth's atmosphere has a very important role in protecting from the cosmic radiation, since cosmic rays lose energy by interacting with the atmospheric nuclei. At ground level, the atmosphere provides as much shielding as a ~90 cm of lead against the cosmic radiation. However, modern passenger planes, flying at high altitudes (10 – 15 km), have less atmospheric shielding and they are exposed to higher cosmic radiation. More precisely, the dose rate of the cosmic radiation, which is nearly 0.2 $\mu\text{Sv/h}$ at the ground level, reaches the value of ~10 $\mu\text{Sv/h}$ at an altitude of 10 km [72]. However, air passengers do not receive significantly high radiation dose because of the shortness of the journey time in spite of the higher dose rate. Nevertheless, the people (especially the airline crew) being at flight altitude for 400 hours per year would be exposed to approximately 4 mSv cosmic radiation annually.

Cosmic radiation exposure increases strongly above the atmosphere. For example, the International Space Station, maintained at altitudes between 340 km and 400 km, is exposed to effective dose rates ranging from 0.4 to ~1 mSv/day during a solar cycle [73]. Since the magnetosphere is another protective layer against the cosmic rays, the radiation exposure is greater outside the magnetosphere. Therefore, radiation protection of the astronauts becomes crucial when it comes to planning a mission to the other planets. For example, a mission to the Mars (half a year to go, 1.5 year to stay there and another half a year to come back to the Earth) would expose astronauts to a cumulative radiation dose of ~1 Sv. Similarly, for the Pluto the total radiation exposure is calculated to be 70 Sv, which is able to kill a living cell [74].

Another example, if not final, on the subject is that astronauts have higher risk of developing cataracts than the people who have not been in space [75]. In order to avoid the health problems originated from the cosmic radiation, NASA imposes short-term and career dose limits for the astronauts. While the short-term limits are determined to prevent the occurrence of any clinically significant health risk, the career limits are used to restrict the increased risk of cancer to an acceptable level [73].

2.5.2. Effects on the atmosphere

Interactions of the cosmic rays with the atmospheric molecules, mainly nitrogen and oxygen, cause a number of chemical reactions many of which start with ionizations. As a result of such reactions, a number of radioisotopes are continuously produced in the Earth's atmosphere. For example, when secondary cosmic neutrons, which are produced in the upper atmosphere, collide with the nitrogen (${}^{14}_7N$) atoms, the atoms turn into radioactive carbon-14 (${}^{14}_6C$) via the reaction



and the carbon-14 atoms with a half-life of 5730 years [76] undergo beta decay



It is known that the cosmic rays have kept the level of carbon-14 in the atmosphere roughly constant for thousands of years until the beginning of open air nuclear tests in 1950s. The carbon-14 atoms may form carbon dioxide, which is used in photosynthesis. Animals and people eat plants and take in carbon-14 as well. As a result, the ratio of carbon-14 to carbon-12 in the air and in all living things at any given time is nearly constant. As soon as a living organism dies, it stops taking in new carbon, and the ratio of carbon-14 to carbon-12 starts to change with time. Therefore, it is possible to determine the age of a formerly living thing (animal, plant etc.) by looking at such ratio, which is known as the *carbon-14 dating method*.

In addition, *aurora*, which is the colored light display in the sky especially near the Earth's magnetic poles, is a visible effect of the cosmic rays. Particles coming from the solar flares and the corona of the Sun are deflected by the magnetosphere, and some of them with relatively lower energies are also able to penetrate the atmosphere in the polar region of the Earth. Low energy solar particles, mostly electrons, flow along the geomagnetic lines, which are nearly vertical in the Earth's magnetic poles, and collide with the atmospheric gases at the altitudes of 70 – 200 km. These collisions result in the excitation of the oxygen and nitrogen atoms in the air. During the transition to the ground state of excited atoms, the energy is released as light. Variation in the color of this light is attributed to the type of atom that is excited. Namely, green light is produced by the oxygen atoms at the lower altitudes and red light is most probably from the high-altitude oxygen or nitrogen atoms. Moreover, nitrogen may also produce blue or purple colored aurora.

The role of the cosmic rays in the cloud formation and its impact on the climate is a topic of debate. H. Svensmark, a Danish scientist, claimed that the cosmic rays contribute to cloud formation and global warming [77]. According to Svensmark's hypothesis, increase in the cosmic ray intensity, which causes an increase in the rate of ionization in the atmosphere, results in an increased cloud formation rate. With the increase in the cloud cover, less amount of radiation would be able to reach the Earth's surface, and a global cooling occurs. However, some later works (see, for instance, [78]) assert that such contribution is negligible.

Some scientists established mechanisms which exhibit the role of cosmic rays in generating thunderstorms and lightning. According to the idea [79], the electric fields present in thunderclouds are not strong enough to initiate electric breakdown. On the other hand, the secondary cosmic rays are energetic and able to knock down more electrons, which form a cascade. After the critical energy is reached, the electrons result in a sudden discharge, releasing the energy in the form of lightning. Although this mechanism is widely agreed upon, the effects of the cosmic rays on thunderclouds and on the climate are still requiring much more worldwide research activities.

2.5.3. Effects on the electronic devices

Cosmic rays can ionize atoms and displace them within their crystalline lattice inside the materials they propagate in. This may alter the content of memory cells [80] or cause the malfunctioning of logic devices or even destroy the component. At normal cruising altitudes, the intensities and the energies of the cosmic rays are sufficiently high to affect the microelectronic devices of the plane [81]. They can deposit enough charge in a small volume of semiconductor to change the state of a memory cell or cause some hardware failure.

Because of their large areas, being outside the atmosphere and having long exposure time, solar panels on a spacecraft are especially affected by the cosmic rays. Mechanical and electrical insulating properties of the materials used in a spacecraft can also be damaged by the cosmic rays leading the decrease of the equipment's lifetime. The disturbances and failures in the Anik (1994) and Telstar satellites were both attributed to the cosmic ray effects [82]. As the technology evolves, cosmic radiation induced errors are being tried to be minimized by deploying future generations of electronics. However, usage of the devices with very small dimensions and made of new materials cause some different problems [83].

2.5.4. Usage of cosmic rays

Cosmic ray muons, the most numerous charged secondaries at the ground level, are used to generate three dimensional images of some big material's interior. This technique is known as the *muon radiography*. The process is very similar to the X-ray imaging, except muons are produced naturally and do not damage the materials they contact. Since muons are very penetrating and they can reach deep underground, muon tomography can be used to visualize inside the huge materials like a mountain, which cannot be visualized using the X-rays. The number of muons passing through a material depends on the density. Therefore, the object to be investigated is sandwiched between a pair of muon detectors and, measurement of the degree of the scattered muons by the interaction could yield the detailed image.

The muon radiography technique was first used in the 1955 to determine the depth of the rock layer above an underground tunnel [84]. The depth was calculated using the muon fluxes measured both inside and outside the tunnel. Then, this technique was used in the search for hidden chambers in the ancient pyramids of Giza, Egypt [85]. In subsequent years, the idea of using cosmic rays to make measurements on large objects was utilized in different researches. By placing the muon detectors around a volcano, the amount of molten rock within the craters could have been determined [86, 87].

In addition, this technique also works in detecting "high Z" materials like uranium in a container or nuclear reactor. Such materials within a container show up more clearly than the surrounding materials since the muon scattering angle increases with atomic number. For example, muon radiography was used for diagnosing the damaged cores of the Fukushima reactors, which were heavily damaged in March 2011 by a tsunami occurred after a great earthquake [88]. Muon radiography is also utilized to detect nuclear materials, even if it is heavily shielded, in a container by arranging detectors above and below of it [89]. As far as the health risks from the radiation are concerned, muon radiography has advantage with respect to the conventional radiography, even though the latter yields better image quality.

CHAPTER 3. MUONS

Cosmic ray muons are the most numerous charged particles at sea level. Since they are electrically charged, they can be easily detected using different kinds of particle detectors. Muons interact weakly with the media they propagate in, and they can even penetrate large thickness of water or rock. Therefore, muons are also called the *penetrating component* of the cosmic rays [1]. Measurement of the absolute muon flux and determination of the muon charge ratio, in addition to the angular dependence of muon intensity, at ground level are essential to get information on the propagation of the cosmic rays in the atmosphere. In addition, muon measurements provide an important tool to test the atmospheric neutrino flux calculations [90]. Moreover, underground and underwater muon experiments also yield significant information on several issues. For example, deep underground muon data are used for the estimations of the background radiation in the underground areas housing the neutrino experiments. Furthermore, high energy region (above $\sim 10^{14}$ eV) of the primary cosmic rays can be derived using deep underground muon data.

3.1. Discovery of the Muon

In 1935, H. Yukawa formulated a theory that describes the nature of the strong interactions between two nucleons [91]. According to the theory, the nuclear interactions occur due to the exchange of a particle in a similar way to the photon-exchange in electromagnetic interaction. The range of the electromagnetic force is infinite since photons are massless. In Yukawa's theory, the exchange particles could not be massless because of the short range (limited by the size of the nucleus) of the nuclear force. Yukawa calculated the mass of the exchange particle as $\sim 100 \text{ MeV}/c^2$, which is equivalent to approximately 200 electron masses, using the uncertainty principle.

The prediction of Yukawa was not largely known until a new particle with a mass nearly equal to that of Yukawa's particle was discovered by S.H. Neddermeyer and C. D. Anderson [92] in 1936 and also by J. C. Street and E. C. Stevenson [93] in 1937. During the observation of the tracks of the cosmic rays in a cloud chamber, they noticed particles that curved differently from electron and proton, indicating the existence of a particle with a mass intermediate between that of the electron and proton. The mass of this new particle was determined by Street and Stevenson to be ~ 130 times the rest mass of the electron. A much better determination (240 electron masses) was made by Neddermeyer and Anderson one year later [94]. The average of the masses determined from the experiments performed later was around $100 \text{ MeV}/c^2$. In addition, it was reported that these new particles with intermediate mass were unstable [95] with a mean life in the order of microseconds [96, 97]. A number of other observations showed the existence of such particles with both positive and negative charges.

At first, the name *mesotron* (middle particle) was suggested for the new particle taking into account that its mass was greater than that of the electron and smaller than that of the proton [98]. Then, H. J. Bhabha proposed the name *meson* [99]. Similarly, the electron was called a *lepton* (light weight), and the proton and neutron were called as *baryons* (heavy weight).

Because of its mass, Anderson's particle was initially thought to be the particle predicted by Yukawa. However, further and more detailed studies of the cosmic ray particles showed that Anderson's particle differs from the Yukawa's particle. A group of Italian physicists (M. Conversi, E. Pancini and O. Piccioni) performed an experiment to obtain information on whether the Anderson's particle could be the mediator of the strong interaction. It was expected that positive mesons would survive for their normal lifetime, while negative ones would be attracted to nuclei where they would be quickly absorbed. However, they found that the negative mesons almost always decay instead of being captured by the positively charged nucleus when they used light absorbers, such as carbon. Namely, the lifetime for decay was equal to the lifetime of the nuclear absorption of the meson in the absorbers with $Z \approx 10$. This observation indicates that the Anderson's particle does

not interact very strongly with the atomic nuclei, and they could not be the transmitter of strong force [100].

Soon after the observation of the Italian group, E. Fermi, E. Teller and V. Weisskopf made a theoretical analysis, in which they used the symbol μ standing for mesotron (meson) for the first time. Fermi's group found that there is a discrepancy about a factor of 10^{12} between the theoretical and experimental results for the mean life of the meson in carbon [101]. To make the issue clear, R. E. Marshak and H. A. Bethe suggested that there are two kinds of mesons with different masses in the nature. According to the hypothesis, the heavier meson, which corresponds to the Yukawa particle, was produced in the upper atmosphere. The light meson, which interacts with the matter weakly, was regarded as the decay product of the heavier one [102].

The puzzle was solved with the observation of two different middle weight particles in cosmic rays at mountaintop altitudes, where it is possible to observe some of the particles directly produced in cosmic ray collisions, by C. M. G. Lattes, G. P. S. Occhialini and C. F. Powell in 1947 [103]. For the observation, they used detectors called the *nuclear emulsions*, which are the sheets of light-sensitive material similar to a photographic film. They discovered that in some cases a particle that appeared to be a meson would stop and then emit another particle of somewhat lower mass, where the second one shows similar properties with the familiar meson. They called the first particle a *pi-meson* (or *pion* in short) because it was the primary particle in the two-step process. The tracks of the particles are shown in Figure 3.1. The symbol π was used to represent the new particle, while μ was for the familiar meson.

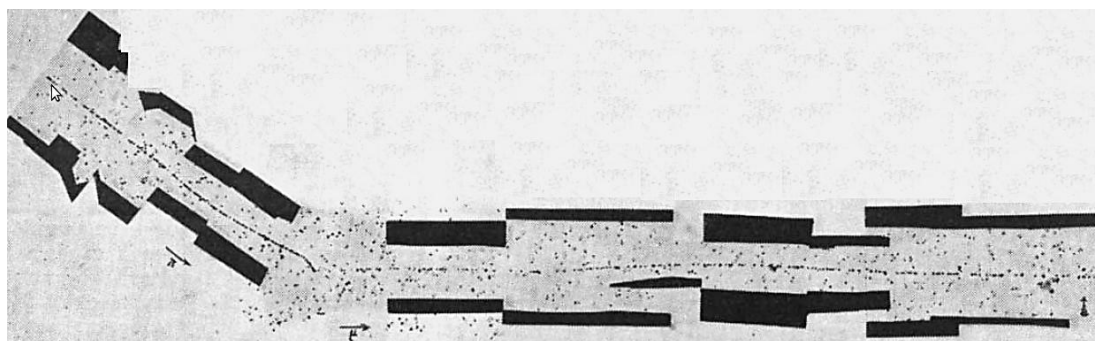


Figure 3.1. The decay of π -meson observed in a photographic emulsion [103]

It was concluded from the tracks that the charged π -meson decays directly to a μ -meson and at least one additional neutral particle required for energy and momentum conservation. A few months later, C. F. Powell and his collaborators published a new photographic emulsion picture, in which the decay of the muon is also visible (Figure 3.2). In the picture is seen the sequential decay of $\pi \rightarrow \mu \rightarrow e$. Thanks to the determination of the existence of two different middle weight particles, it was understood that π is the true Yukawa's meson, which mediates the nuclear force. After the observation of the π -meson, Yukawa was awarded by the Nobel prize in physics in 1949 [105].

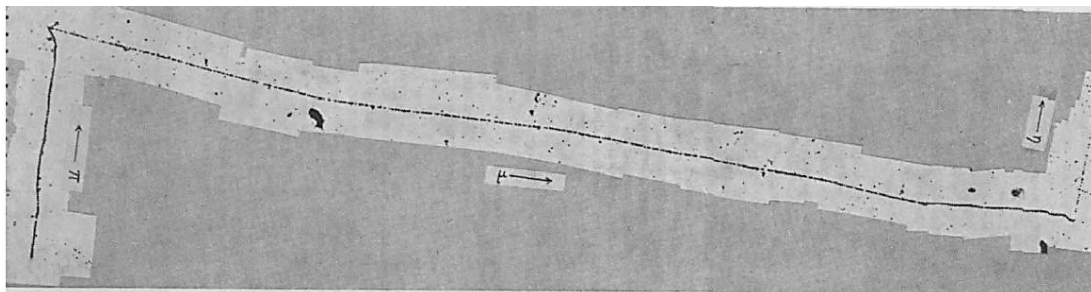


Figure 3.2. The decay chain of $\pi \rightarrow \mu \rightarrow \eta$ in photographic emulsion where η represents the electron [104]

In the following years, more types of mesons were discovered, and researches provided a better understanding of the properties of the particles with the invention of particle accelerators. It was found that μ -meson has very different properties in comparison with not only π -meson but also the other types of mesons discovered later. For instance, μ -meson does not have a strong interaction with the nuclei, even though all of the other mesons do. In addition, decay products of the μ -meson include both neutrino and anti-neutrino while only one of them can be observed in the decay of the other mesons. Furthermore, μ -meson was assumed to be obeying the Fermi-Dirac statistic because of its half-integer spin, which also makes it different from the other mesons with integer spin. Moreover, the mesons were defined to be the composite particles made up a *quark* and anti-*quark* pairs in the quark model. However μ -meson is a fundamental particle with no quark structure similar to the electron. Briefly, μ -meson behaves like a heavier version of the electron. Therefore, the μ -meson was understood not to be a kind of meson, but to be a member of the lepton family, and finally it was renamed as the *muon*.

3.2. General Properties of the Muon

Muon (μ^-) is an elementary particle, which is a member of the lepton family, with similar properties to the electron except for the mass and mean lifetime. Namely, it is a fermion with spin 1/2 and has a negative elementary electric charge just like an electron. The mass of the muon is $105.7 \text{ MeV}/c^2$, which is approximately 207 times that of the electron [55]. The muon has an antiparticle having the same properties with itself except that the antiparticle has opposite charge (positive). Therefore, the antiparticle, known as the *anti-muon* (μ^+), is also called the *positive muon*.

The muon (and also the anti-muon) is an unstable particle with a mean life of $2.2 \cdot 10^{-6}$ sec, which is the longest mean life with the exception of the neutron [55]. It decays via the weak interaction. The most probable decay modes of the muon and the anti-muon, previously given in Table 2.2, are the following; muon decays into an electron, an electron anti-neutrino and a muon neutrino while anti-muon decays into a positron, an electron neutrino and a muon anti-neutrino. The Feynman diagram for the muon decay is illustrated in Figure 3.3.

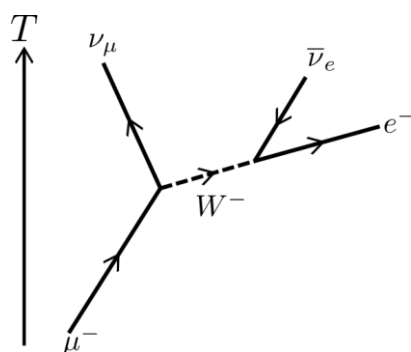


Figure 3.3. The Feynman diagram for the muon decay

Nearly all of the rest energy of a stopped muon is shared by the decay products as the kinetic energies. While some of the rest mass energy of the muon appears as the kinetic energy of the electron (or positron), the rest of the energy is carried by the neutrino and anti-neutrino. Therefore, the energy of the electron (or positron) from muon decay varies depending on the momentum directions of the neutrinos and anti-neutrinos. For example, the electron has a maximum energy of $\sim 53 \text{ MeV}$ when both

neutrino and anti-neutrino recoil against the electron. The experimental and theoretical momentum spectra of the outgoing positron in the decay of the positive muon are shown in Figure 3.4.

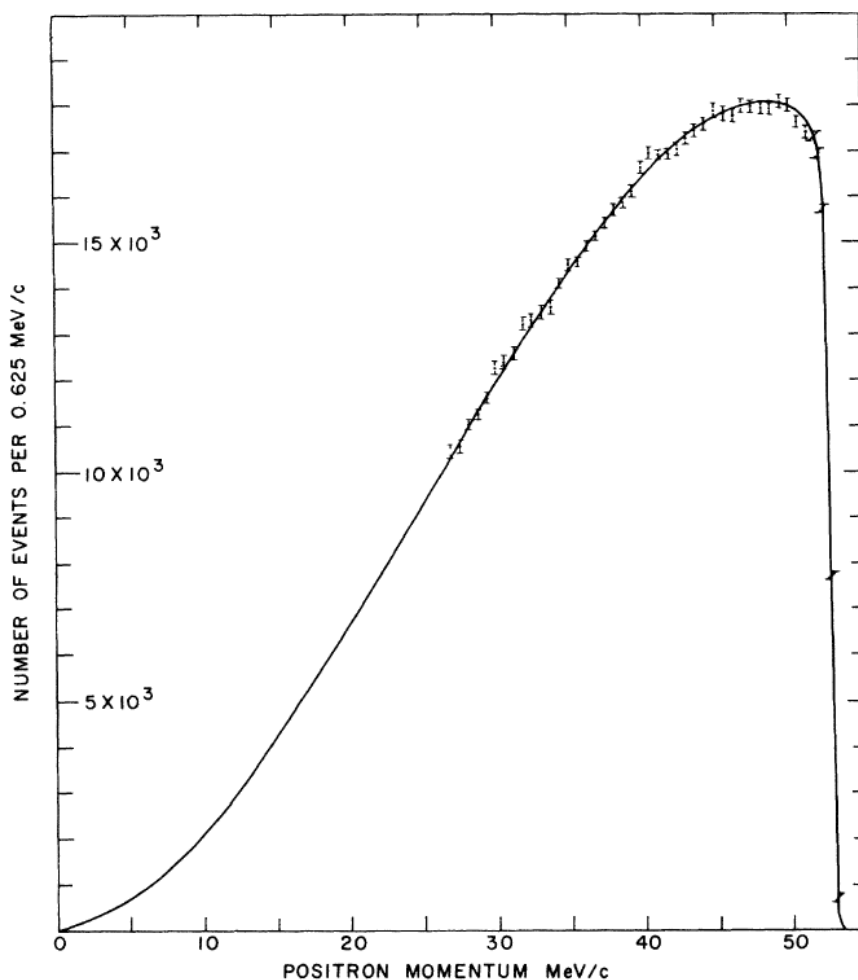


Figure 3.4. Experimental points and theoretical curve for the momentum spectrum of the positron in the decay of $\mu^+ \longrightarrow e^+ + \nu_e + \bar{\nu}_\mu$ [106]

Both the negative and positive muons are subject to the electromagnetic and weak interactions with the media they propagate in, similar to the electron and positron respectively. However, their interactions with the molecules present in the surrounding media can also cause the formation of unusual structures. For example, when a fast-moving positive muon decelerates to low energies in an ordinary matter, it can capture an electron and forms an exotic atom known as the *muonium* [107]. Muonium behaves like a light, radioactive hydrogen isotope, in which the muon acts as the nucleus, and its Bohr radius is very close to that of the hydrogen atom.

In addition, the negative muons can bind to the nuclei of some atoms like carbon and hydrogen, which make the material they pass through, in the same way as electrons do. The atoms in which the electrons are replaced with negatively charged muons are known as the *muonic atoms*. A muonic hydrogen atom, for example, has a radius of roughly 200 times smaller than the ordinary hydrogen atom due to the larger mass of the muon. When only one electron of a multi-electron atom is replaced by a muon, the muon gets closer to the nucleus than the atomic orbitals of the electrons. Therefore, the size of the atom, which is determined by the other electrons, remains nearly unchanged. Because of its proximity, a muon in a muonic atom can be captured by the nucleus via the semi-leptonic reaction



which is mediated by the weak interactions. Nuclear capture rate of a muon by a nucleus depends on the atomic number (Z) of the nucleus, and is roughly proportional to Z^4 [108].

The decay time probability for muons follows an exponential decay law similar to the law of radioactive decay. The distribution of the muons $N(t)$ as a function of time (t) can be described as

$$N(t) = N_0 e^{-t/\tau} , \quad (3.2)$$

where N_0 and τ are the normalization parameter and mean muon lifetime respectively. Therefore, $N(t) - t$ graph plotted with the ordinate in the logarithmic scale has a linear form and its slope gives the muon lifetime. The numbers of positive and negative muons in aluminum as a function of the time, indicating the disintegration rates, are given in Figure 3.5.

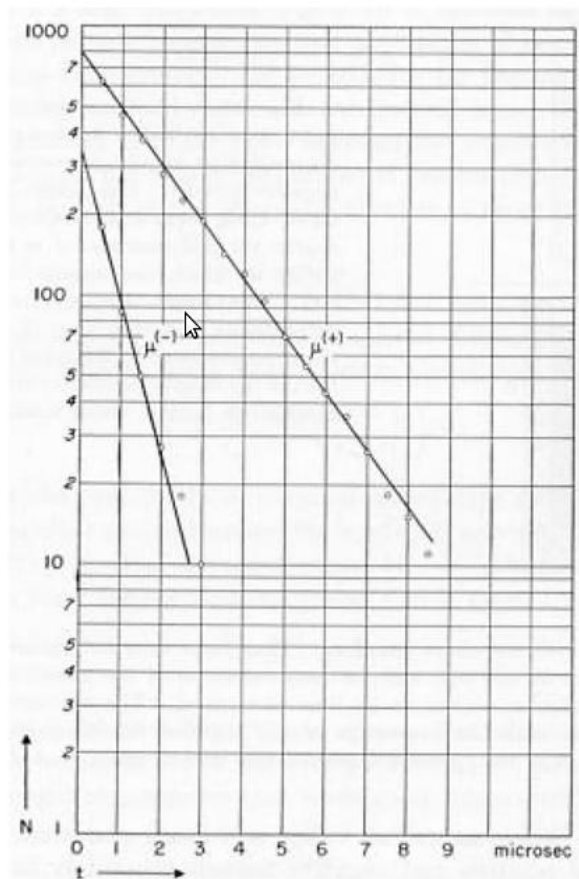


Figure 3.5. Disintegration curves for positive and negative muons in aluminum [109]

As it can be seen from the figure, the slope for the positive muons is smaller than that for the negative ones. As discussed above, there are more ways for a negative muon to disappear during the propagation in a medium compared to the positive one. Therefore, the lifetime of negative muons is found to be somewhat less than that of the positively charged ones while they are passing through a material.

In addition, the mean lifetime of the negative muon in a material becomes shorter with increasing atomic number of the material because of the competition with the nuclear capture. This situation is clearly seen in Table 3.1, where the mean lifetimes of the negative muon in several materials with different Z are listed. As an example, the lifetime of the muon in lithium is close to $2.2 \mu\text{s}$, which is the muon lifetime given in the literature, it decreases by more than 10 times in iron.

Table 3.1. Mean lifetimes of the μ^- in several materials [110]

Material	Z (Z_{eff})	Mean lifetime (ns)
Li	3 (2.94)	2177 ± 2.0
O	8 (7.49)	1795 ± 2.0
Na	11 (9.95)	1204 ± 2.0
Al	13 (11.48)	864 ± 1.0
Ca	20 (16.15)	333 ± 1.5
Fe	26 (19.59)	206 ± 1.0
Ag	47 (27.95)	87 ± 1.5

3.2.1. Energy loss of muons in matter

Energy loss mechanism of the muon by the interaction with the media it propagates in is similar to that of the electron. However, muons are not sharply accelerated by the electromagnetic fields because of their bigger masses, and they suffer less energy loss than electrons from the emission of the bremsstrahlung radiation. Consequently, muons are more capable of penetrating deeply into matter than electrons insomuch that the cosmic ray muons can reach deep underground levels passing through large thickness of rock sample depending on their energies.

Muons propagating in matter lose energy via the mechanisms such as *ionization*, *atomic excitation*, *direct electron pair production*, *bremsstrahlung radiation* and *photo-nuclear interactions*. The energy loss rate due to the ionization and atomic excitation, which is indicated by the parameter α , depends weakly on muon energy and chemical composition (average Z/A ratio) of the medium. Therefore, it is accepted to be nearly constant for relativistic particles in numerical estimates. Each of the other mechanisms, on the other hand, depends on average Z^2/A ratio of the medium in addition to muon energy. The mathematical expressions describing the

dependencies of these mechanisms are relatively complex. However, the total energy loss relation for muons can be parameterized, in general, with the expression

$$-\frac{dE_\mu}{dX} = \alpha + \beta E_\mu, \quad (3.3)$$

where X is the thickness of the crossed material in g cm^{-2} and β is sum of the fractional energy losses resulting from bremsstrahlung, pair production and photo-nuclear interactions ($\beta = \beta_{\text{br}} + \beta_{\text{pp}} + \beta_{\text{ph}}$) [111]. Calculation results for the energy loss parameters, α and β , of the muons with different energies in standard rock (see Section 3.5 for definition of standard rock) are given in Table 3.2.

Table 3.2. The energy loss parameters α and β calculated for standard rock [112]

E_μ GeV	α MeV/(g cm ⁻²)	β_{br}	β_{pp}	β_{ph}	β
		[10 ⁻⁶ (g cm ⁻²) ⁻¹]			
10	2.17	0.70	0.70	0.50	1.90
100	2.44	1.10	1.53	0.41	3.04
1000	2.68	1.44	2.07	0.41	3.92
10000	2.93	1.62	2.27	0.46	4.35

For simplicity, the parameter α is accepted to have a constant value of 2 MeV/(g cm⁻²). The value of β , which is in the order of 10⁻⁶ g⁻¹ cm², depends on the Z^2/A ratio of the medium that muon propagates in and muon energy. The energy at which two energy loss terms are equal is defined as the *critical muon energy* (E_μ) below which the energy loss rate due to the ionization and atomic excitation dominates. The critical energy for muons propagating in rock is $E_\mu = \alpha/\beta \approx 500$ GeV. Therefore, the energy loss of the muon with energy well below this value can be calculated approximately using the formula

$$\Delta E_{\mu} = \int \alpha dX = \alpha X = 2 \text{ MeV} / (\text{g}\cdot\text{cm}^{-2}) X , \quad (3.4)$$

which is derived from Equation 3.3. The average energy of a muon ($\langle E_{\mu} \rangle$), with initial energy E_0 , after travelling through $X \text{ g cm}^{-2}$ of material can be calculated using the formula

$$\langle E_{\mu} \rangle = (E_0 + \epsilon_{\mu}) e^{-\beta X} - \epsilon_{\mu} , \quad (3.5)$$

which is a general solution of Equation 3.3. Therefore, the minimum energy of a muon required to penetrate the thickness X is found simply by setting $\langle E_{\mu} \rangle = 0$ in Equation 3.5;

$$E_0^{\text{min}} = \epsilon_{\mu} (e^{\beta X} - 1). \quad (3.6)$$

Thickness of the material X is also known as the *interaction depth*, which is in units of g cm^{-2} . The number of interactions particles have during the propagation (and also the interaction depth) is proportional to the density of the medium times the path length. Multiplication of the density and the path length in units of g cm^{-3} and cm , respectively, yield the interaction depth, X , in units of g cm^{-2} . Interaction depth in such unit allows for comparison of the effects of passage through different sort of materials with different dimensions. For example, the interaction depth of a uniform lead plate (density of $\sim 11.34 \text{ g cm}^{-3}$) with a thickness at 88 cm is equal to that of 10 meters in water. In some cases, the unit of *meter water equivalent* (m.w.e.) is also used for depth, where the units can be converted to each other according to the relation of $100 \text{ g cm}^{-2} = 1 \text{ hg cm}^{-2} = 1 \text{ m.w.e.}$

3.2.2. Cosmic ray muons

Cosmic ray muons are mostly produced at an altitude of ~ 15 km above the sea level as the result of decays of unstable mesons, which are produced by the interactions of the primaries with the atmospheric nuclei. Although the main contributors to the cosmic muons are charged pions and kaons, some charmed particles such as D^\pm , D^0 , J/ψ also play a role in the muon formation. The relative contribution of the kaons on the muon intensity increases with the increasing energy. Although nearly 5% of the vertical muons come from the kaons at lower energies, this ratio increases to 8% and 19% at 100 GeV and 1000 GeV muon energies, respectively [1].

Considering Equation 3.4 and the vertical depth of the atmosphere which is about 1000 g cm^{-2} , one can conclude that muons lose nearly 2 GeV due to ionization before they reach the ground. This might mean that muons with energies lower than 2 GeV at the top of the atmosphere will most probably decay in flight before reaching the ground. The mean energy of cosmic muons at ground level is about 4 GeV, and therefore their mean energy at the site of production is expected to be ~ 6 GeV [55].

Muons' arrival at the ground and penetration to underground could be attributed not only to their small interaction cross section and small energy loss passing through a medium but also to their relatively long lifetime as well. However, the lifetime of $2.2 \mu\text{s}$ was expected to allow the muons to travel only about 650 m distance before they decay. Propagation of the muons through kilometers without disintegration is a confirmation of the relativistic time dilation, which is one of the postulates of the special theory of relativity. The first experiment, which verifies the time dilation of moving clocks predicted by A. Einstein, was performed by B. Rossi and D.B. Hall [113]. In the experiment, muon fluxes measured in two different locations with a difference in the altitude of 1624 m were compared. Although the travel time of such distance for the muons is several muon lifetimes, the difference between the muon fluxes measured in both altitudes was very little. This finding was consistent with the relativistic prediction. In subsequent years, many similar experiments with convincing results were performed by different groups (see, for example, [114]).

3.3. Cosmic Muons at Ground Level

Cosmic muons are the most numerous secondary cosmic particles at ground level after the photons and neutrinos (see Figure 2.14). They represent approximately 80% of the charged components of the secondary cosmic rays at sea level. The integral flux of the muons at sea level with energies above 1 GeV is about $70 \text{ m}^{-2}\text{sr}^{-1}\text{s}^{-1}$ [115]. In general, one can say that one cosmic muon passes through a 1 cm^2 horizontal area per minute. Both differential and integral vertical muon intensities for some momentum values from a detailed spectral measurement [116] are summarized in Table 3.3.

Table 3.3. Best-fit for differential and integral muon spectra for the vertical direction [116]

Muon momentum (GeV/c)	Differential intensity ($\text{cm}^{-2} \text{sr}^{-1} \text{s}^{-1} (\text{GeV}/c)^{-1}$)	Integral intensity ($\text{cm}^{-2} \text{sr}^{-1} \text{s}^{-1}$)
0.5	2.94×10^{-3}	8.69×10^{-3}
1.0	2.62×10^{-3}	7.29×10^{-3}
5.0	5.17×10^{-4}	2.27×10^{-3}
10.0	1.35×10^{-4}	9.05×10^{-4}
25.0	1.45×10^{-5}	1.96×10^{-4}
50.0	2.11×10^{-6}	5.35×10^{-5}
100.0	2.77×10^{-7}	1.28×10^{-5}
250.0	1.50×10^{-8}	1.58×10^{-6}
500.0	1.45×10^{-9}	2.93×10^{-7}
1000.0	1.31×10^{-10}	5.16×10^{-8}
2000.0	1.13×10^{-11}	8.81×10^{-9}
3000.0	2.67×10^{-12}	3.11×10^{-9}

Vertical muon intensities at the ground measured by different groups are illustrated in Figure 3.6 as a function of the muon energy. Also in the figure are shown the

calculated spectrum for the ground level muons (solid line) together with the calculations with the exclusion of the decay and energy loss mechanisms for the muons (the dotted line).

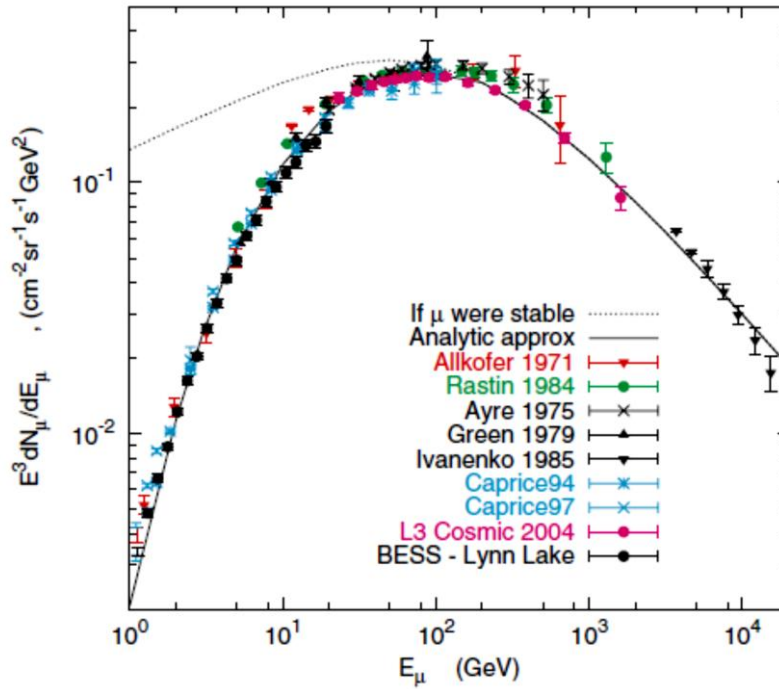


Figure 3.6. Some measurements (markers) and calculation results (lines) for the energy spectrum of the cosmic muons at the ground (see [117] and references therein)

The muon flux at sea level for high energy region (above 100 GeV) could be described by an analytic expression, known as the Gaisser's formula [1]:

$$\frac{dN_{\mu}}{dE_{\mu}d\Omega} \approx \frac{0.14E_{\mu}^{-2.7}}{\text{cm}^2 \text{ s sr GeV}} \times \left\{ \frac{1}{1 + \frac{1.1E_{\mu} \cos \theta}{115 \text{ GeV}}} + \frac{0.054}{1 + \frac{1.1E_{\mu} \cos \theta}{850 \text{ GeV}}} \right\} \quad (3.7)$$

Since the formula, in which E_{μ} is the muon energy and θ is the zenith angle, was developed by omitting the muon decay, it is not successful in describing the experimental results at low energy. In addition, the formula is valid for the case where the curvature of the Earth is neglected which requires the zenith angle cut of $\theta < 70^{\circ}$.

The values of 115 GeV and 850 GeV in Equation 3.7 are the critical energies (\mathcal{E}_π and \mathcal{E}_K), at which the interaction probability in the atmosphere equals the decay probability for pion and kaon, respectively. High energy pions with energies above \mathcal{E}_π most probably interact with the atmospheric nuclei and produce further pions before they decay. Since the produced pions have lower energies, their decay products, muons, have lower energies as well. This situation causes the muon spectrum at high energies to be steeper than that of the parent primaries.

The spectrum of the muons with energies in the interval of $\sim 10 - 100$ GeV is almost determined by the distribution of the primaries and the hadronic interaction they are exposed. For lower energies, decay and the energy loss of the muons play an important role in the formation of the spectral shape. In addition, below a few GeV, the spectrum depends on the geomagnetic latitude, the altitude, the atmospheric conditions of the experimental site and the solar activity.

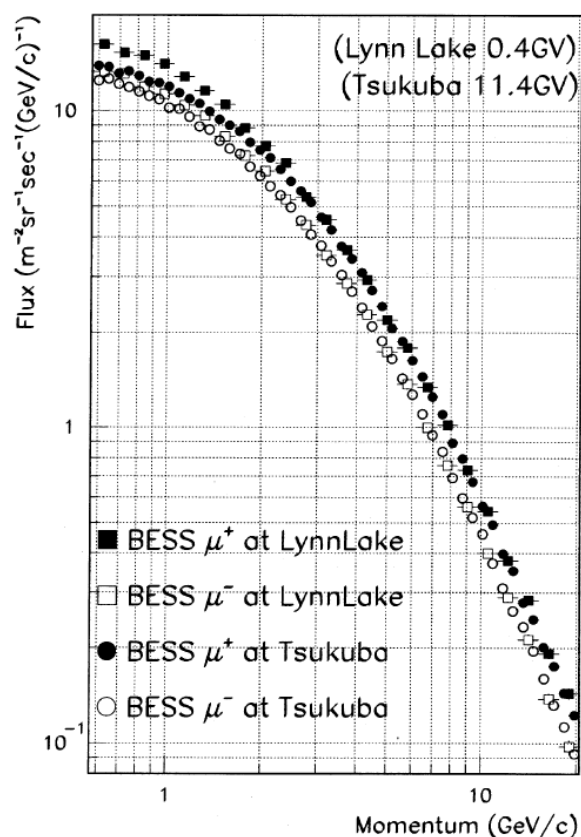


Figure 3.7. BESS results for the negative and positive muon spectra at two different locations [119]

The BESS (Balloon-borne Experiment with Superconducting Spectrometer [118]) results for the absolute fluxes of both negative and positive muons at Lynn Lake, Canada (0.4 GV) and Tsukuba, Japan (11.4 GV) are shown in Figure 3.7. Since the geomagnetic cut-off rigidity in Tsukuba is much higher than the one in Lynn Lake, comparison of the muon spectra obtained at these locations allows observation of the effect of the cut-off rigidity. As it can be seen from the figure, the muon fluxes measured in Tsukuba are somewhat smaller than the ones in Lynn Lake for lower momenta, especially below 5 GeV/c. However, the muon fluxes for both locations are in good agreement for higher momentum region. This is because the cut-off rigidity does not affect the higher energy primaries, which are responsible for the production of high energy muons.

Low energy cosmic muon flux changes annually depending on the effect of the solar modulation. Since the low energy primary proton flux changes according to a temporal variation due to solar modulation, the flux of the secondary muons with low energies also changes. Low energy muon flux is expected to reach the maximum value at solar minima, one of which was happened in 1996 – 1997.

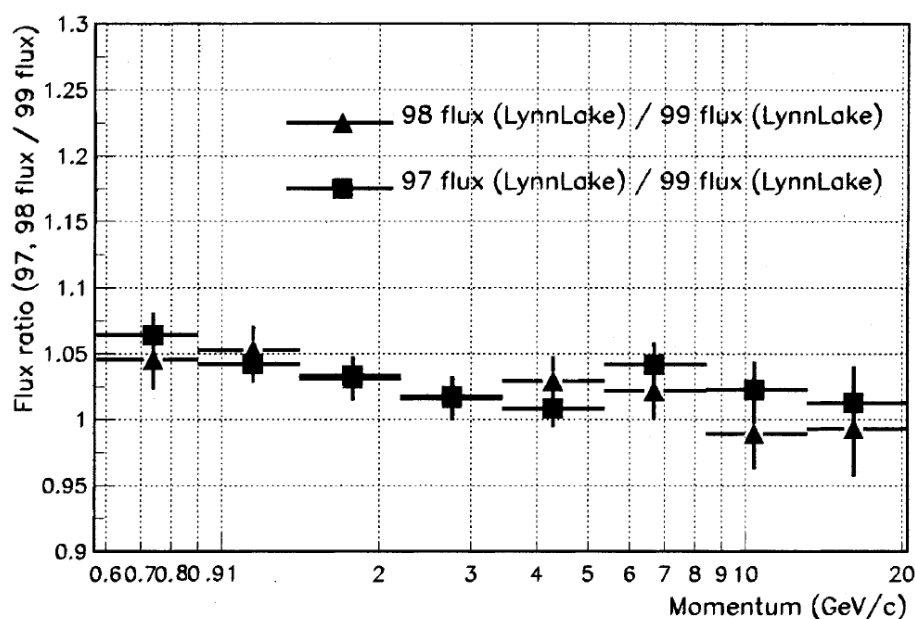


Figure 3.8. BESS results for the annual variation of the muon flux in Lynn Lake [119]

In Figure 3.8, the muon fluxes measured in Lynn Lake in 1997 and 1998 are divided by the ones obtained in 1999. It is clearly shown that the flux in 1999 is lower than the other fluxes especially below the muon momentum of 3 – 4 GeV/c. This finding clearly exhibits the effect of solar modulation on the ground level muon distribution.

3.3.1. Angular dependence of the muon intensity

The parent particles of the muons, mainly pions and kaons, may either decay or interact with the atmospheric nuclei during their propagation towards the ground. Probability of the decay or interaction depends on the parent mesons' energies and the density of the atmosphere along their trajectories. For large zenith angles, the parent mesons at high altitudes travel relatively longer distances in the low density part of the atmosphere, which increases their decay probability compared to the interaction probability. Decays of the parent mesons before the interactions lead to an enhancement in the intensity of high energy muons. Consequently, the flux of the high energy muons with a larger zenith angle at the ground level is greater than the vertical one.

The situation is a bit different for the intensities of low energy muons. Cosmic muons with nonvertical trajectories travel through longer paths than the vertical ones before reaching the ground. Therefore, muons with larger zenith angles, compared to the ones with smaller angles, lose more energy with the interaction of atmospheric gasses. Furthermore, some of the muons with low energies, enough to make them reach the ground along the vertical paths, are not able to arrive the Earth's surface because of the decays and absorption effects. As a result, intensities of the low energy muons incident with a large zenith angle are expected to be smaller than that of the vertical muons at the surface. One should note that, the total muon intensity also decreases with the increasing zenith angle since the total muon intensity is dominated by low energy ones.

Momentum spectra of the vertical muons are given in Figure 3.9 together with the momentum distribution of the muons with 75° zenith angle. Previously discussed effect of the zenith angle on the muon intensity is clearly seen from the figure, in

which the measurement results of various experiments (see [55] and the references therein) are illustrated. More clearly, intensity of the muons with zenith angle 75° is greater than that of the vertical one above ~ 100 GeV/ c although the situation is opposite for lower momenta.

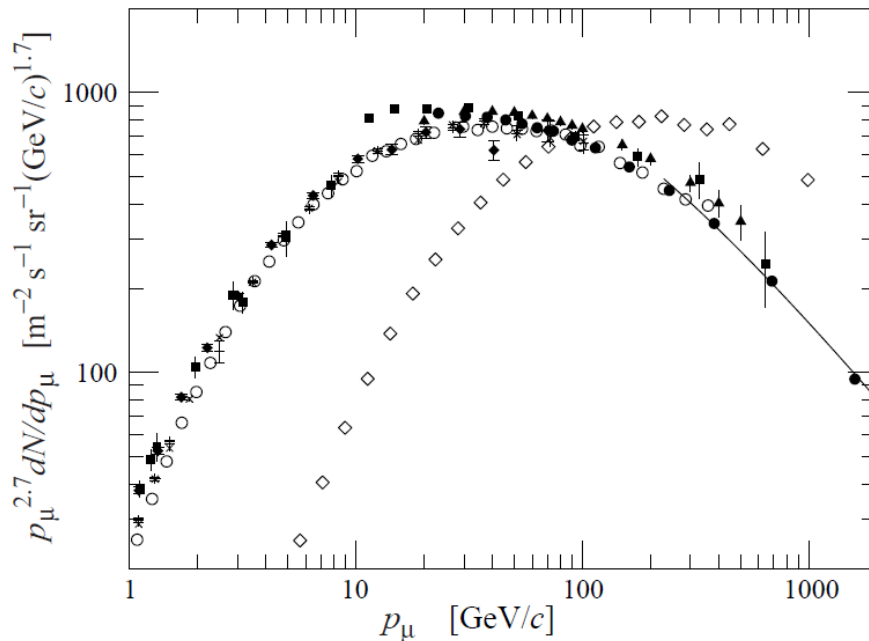


Figure 3.9. Momentum spectrum of muons with zenith angle $\theta = 75^\circ$ (blank diamonds) and those of the vertical muons (the rest of the markers) [55]

The zenith angle dependence of the cosmic muon intensity, in the case that the curvature of the Earth is neglected ($\theta < 70^\circ$), can be described by the expression

$$I(\theta) = I(0^\circ) \cos^n \theta, \quad (3.8)$$

where $I(\theta)$ is the intensity at zenith angle θ , $I(0^\circ)$ is the vertical intensity and n is the exponent, which is a function of muon energy. For the total intensity of the ground level muons, the exponent has a value of $n = \sim 2$, which is the characteristic of muons with ~ 3 GeV energy [55]. The n value decreases with the increase in the muon energy, so that the angular distribution of the high energy muons approaches to $\sec \theta$ distribution. Monte Carlo calculation results for the ratio of the inclined muon flux to

that of vertical ones at ground level are illustrated in Figure 3.10 as a function of cosine of the zenith angle for different muon momenta.

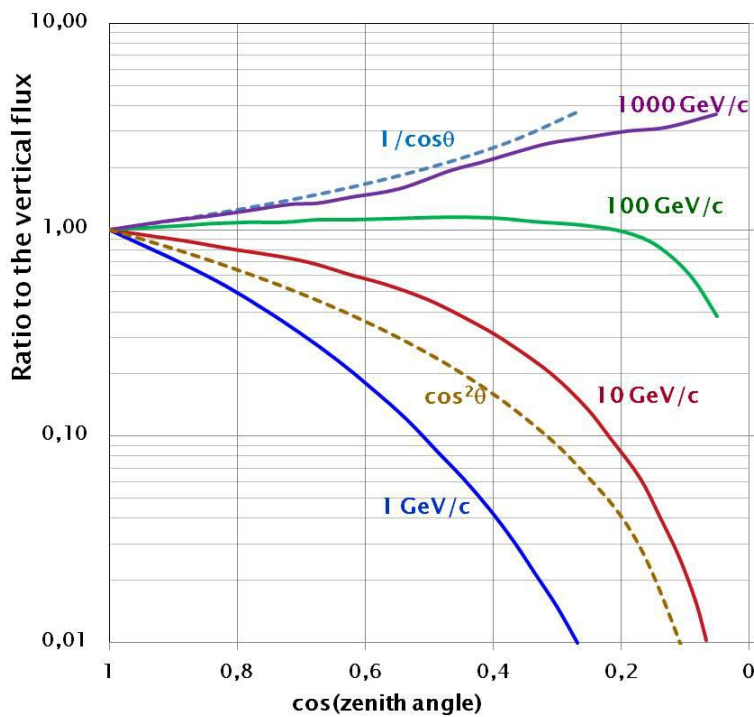


Figure 3.10. Monte Carlo calculations of the ratio of the inclined muon flux to the vertical muon flux at ground level as a function of cosine of the zenith angle for different muon momenta [111]

As it is seen from the figure, muons with the momentum 1 GeV/c have an angular distribution defined in the Equation 3.8 with $n > 2$. In addition, the distribution of the muons with 100 GeV/c momenta is almost flat up to $\cos \theta = 0.2$, which means that the flux of 100 GeV/c muons is independent from the zenith angle, and then it declines sharply. Furthermore, the flux of the muons with 1 TeV/c increases with the increase in zenith angle approaching to a $\sec \theta$ distribution.

The flux of positively charged primary cosmic rays that reach the Earth's atmosphere from the western direction is greater than the one from the eastern direction. This influence, called the East–West effect, has been discussed in more detail in Section 2.1. Since the secondaries propagate almost in the same direction with their parent primaries, cosmic muon intensity at low energies shows an azimuthal dependence as well. The asymmetries in the fluxes of the secondary particles like muons and neutrinos have been previously reported in various studies [120-122].

In addition, positive (negative) muons coming from the western (eastern) direction are bent down by the geomagnetic field, which causes them to follow a shorter path than the negative (positive) ones to reach the ground. Similarly, the negative (positive) muons coming from the West (East) are bent up by the field, yielding a longer path and more interaction with the atmosphere. This effect becomes more remarkable especially at large zenith angles of muon incidence and at lower muon energies.

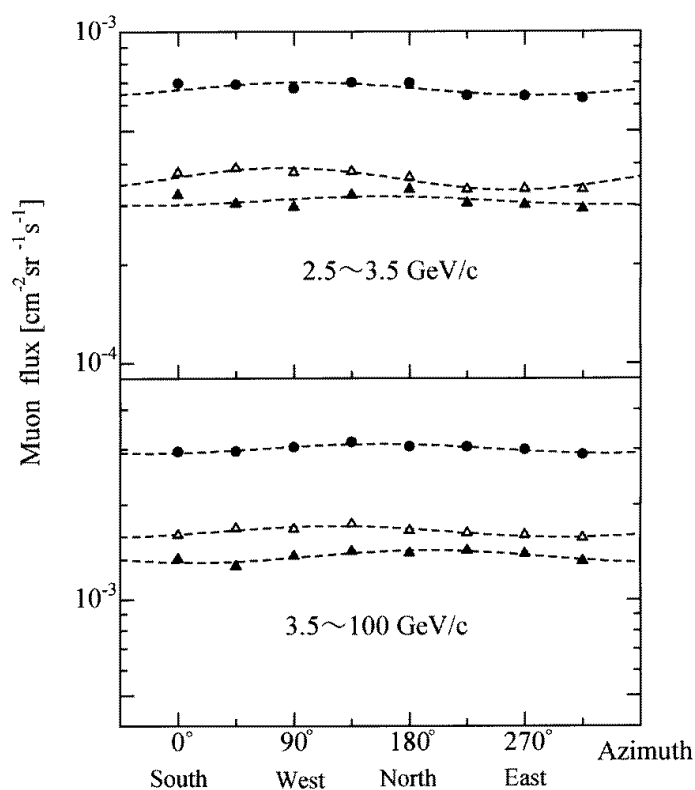


Figure 3.11. The azimuthal angular dependence of the muon fluxes for the zenith angles $40^\circ \pm 5^\circ$ for different momentum intervals. Open and full triangular markers represent the positive and negative muon flux respectively. The circular marker is for the total flux, and the dashed lines are the fit curves [123]

The variation of the muon fluxes as a function of the azimuthal angle for different momentum intervals (2.5–3.5 GeV/c and 3.5–100 GeV/c) with the zenith angles $40^\circ \pm 5^\circ$ are shown in Figure 3.11. As it can be seen from the figure, the fluxes in the lower momentum interval fluctuate more than the ones in higher momentum region. In addition, the azimuth angle dependence of the negative and positive muon fluxes have different profiles. This fact will be illustrated more clearly in the next subsection with the concept of the muon charge ratio.

3.3.2. Muon charge ratio

Interaction of the primary cosmic rays, which consist almost entirely of positively charged particles, with the atmospheric nuclei produces not only positive but also negative charged secondary particles. However, the positive charge excess is transferred to the secondaries like pion, kaon and eventually muon. As a result, the *muon charge ratio*, which is defined as the number of positively charged muons over the negatively charged ones, becomes greater than unity. Muon charge ratio, obtained from various experiments, is illustrated in Figure 3.12 as a function of the muon momentum.

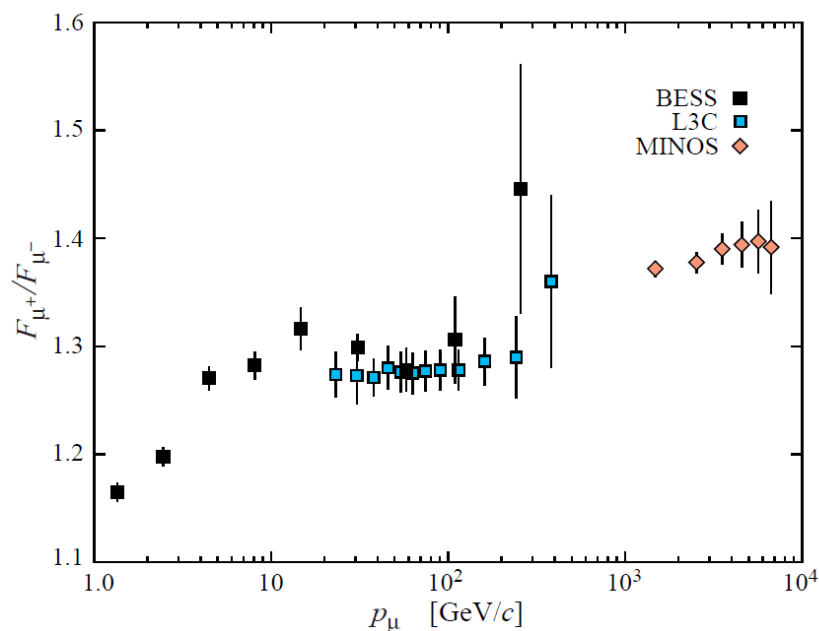


Figure 3.12. Experimental muon charge ratio as a function of the muon momentum (see [55] and references therein)

In the interval extending from a few GeV/c to TeV/c, the muon charge ratio is almost independent of the momentum within the experimental errors and its mean value for the vertical muons was reported to have a constant value close to 1.3 in the literature [124, 125]. For the muon energies $E_{\mu} > E_K$, charge ratio has higher values since the kaon contribution for muon production becomes important. Positively charged kaons (K^+) are generated much more than the negative ones in the cosmic rays. Therefore,

largeness of the kaon charge ratio (K^+/K^-) than that of the pions (π^+/π^-) causes to increase in the muon charge ratio in the high energy region [126].

In addition, at low momenta (below a few GeV/c), the muon charge ratio depends on the geomagnetic latitude and on the azimuthal direction. It was previously stated in detail (see Section 3.3.1) that the muons approaching from different azimuthal direction has different path lengths before they reach the ground under the influence of the geomagnetic field. Positive muons coming from the East have longer path length than the negative ones, while the positive muons coming from the West follow a shorter path than the negative ones to reach the ground. This physical phenomenon results in a decrease (an increase) in the charge ratio for the particles coming from the East (West).

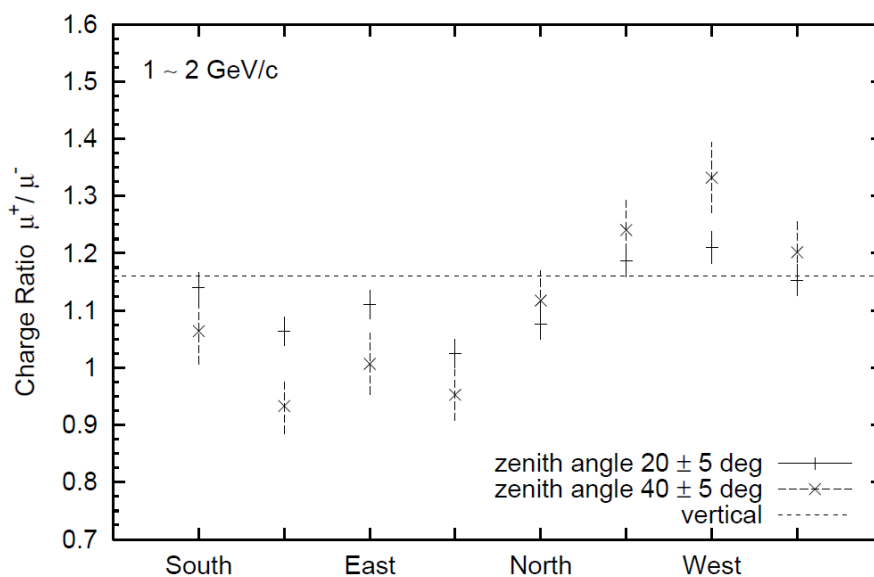


Figure 3.13. The azimuthal dependence of the muon charge ratio for zenith angles 20° and 40° in the momentum range $1 - 2 \text{ GeV}/c$ [127]

Measurement results for the charge ratio of the cosmic muons within the momentum range $1 - 2 \text{ GeV}/c$ and for different azimuthal directions at zenith angles 20° and 40° are shown in Figure 3.13. It is clearly seen from the figure that the muon charge ratio in the lower momentum region shows an azimuthal dependence that becomes more distinctive especially for larger zenith angles.

3.4. Cosmic Muons in the Atmosphere

For the studies of the cosmic rays in the atmosphere, the amount of the matter (gas) above any atmospheric layer is an important parameter to describe the interactions and the propagation of the particles. The term used for this purpose is the *atmospheric depth* (X), which is in the unit of g cm^{-2} and defined as the integral in the altitude of the atmospheric density above a certain level. The vertical atmospheric depth at an altitude h is calculated through the *barometer formula*, which can be written in the simplest form for a standard isothermal exponential atmosphere as

$$X(h) = X_0 e^{-h/h_0}, \quad (3.9)$$

where X_0 is the atmospheric depth at sea level (1030 g cm^{-2}) and h_0 is the scale height of the atmosphere with a value of about 8.4 km [111]. For the inclined trajectories, the atmospheric depth can be calculated simply by multiplying the vertical depth with the secant of the zenith angle for the cases where the Earth's curvature is neglected ($\theta < 70^\circ$).

While the muon measurements at ground level were performed extensively in the past, measurements in the atmosphere were not as much as the ones at sea level and the available ones are limited by a short range of altitude. Measurements of the high altitude muons have been performed using the balloon-borne detectors in addition to the air plane-borne ones and the ones located at mountain sites (see, for example, [128–130]). Recent measurements of the muon flux as a function of the altitude (see [131]) have been made using a balloon-borne cosmic ray detector at the altitude of ~ 40 km, which corresponds to $\sim 5 \text{ g cm}^{-2}$ atmospheric depth.

Balloon measurement results for the momentum spectra of negative muons for nine atmospheric depth intervals are illustrated in Figure 3.14. Focusing on the spectra scaled by 1, one can clearly observe that the muon flux in the lower momentum region increases as the atmospheric depth decreases from 1000 g cm^{-2} to $250\text{--}350 \text{ g cm}^{-2}$. However, the effect of the atmospheric depth on the muon flux

diminishes as the muon momentum increases such a way that it almost disappears above 10 GeV/c.

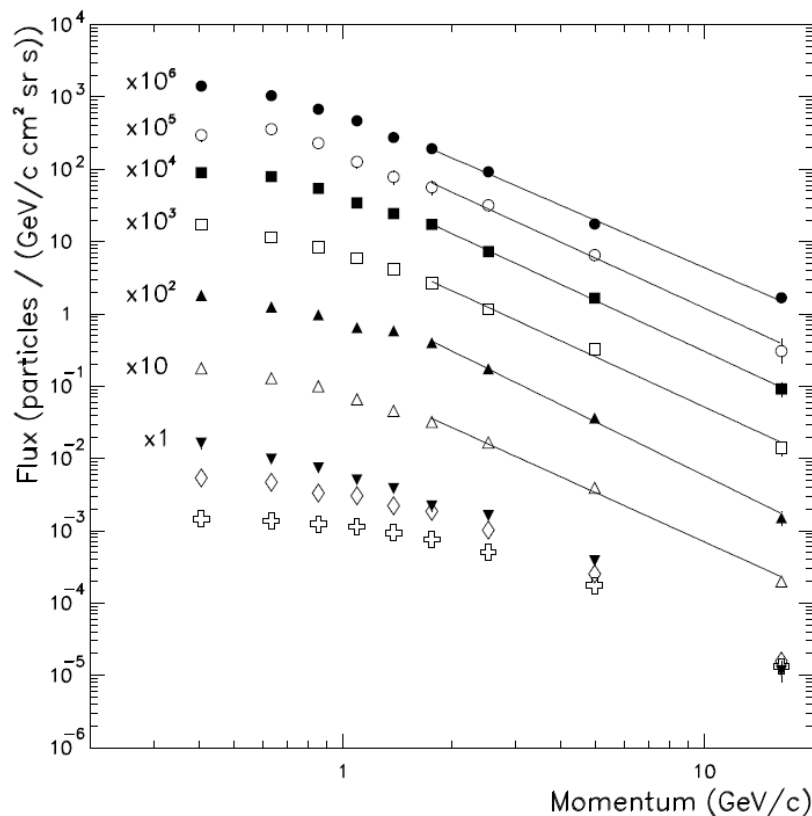


Figure 3.14. Momentum spectra of negative muons for several atmospheric depths. Depth ranges from the top to the bottom are: 3.3–4.6 g cm⁻² (x10⁶), 7–25 g cm⁻² (x10⁵), 25–70 g cm⁻² (x10⁴), 70–115 g cm⁻² (x10³), 115–165 g cm⁻² (x10²), 165–250 g cm⁻² (x10), 250–350 g cm⁻² (x1), 350–850 g cm⁻², 1000 g cm⁻². Solid lines are the fit to power law [132]

The fluxes of both negative and positive muons with different momentum intervals are illustrated in Figure 3.15 as a function of the atmospheric depth. One can see from the figure that the total muon flux first increases and then decreases with the increasing altitude. Such altitude dependence of cosmic radiation was previously discussed in Section 2.3.

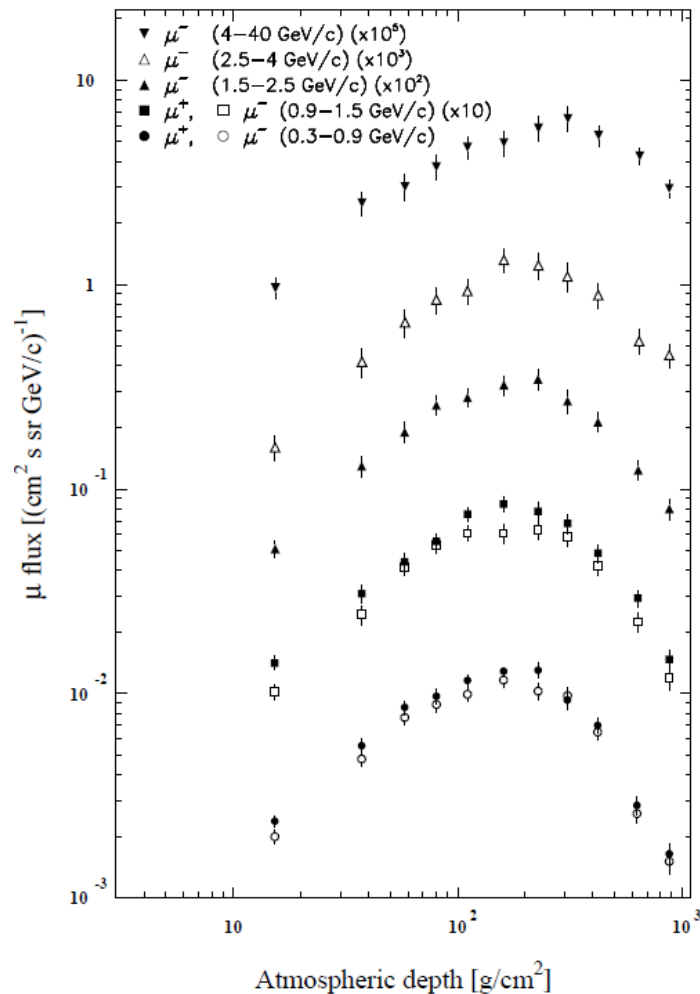


Figure 3.15. Muon flux as a function of the atmospheric depth for different momentum ranges [133]

Muon charge ratios with different momentum intervals have been measured at various atmospheric depths in several experiments. Based on the results of such experiments, no clear correlation of the muon charge ratio with the atmospheric depth has been noticed in the investigated momentum intervals [133–137].

3.5. Underground Muons

The energy spectrum of the muons with energies above a few tens of GeV at sea level is more or less independent from the geomagnetic effect and the solar modulation. Therefore, the intensities of the high energy muons could be accepted as a global constant. However, underground muon spectrum at a proper depth differs based on the properties (average density ρ , charge number Z and atomic mass A) of

the medium. This is because the energy loss mechanism of the muons is heavily dependent on the nature of the medium they propagate in.

As previously discussed in Section 3.2.1, energy losses of the low energy muons are dominated by ionization and atomic excitation which depend mainly on the average Z/A ratio of the medium. At high energies, on the other hand, energy losses of the muons are dominated by pair production and bremsstrahlung radiation, which depend on the average Z^2/A ratio of the medium. Although the average Z/A ratio for most of the rock types is almost equal to the value of 0.50, the average Z^2/A ratio deviates considerably for different rock types. Therefore, different rocks could be considered equivalent up to the depth of ~ 1500 m.w.e., while the rock profiles become important for deeper sites.

Underground muon measurements have been performed in different laboratories located under different rock composition. Therefore, for comparison of the data, it is necessary to take into account the ρ , Z/A and Z^2/A values for the piece of the Earth's crust above the site where the measurements were made. For simplicity, measurements results are usually converted to the ones under *standard rock*, which is defined as rock whose average density $\rho = 2.65 \text{ g cm}^{-3}$ with $Z/A = 0.5$ and $Z^2/A = 5.5$. Averages of the mentioned rock parameters for several sites where the underground muon measurements were performed are given in Table 3.4 together with the properties of the standard rock.

Table 3.4. Average of the rock parameters ρ , Z/A and Z^2/A for several underground sites

Experiment	$\langle \rho \rangle$	$\langle Z/A \rangle$	$\langle Z^2/A \rangle$
Fréjus [138]	2.74	0.498	5.035
Gran Sasso [139]	2.71	0.499	5.690
Kolar Gold Fields [140]	3.02	0.494	6.300
Mont Blanc [141]	2.60	0.494	5.120
Soudan II [142]	2.80	0.496	5.980
Standard rock [143]	2.65	0.500	5.500

3.5.1. Depth-intensity relation

Atmospheric muons are able to penetrate deep underground sites, up to the depth of several km.w.e., depending on their energies (see Equation 3.6). For example, muons with energies 100 GeV and 1 TeV have average ranges of 0.41 km.w.e. and 2.45 km.w.e. in standard rock, respectively [55]. Naturally, it is expected that the muon intensity decreases with the increase in depth as a result of energy loss. In addition to atmospheric muons, neutrino interactions are known to be another source for the underground muons since the mid-1960's [144, 145]. High energy muon neutrinos (and muon anti-neutrinos) produce muons by undergoing the interaction which can be expressed in the form of $(\nu_{\mu}, \bar{\nu}_{\mu}) + N \longrightarrow (\mu^{-}, \mu^{+}) + N'$ in the Earth's crust. These neutrino induced muons were observed in underground laboratories in every direction (including horizontal and upward directions) and their flux has the value in the order of $10^{-13} \text{ cm}^{-2} \text{ sr}^{-1} \text{ s}^{-1}$ above the energy of 1 GeV [146,147]. Because of the low interaction probability of neutrinos, the neutrino induced muon intensity does not depend on the depth. Although contribution of the neutrino induced muons is negligible for shallower depths, they dominate the underground muon intensity at great depths.

Depth-intensity relation for the underground muons could be determined by using the knowledge of sea-level muon distribution together with the energy-loss processes of muons. In addition, intensities of the underground muons with various zenith angles obtained in an individual experiment could be converted into the vertical intensity data for different depths. Therefore, depth dependence of the vertical muon intensity could be studied using a detector located at a specific depth. Vertical intensity of the underground muons is illustrated in Figure 3.16 as a function of depth. The shaded flat part of the graph for large depth shows the intensity of the neutrino induced muons, whose contribution is dominant for the depths greater than ~ 15 km.w.e. in standard rock. The upper (lower) line of the shaded part is for the muons induced by horizontal (vertically upward) neutrinos. The darker shading part shows the measured intensity in the Super Kamiokande experiment [55].

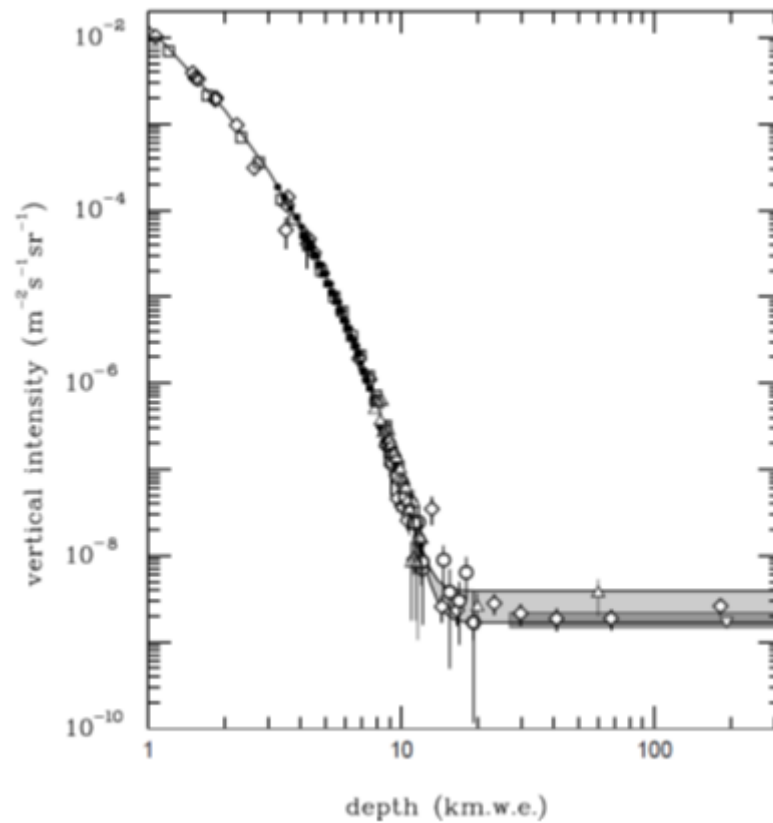


Figure 3.16. Vertical intensity of underground muons as a function of depth [55]

Vertical muon intensity up to the depths where the neutrino induced muons start to dominate the intensity can be described with the expression, which is known as the Fréjus function [148], in the form of

$$I_{\mu}(X) = A \left(\frac{X_0}{X} \right)^2 e^{-\frac{X}{X_0}}, \quad (3.10)$$

where X is the depth in m.w.e. Different values for the parameters A and X_0 are reported from different experiments. For example, results of the measurements made by the Fréjus proton–decay detector yield $A = (1.96 \pm 0.09) \times 10^{-6} \text{ m}^{-2} \text{ sr}^{-1} \text{ s}^{-1}$ and $X_0 = 1184 \pm 8 \text{ m.w.e}$ [148]. For larger depths, the Fréjus function is modified by adding a constant term K , which accounts for the neutrino induced muon component and has a value in the order of 10^{-13} (see, for example, [149]).

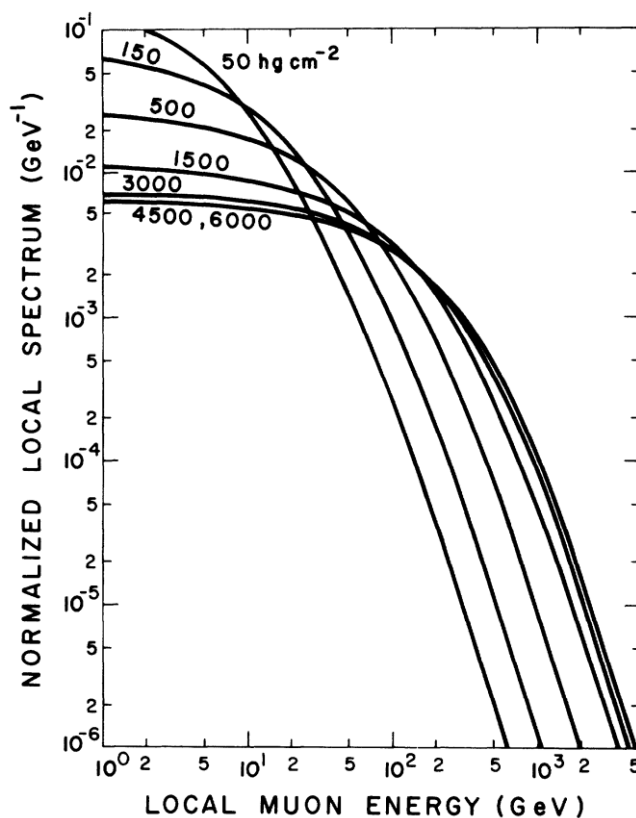


Figure 3.17. Local differential energy spectra of the underground muons at various depths. Each spectrum was normalized to the vertical muon intensity at the corresponding depth [150]

The normalized local energy spectra, which were defined as the differential energy spectra at specific depths normalized to the corresponding integrated intensities, are given in Figure 3.17 for various depths in standard rock. It is seen from the figure that the low energy part of the spectrum gets flatter as the depth increases so that it becomes nearly constant for great depths. For the depths greater than ~ 2.5 km.w.e., the normalized spectrum becomes almost independent of the depth and its high energy part (above ~ 500 GeV) reflects the surface muon spectrum.

3.5.2. Angular dependence of underground muon intensity

As previously discussed in Section 3.3.1, high energy muons are not affected by the geomagnetic field significantly and they show no azimuthal dependence. Since only the energetic muons are able to penetrate significant depths in Earth's crust, underground muons have no azimuthal dependence either. On the other hand, underground muon intensity shows zenith angle dependence. Muons with larger zenith angles, compared to the ones with smaller angles, lose more energy in the medium they propagate through since they are exposed to more interaction. As a result, the intensity of muons incident with a large zenith angle reaching a particular depth is expected to be smaller than that of the vertical muons.

Similar to the sea level muons, the zenith angle distribution of the underground muons at shallow depths could be expressed with cosine power law in the same form as Equation 3.8. By considering the depth dependence of the underground muon intensity, the zenith angle distribution could be formalized as

$$I(X, \theta) = I(X, 0^\circ) \cos^n \theta , \quad (3.11)$$

where X is the depth in m.w.e. The exponent n in the equation is a function of depth in the form of

$$n = 1.53 + 8.0 \times 10^{-4} X + \varepsilon , \quad (3.12)$$

where ε is a small correction coming from muon decay and ionization losses at shallower depths [151]. As it can be clearly seen from Equation 3.12, with the increase in depth the exponent n also increases, which means that the zenith angle distribution of the underground muon intensity gets steeper. Since the neutrino induced muons dominate at greater slant depths, the usage of the Equation 3.11 is limited by different zenith angle intervals for different depths. For example, the equation is inadequate at depths greater than ~ 5000 m.w.e. for zenith angles greater than $\sim 40^\circ$ [151].

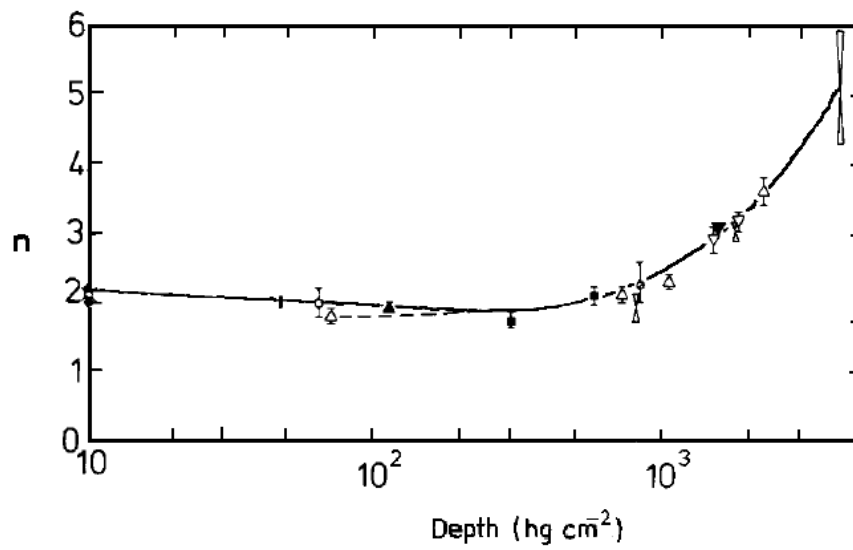


Figure 3.18. Variation of the exponent as a function of depth below the top of the atmosphere (see [152] and references therein)

A compilation of data on the depth dependence of the exponent n for underground muons is illustrated in in Figure 3.18. References for the experimental data could be found in [152]. The solid curve represents the best fit to all the data. The depth in the figure is given below the top of the atmosphere.

CHAPTER 4. GEANT4 MONTE CARLO SIMULATION TOOLKIT

4.1. Monte Carlo Method

Monte Carlo method is a technique that approximates solutions to quantitative problems through statistical sampling. The method is generally used when it is infeasible to compute an exact result with a deterministic algorithm. Although there are a number of isolated and undeveloped early variants of the method (see, for example, [153]), it is accepted that the method was invented by S. Ulam, who is a mathematician worked with J. Neumann on the Manhattan Project during the Second World War. He invented the method in 1946 while he was pondering the probability of winning a card game [154]. N. Metropolis used the term "Monte Carlo" for the method [155], referring to the city of Monte Carlo in Monaco, one of the centers for gambling, considering the similarity between the statistical simulation and games of chance. Then, the Monte Carlo methods were adopted to get the solution for the probabilistic problems concerned with the random neutron diffusion in fissile materials by J. Neumann [156].

In the Monte Carlo method, a random number is selected and the problem is calculated based on this random value. After the result is recorded, the process is repeated for another randomly selected number. A typical Monte Carlo simulation makes the calculations many (thousands or millions of) times by using a different randomly selected value for each. Therefore, the simulation yields a large number of results, which could be analyzed to determine the one with the highest probability.

For trivial problems, using the technique may require more effort than finding an analytical solution. However, using the Monte Carlo technique becomes advantageous as the complexity of the problem of interest increases. This situation is

expressed in Figure 4.1, which shows the time required for solution using the Monte Carlo method and analytic approach as a function of the complexity of the problem.

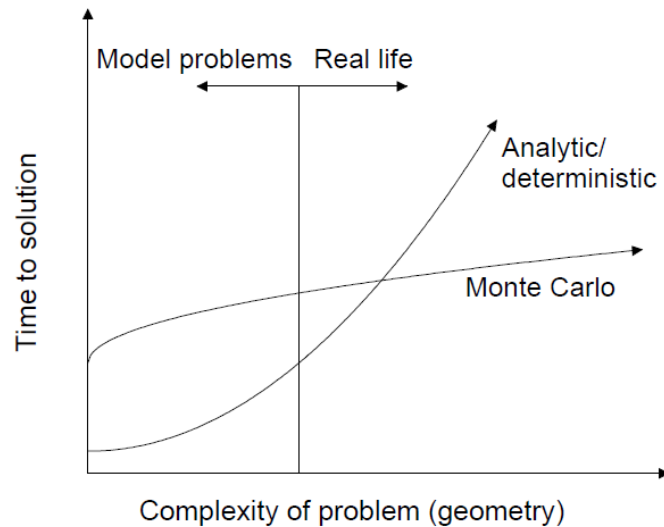


Figure 4.1. The time for solution of the problems, depending on their complexity, using the Monte Carlo method and analytic approach [157]

In addition to yielding the results for the complex problems relatively fast, Monte Carlo simulations offer many more advantages. By running the simulations, one can do the sensitivity analysis and optimization of real system without need to operate it. In addition, effects of the experimental conditions on the results can be controlled better than the real system. However, since the Monte Carlo methods are subject to statistical errors, they become, from this point of view, less advantageous compared to the analytical one.

Today, Monte Carlo method is widely used to develop a reliable parametric picture of a process's outcome in many areas such as from economics to nuclear physics. For example, using the Monte Carlo methods in the study of the propagation of the radiation in a media is very useful since the physical outcome for the interaction of the radiation with matter cannot be predicted with certainty. It is impossible to be sure which interaction type (scattering, absorption, annihilation etc.) a single particle is exposed in a matter. However, all of the possible interactions have their own probabilities to occur based on the properties of the particle and the media. Since, a

beam containing millions of particles (not a single particle) is used in radiation physics, Monte Carlo simulations are very useful in determining the mean behavior of the radiation interacting with the media. Therefore, many Monte Carlo codes, such as Geant4, Fluka [158] and MCNP [159], have been developed to investigate the passage of radiation through matter.

4.2. Geant4 Simulation Package

Geant4 (an acronym for GEometry ANd Tracking) [160, 161] is an object-oriented toolkit for simulation of the passage of particles through matter via the Monte Carlo method. It is developed in CERN in 1998 [162] based on the object-oriented methodology and C++ programming language in spite of the previously released Geant3 tool [163], which was written in FORTRAN. Development and support of Geant4 have been maintained by a large international collaboration including ESA, CERN, and many other institutes and universities around the world. The code, which could be run on operating systems such as Linux, Unix, Mac and Windows, is freely available from the Geant4 website [164].

Geant4 is a powerful tool for the simulation of complex experimental setups in High Energy and Nuclear Physics. Although it was developed for the simulation of the High Energy Physics detectors, it has been extended to a broad area of applications including particle, nuclear, accelerator, medical and space physics thanks to its flexibility and tolerance to evolution. Geant4 simulation software allows the user capabilities for the formation of complicated three-dimensional geometries filled with variety of materials. The user can also track the passage of particles through the defined geometry. In addition to being able to follow the individual particles, it is also necessary to determine their interaction probabilities with the atoms and nuclei present in the medium. Various physics models offered by Geant4 are responsible for performing these tasks. Both primary and the secondary particles, which are formed in the simulation, are tracked step by step until they disappear or come to the end of the defined simulation volume. Most of the physics quantities of the particles such as position, energy and momentum can be obtained at any time during the simulation.

In general, the simulation process for the passage of particles through the matter includes the following aspects:

- i. Geometry and materials
- ii. Particle interaction in matter
- iii. Event and track management
- iv. Digitization and hit management
- v. Visualization and user interface

The geometry, which includes the shape and material, primary particle (type, energy etc.) and the physics model describing the interactions are mandatory to be defined by the user for a Geant4 application. Some other information such as the external electromagnetic fields can also be included depending on the user's need.

4.2.1. Geometry and materials

The Geant4 simulation toolkit has been designed to allow the construction of the geometrical model of the structure, whether simple or complex, to be studied. Particle detectors for the high energy physics experiments, spacecrafts and planets for astroparticle physics, and the human phantom for the medical applications are among the examples of geometrical structures widely modeled using the toolkit.

In general, the geometry in Geant4 refers to the volumes built in the simulation with appropriate materials. A geometry in which particles are propagating in is made of a number of volumes in a hierarchical structure. The largest volume that includes all the parts of the geometry is named as the *world*. The global coordinate system is defined by the world volume in such a way that the origin is at the center of it. When a volume is placed within another volume, the former (latter) one is called as the *daughter (mother)* volume. A mother volume can contain one or more daughter volumes, the positions of which are described with respect to the local coordinate system of their mother volumes. It is crucial for the geometry construction that the daughter volumes do not overlap with each other and do not extend beyond the boundaries of their mother volume.

Geant4 provides definitions of a wide variety of geometrical shapes including not only simple ones, such as boxes, spherical and cylindrical shells, but also specific ones, like polyhedra and hyperbolic tubes. Some of the shapes defined in Geant4 libraries are given in Figure 4.2. The shapes other than the ones defined in Geant4 can be modeled by combining the primitive ones using the Boolean operations like unions, intersections and subtractions.

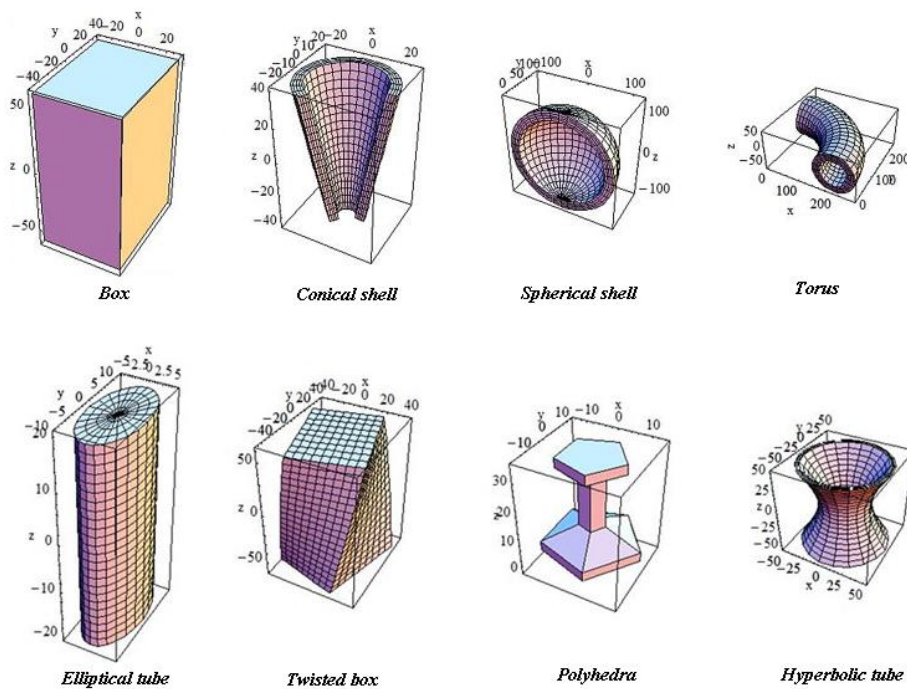


Figure 4.2. Several geometrical shapes defined in Geant4 simulation package [165]

In addition to their shapes, the materials of the volumes must also be determined by the user as mentioned above. This is because the physical processes that the particles undergo during the propagation in a medium depend on the material properties. In nature, materials (molecules, chemical compounds and mixtures) are made of elements, which could have several isotopes. Although Geant4 has libraries in which hundreds of elements, isotopes and materials are defined, it also allows the user to define new materials.

Materials of the modeled volumes in Geant4 can be defined to be made of not only single type of elements but also a mixture of elements (compounds or molecules). In both cases, density, temperature and pressure of the material together with its state (liquid, gas, etc.) must be specified. Materials made of one type of element can be simply defined by describing the properties of the element such as the atomic number and atomic mass. In addition, compounds and molecules must be defined through their constituent elements using their chemical formula or weight fraction.

4.2.2. Particles in Geant4

Geant4 simulation toolkit provides over a hundred pre-defined particle types, including photons, leptons, mesons, baryons, quarks, gluons and ions. In Geant4, an individual particle is characterized with its properties such as name, mass, charge and mean life. In addition to the particles belonging to one of the groups given above, virtual particles called *geantino* are defined in Geant4 libraries as well. Geantino has no charge or mass and does not interact with the medium. Therefore, trajectories of the geantinos are very useful for the verification of the geometrical setup. Charged version of the geantino, the *charged geantino*, is also available in the Geant4 particle list. The charged geantino is also massless and non-interacting, but thanks to its charge, it can be tracked properly in a magnetic field. Trajectory of the charged geantino in a medium depends on both its energy and the strength of the magnetic field.

In a Geant4 simulation, user must define all the details (type, starting position, propagation direction and energy or momentum) of initial particles that are injected into the modeled geometry. Each of these initial properties can be modeled either with a constant value or a distribution function. Therefore, the user can generate the primary particles with a simple model like a monochromatic particle beam or with a complex one by specifying their energy and angular distributions.

4.2.3. Geant4 physics models

The Geant4 toolkit contains a large variety of physics models handling the interactions of particles with matter across a very wide energy range from 250 eV up to several PeV [160]. It is obvious that developing a uniform physics model that covers wide variety of particles and wide energy range is unrealistic. For this reason, Geant4 provides sets of alternative physics models, each of which has been specialized for an area of application. Geant4 does not have any default physics model, and the users are responsible for the selection of suitable models and including them in the physics list according to their applications. Various models are put together in a physics list according to the application domain. The choice of the models should be made by taking into account not only the accuracy but also the speed of the simulation. Although some more sophisticated models yield more realistic results, selection of a model that does not handle the processes in the irrelevant energy regions can potentially save significant CPU time with little or no impact on physics.

The interactions handled in Geant4 are divided into major process categories including electromagnetic, hadronic, optical processes etc. In the next two subsections, electromagnetic and hadronic models are discussed respectively. Detailed information on the physics models could be found in the official website of Geant4 [164].

4.2.3.1. Electromagnetic interaction models

In Geant4, the electromagnetic interactions of leptons, photons, hadrons and ions with matter are described mainly in two categories; *standard* and *low energy* [166]. While the standard package handles the basic processes of electromagnetic interactions, the low energy package provides alternative models extended down to lower energies.

The standard package for the electromagnetic interactions (*emstandard*) includes the processes of ionization, bremsstrahlung, multiple scattering, Compton and Rayleigh

scattering, photoelectric effect, pair conversion, annihilation, synchrotron and transition radiation, scintillation, refraction, reflection, absorption, and the Cherenkov effect for the energies from 1 keV up to 10 PeV [165]. This package has been used for large scale productions in many domains of application.

Geant4 offers the low energy package, which includes alternative models like Livermore and Penelope, for simulation of the electromagnetic interactions of particles with very low energies. The low energy package can perform very detailed simulations for the propagation of particles with energies down to 100 eV. It is obvious that such a detailed simulation requires significantly more CPU resources. This package is utilized in various areas of applications such as medical physics and microdosimetry.

4.2.3.2. Hadronic interaction models

Hadronic interactions are handled in Geant4 by different models, which are valid for specific energy ranges. Some of the hadronic models available in Geant4 are illustrated in Figure 4.3 together with the energy intervals that the models handle.

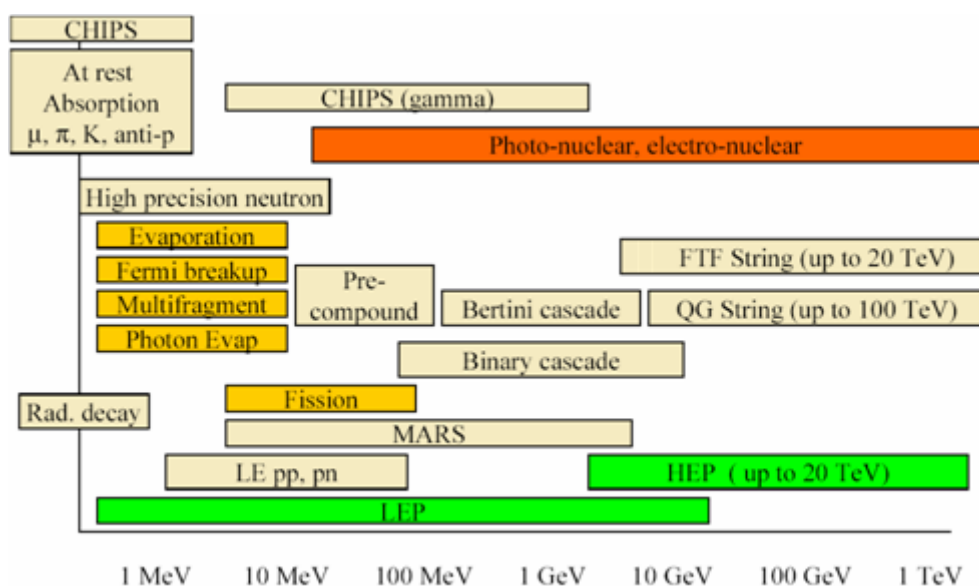


Figure 4.3. Some of the hadronic models used in Geant4

The *quark–gluon string* (QGS) and *fritiof string* (FTF) models are theory based models that describe the hadron–hadron, hadron–nucleus and nucleus–nucleus interactions above ~ 15 GeV and ~ 5 GeV respectively [167]. The QGS model describes the formation of strings in the initial collisions of the protons, neutrons, pions and kaons with the nuclei by building a three–dimensional model of the target. According to the model, two or more strings could be stretched between the partons (quarks or gluons) within the hadrons. The model also covers splitting of the nucleons into quarks and di-quarks, the formation and excitation of quark–gluon strings and string hadronization. The FTF model, which is an alternative string model, was developed based on the Fritiof approach in order to overcome the validity gap between the cascade and string models around 10 GeV [168]. Although it is similar to the QGS model, it has a different set of string fragmentation functions. Unlike the QGS model, FTF can be used for all long–lived hadron projectiles including *lambda*, *sigma* and *omega*.

In addition to the string models, which are valid at high energies, Geant4 provides cascade models (*Bertini* and *Binary*) to complement the high energy models. The *Bertini cascade* (BERT) model is valid for proton, neutrons, pions, kaons, and hyperons with kinetic energies below 10 GeV. According to the model, secondaries produced in the collision of incident hadrons with protons and neutrons in the target nucleus are transported along straight lines through the nuclear medium. As an alternative to the BERT model, the *Binary cascade* (BIC) model is used for incident protons and neutrons with kinetic energies up to 10 GeV and for pions below ~ 1.5 GeV. The model is based on the series of two-particle collisions within the target nucleus, which is modeled by a three–dimensional collection of nucleons. Both incident particle and subsequent secondaries are transported along curved paths, which are calculated by numerically solving the equation of motion [169].

De-excitation of the remnant nucleus after the initial interaction is handled by the *precompound* (P) model, which is valid below 200 MeV for any excited nucleus. In the simulation of the showers induced by hadron interactions with matter, this model is responsible for the lower energy component of the shower [169].

In addition, Geant4 offers the *parameterized models*, which have been developed based on the GHEISHA hadronic package from Geant3. The Low and High Energy Parameterized models (LEP, HEP) depend on both data and theory, and they cover most of the particle types over a large energy range. Since they are mainly based on the calorimetric measurements from the 1980's, much certain up-to-date knowledge in hadronic physics is missing in the mentioned models [170]. Although they were available in the previous versions of the Geant4, they have become obsolete with the release of 10.0.

Since the Geant4 hadronic models are valid over a finite energy domain, it is customary to include several physics models in a physics list according to the needs. For example, the QGSP and FTFP models are combination of the Precompound model with the QGS and FTF models respectively. Therefore, QGSP and FTFP models handle de-excitation of the remnant nucleus thanks to the Precompound model they include. Furthermore, QGSP and FTFP models could also be combined with the BIC or BERT models to form various models like QGSP_BIC, QGSP_BERT and FTFP_BERT. Similarly the LHEP is based on the LEP and HEP models to cover all hadronic interactions for all particles in a wide energy region.

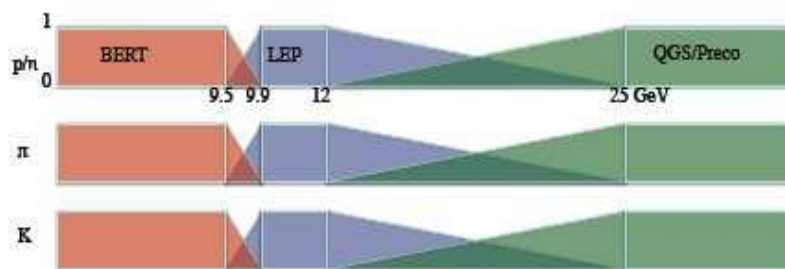


Figure 4.4. Energy intervals of QGSP_BERT for various particles [171]

If two combined models have validity over an overlapping energy region, a smooth transition mechanism is used for that region. Figure 4.4 provides an illustration of the QGSP_BERT physics list used for nucleons, pions and kaons. In addition to the QGSP and BERT models, the LEP model is also included in QGSP_BERT to describe the interactions at intermediate energies, which are not covered by either

QGSP or BERT. The transition between the BERT and LEP (LEP and QGSP) models is made at 9.5–9.9 GeV (12–25 GeV).

4.2.3.3. Cuts

It is obvious that calculation of the particle interactions at energies much lower than the energies the user is interested in is CPU time consuming. Therefore, it is important to determine a threshold (*cut*) value, below which the particle tracking will be stopped. This yields a balance between the accuracy of the results and the computing speed.

In Geant4, all particles are tracked down to zero kinetic energy unless they disappear by reasons like decay or interaction. However, the production cuts, which determine whether a particle to be created or not, are used instead of tracking cuts. Some electromagnetic processes like Bremsstrahlung and gamma ray production lead to huge number of small energy secondary gammas and electrons. Secondary particles with energies lower than the defined production threshold are not generated in the simulation. In addition to electron, positron and gamma, a cut could be applied to the proton as the production thresholds of nuclei for hadron elastic processes. If a track does not have enough energy to produce secondaries above the production threshold, its energy is integrated into the energy deposition of the parent track along its trajectory. This ensures that the particle energy deposition is taken into account correctly.

Cut value in Geant4 is specified as a distance which is converted into the energy for individual materials for each particle type. Although the default cut value is defined to be 1 mm for all of the abovementioned particles in any matter, the user can set new cut values for each particle separately. Setting a 1 mm cut allows one to track the particles until they no longer have enough energy to produce secondaries which travel at least 1 mm. Users should also keep in mind that one value of the cut corresponds to different production thresholds in energy depending on the material.

CHAPTER 5. SIMULATION

This chapter discusses the models constructed for the atmosphere and the crust of the Earth using Geant4, release 9.3.p01. The atmosphere model was utilized for the investigation of atmospheric muon distributions. The models for the Earth's crust were used in the simulations for the estimation of the underground muon distributions at various depths. In addition to the modeled geometries, distributions of the primary particles that injected upon the geometries have been introduced and physics models used in the simulations have been stated in this chapter.

5.1. Model of the Earth's Atmosphere

5.1.1. Earth's atmosphere

The Earth's atmosphere is a layer of gas mixture extending up to ~1000 km from the Earth's surface into space. However, more than 99% of the total atmospheric mass is within the first 30 km above the Earth's surface [172]. The atmosphere gets thinner with the increase in the altitude and slowly dissipates in outer space. Although there is no definite boundary between the atmosphere and the outer space, the *Karman line*, which is 100 km above the sea level, is generally accepted as being the boundary of the atmosphere and space [173]. As stated above, the atmosphere extends to greater heights than the Karman line, but the atmosphere is so thin above the altitude of 100 kilometers that the air density at such altitudes is less than that of the perfect artificial vacuums at the surface [172].

The common name given to the mixture of the gases that form the Earth's atmosphere is the *air*. The relative composition of the air varies somewhat from place to place on the surface of the Earth and even from time to time in the same

place. However, with the exception of the variable components like water vapor, dry air consists of 78.08% nitrogen (N_2), 20.95% oxygen (O_2), 0.93% argon (Ar), 0.039% carbon dioxide (CO_2) and small amounts of other gases including neon, helium and methane [172]. Although the relative fractions of the air's constituents are very stable up to an altitude of ~ 80 km [172], pressure, density and temperature of the air change depending on the height from the Earth's surface.

As a result of the gravitational attraction and compressibility of the gasses, density and pressure of the atmospheric gasses decrease with the increase in the altitude. As it is shown in Figure 5.1, which illustrates variation of the air pressure depending on the altitude, the pressure decreases gradually (sharply) at relatively small (greater) altitudes from the Earth's surface. More precisely, 50% of the mass of the atmosphere lies below an altitude of 5.6 km while the percentage reaches 90% at ~ 16 km.

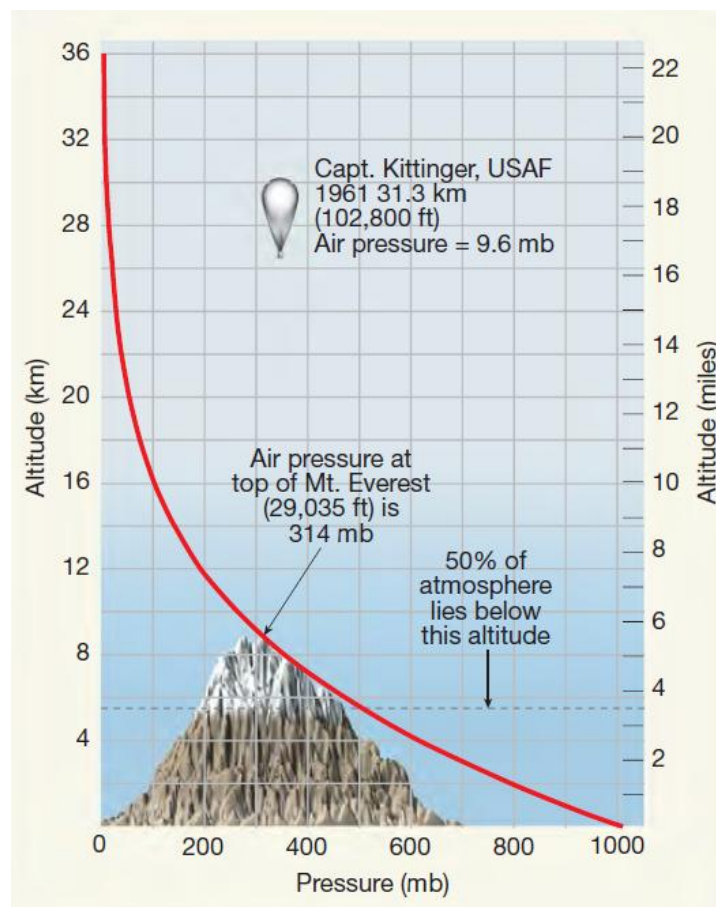


Figure 5.1. Change in the atmospheric pressure depending on the altitude [172]

In contrast to the density and the pressure, temperature of the air has a more complicated altitude dependence structure. Based on the temperature, the atmosphere is divided into different layers. Temperature profile of the atmosphere up to 140 km altitude is shown in Figure 5.1.

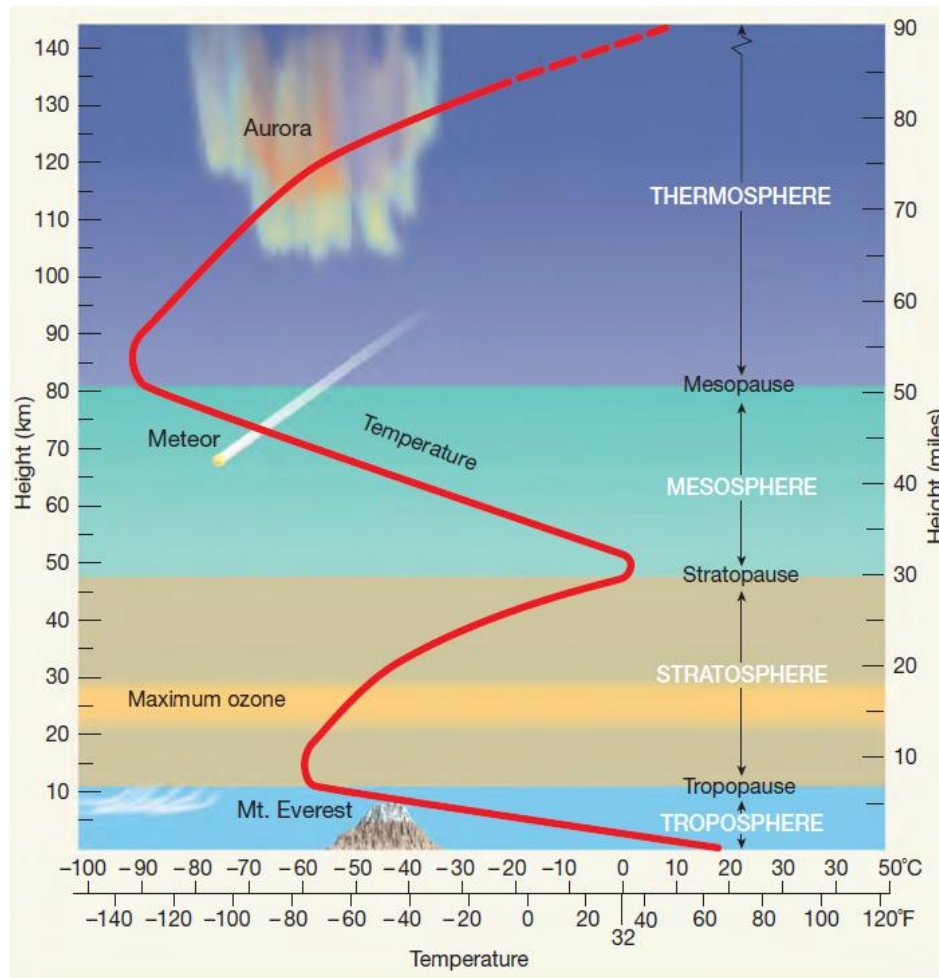


Figure 5.2. Thermal structure of the atmosphere up to 140 km altitude [172]

The layer from the ground up to ~12 km, in which the temperature decreases with an increase in the altitude, is called the *troposphere*. All the phenomena related with the weather like storms and clouds, occur within this layer. Above the troposphere lies a region known as the *tropopause*, which separates the troposphere from the stratosphere.

The layer from the tropopause to ~50 km is known as the *stratosphere*. Although the lower part of the stratosphere is almost an isothermal region, the temperature starts to increase with the altitude after ~20 km since the atmospheric *ozone* (O₃) is concentrated in this layer. Absorption of the ultraviolet radiation from the Sun causes the gases in this layer to be heated. Although the ozone concentration reaches the maximum between 15 and 30 km above the ground, the smaller amounts of ozone above that range absorb enough ultraviolet radiation to increase the temperature. As a result, air temperature at the *stratopause*, which is the boundary between the stratosphere and the mesosphere, is nearly 60 °C higher than the one at the tropopause.

The *mesosphere* is the third layer of Earth's atmosphere. It occupies the region from the stratopause to the height of 80–85 km. The air temperature again falls with the altitude up to the upper end of this layer, known as the *mesopause*. The fractions of the air constituents, except for water vapor and ozone, remain almost the same from the ground up to the mesopause. Therefore, the region below the mesopause is also called the *homosphere*.

Above the mesopause is the *thermosphere*, in which the temperature rises again with altitude. Although it has no well-defined upper limit, the thermosphere is accepted to extend between 500 and 1000 km. Temperature increase in this layer is due to absorption of highly energetic solar radiation by oxygen and nitrogen present in the atmosphere. High-energy solar radiations also ionize gas particles in the thermosphere, creating electrically charged ions of atoms and molecules. Therefore, the region of ionized gases is also called the *ionosphere*, where the auroras primarily occur.

5.1.2. Atmosphere model

In this study, the Earth's atmosphere has been modeled as a rectangular box with 100 km height. Such an assumption, which neglects the curvature of the Earth, is acceptable since the atmospheric muons with zenith angles greater than 70° are not studied in any part of the work. The modeled atmosphere has been divided into 100 layers, each having 1 km of thickness, to be able to interpret the altitude dependent structure of the atmospheric temperature, pressure and density. The bottom area of the model have been designed such large that the modeled volume of the atmosphere keeps all the muons with zenith angles smaller than 70° . A Geant4 representation of the modeled atmosphere is given in Figure 5.3.

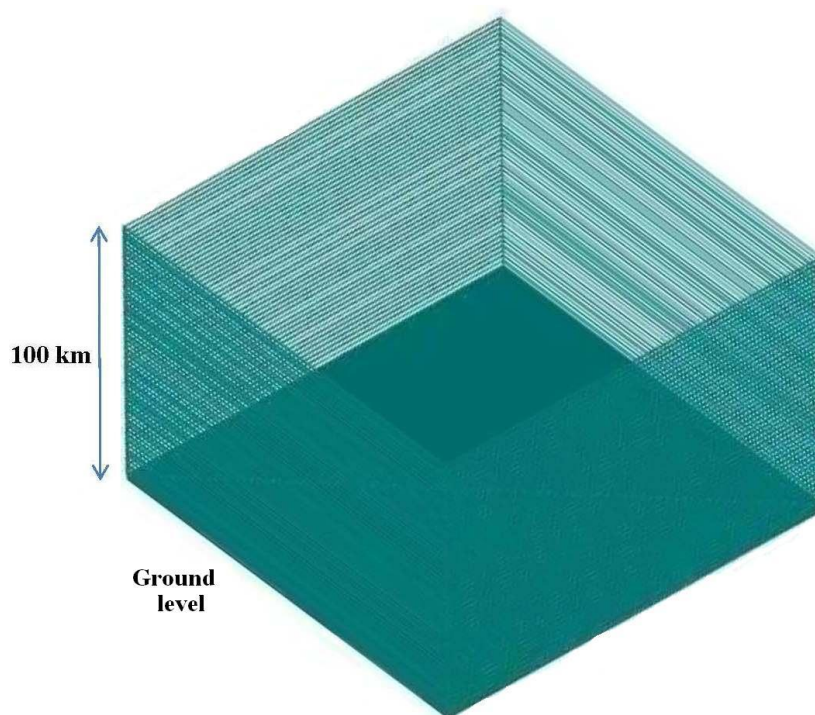


Figure 5.3. Geant4 view of the atmosphere model consisting of 100 layer, each having 1 km of thickness

The chemical composition of the atmosphere has been considered to be a mixture of 78.08% N_2 , 20.95% O_2 , 0.93% Ar and 0.04% CO_2 . The temperature (T), pressure (P) and density (ρ) of each layer have been determined based on the U.S. Standard Atmosphere model [174].

5.1.3. Electromagnetic fields

Some of the simulation results in this study have been compared with the experimental data obtained at various locations for testing the reliability of the models. In order to be able to compare the results, the Earth's magnetic field components for each site of interest have been calculated based on the International Geomagnetic Reference Field Model (IGRF 11) [175] and taking into account the measurements' date using a magnetic field calculator [176], and they have been included in the simulations. The calculated components of the geomagnetic fields, together with the geomagnetic cut-off rigidities, at the abovementioned experimental sites are given in Table 5.1.

Table 5.1. Calculated geomagnetic field components and cut-off rigidities at various experimental sites

Location	Geomagnetic cut-off rigidity (GV)	Components of the Geomagnetic Field (μT)		
		North	East	Vertical
Lynn Lake, Canada (56.5 °N, 101 °W)	0.4	10.2	1.7	59.4
Bucharest, Romania (44 °N, 26 °E)	5.6	23.0	1.6	41.7
Sakarya, Turkey (40 °N, 30 °E)	~6.0	25.2	2.1	39.7
Tsukuba, Japan (36.2 °N, 140.1 °E)	11.4	29.8	-3.7	35.5
Calcutta, India (12 °N, 88 °E)	~16.0	40.8	-1.1	4.5
Melbourne, Australia (47 °S, 144 °E)	~1.0	15.8	3.3	63.1

Charge distributions, resulting from the processes like ionization by cosmic rays and the radioactive decay at the ground, form an electric field in the atmosphere towards

the Earth's center. At fair weather, the electric field value near the Earth's surface is around 100 V/m where it falls below 5 V/m at altitudes above 10 km. Such a decrease in the electric field with increasing altitude results from the increasing atmospheric conductivity.

Muons are electrically charged particles. Therefore, the electric field, in principle, affects propagation of the muons through the atmosphere. Due to the charge distribution in the thunderclouds, the electric field during a thunderstorm is significantly higher than the one at fair weather. Hence, the effects of the atmospheric electric field on the muons become noticeable during a thunderstorm [177]. However, relatively low electric field at fair weather does not have a significant effect on the muons with energies above 0.1 GeV [178]. Therefore, the electric field was not taken into account in this study in order to speed up the simulations.

5.2. Models for the Earth's Crust

In the simulations, two different models, the standard rock and salt, have been used for representation of the Earth's crust.

5.2.1. Standard rock

The Earth's crust has been modeled as a rectangular box in the studies that investigate the underground muon distributions at various depths. The box, which has a height of 10000 m.w.e., was considered to be made of standard rock. In order to provide the standard rock properties, which were discussed in Section 3.5, the material of the modeled box was defined as a mixture of CaCO_3 and MgCO_3 with an average density of $\rho = 2.65 \text{ g cm}^{-3}$. Arranging the mass fractions of the elements as 52% O, 27% Ca, 12% C and 9% Mg yields $Z/A = 0.5$ and $Z^2/A = 5.5$ [179].

5.2.2. Slanic salt mine

A salt mine in Slanic–Prahova, Romania, is one of the underground sites that has been used for the muon measurements. The salt ore, consisting of NaCl (~98%) with impurities less than 2%, is ~500 m thick, a few kilometers long and wide [180]. The mine, which has both active (Cantacuzino) and inactive (Unirea) sites, is one of the sites around Europe that have been considered to house the detector components of the proposed project the Large Apparatus studying Grand Unification and Neutrino Astrophysics (LAGUNA) [181]. An artistic view of the mine, in which the relative positions of Cantacuzino, Unirea and proposed excavation for LAGUNA are shown, is given in Figure 5.4.

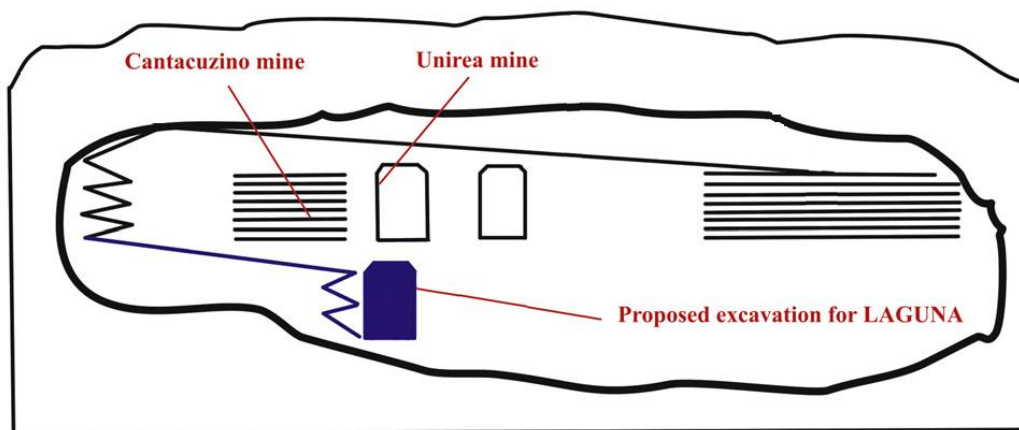


Figure 5.4. An artistic representation of the Slanic salt mine

The Cantacuzino mine is still active and has a relatively homogeneous salt structure. The Unirea mine, on the other hand, is not active anymore and it is currently open for touristic visits. It has corridors with stable salt walls shaped after extraction of salt over years. The heights of the walls and the widths of the corridors in the mine, whose floor is 208 m below the ground, are 52 – 57 m and 32 – 36 m, respectively. Given in Figure 5.5 is a schematic drawing of the Unirea mine. A laboratory constructed by the Horia Hulubei National Institute for Physics and Nuclear Engineering (IFIN-HH) of Romania for low background measurements in 2006 [182] is located in this mine. Location of the laboratory, together with that of the

elevator and cafeteria, is pointed out in the drawing. The gray regions in the drawing represent the salt walls where the white regions are the corridors.

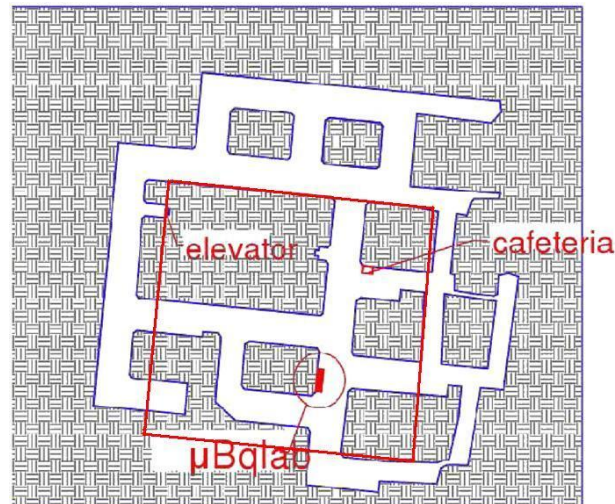


Figure 5.5. Schematic drawing of the Unirea mine

In this part of the simulations, the structure of the Unirea and Cantacuzino mines have been modeled to be made of pure NaCl, neglecting the impurities as an approximation. The Cantacuzino mine has been represented as a 210 m thick solid rectangular box having ignored the cavities in it. However, tens of meters wide and high corridors of Unirea have been taken into account during the model construction. For this purpose, Unirea salt mine was simulated to consist of two parts such that the top and bottom parts have the thicknesses of 150 m and 50 m, respectively. The upper part has been considered as a solid box while the corridors in the bottom one have been simulated according to the selected part (interior region of the red frame) of the schematic drawing given in Figure 5.5. Geant4 representation of the model is given in Figure 5.6, in which the IFIN-HH laboratory is indicated.

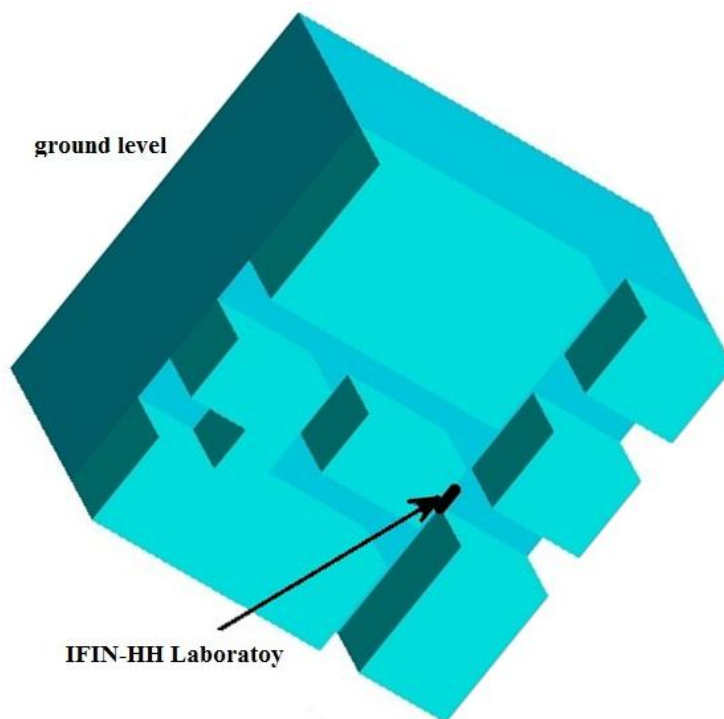


Figure 5.6. A Geant4 representation of a part of Unirea mine

5.3. Primary Particles

In the simulations of the atmospheric muons, proton has been used as the primary particle that was injected upon the modeled atmosphere. For the underground muon studies, both negative and positive muons have been used as primaries to be shot on the top of the modeled rock and salt samples. In each simulations primary particles have been isotropically distributed over the models within the zenith and azimuth angle intervals of $0 < \theta < 70^\circ$ and $0 < \varphi < 2\pi$, respectively. The zenith angle cut of $\theta < 70^\circ$, which is the requirement for the omission of the Earth's curvature, has been applied for protons since the atmosphere was modeled as a rectangular box. The reason for zenith angle cut, which can be different depending on the depth of the interest, for the primary muons is that the neutrino induced muons dominate and the usage of the cosine power law of angular distribution becomes inadequate at greater slant depths.

The energy distribution of the primary protons used in the simulations was adapted to the BESS measurement results obtained in 1998 at Lynn Lake below the energy of

120 GeV [183]. For the protons with higher energies, the distribution was extrapolated up to 10 TeV according to the power law with a spectral index of 2.7 (see the Equation 2.1) as shown in Figure 5.7.

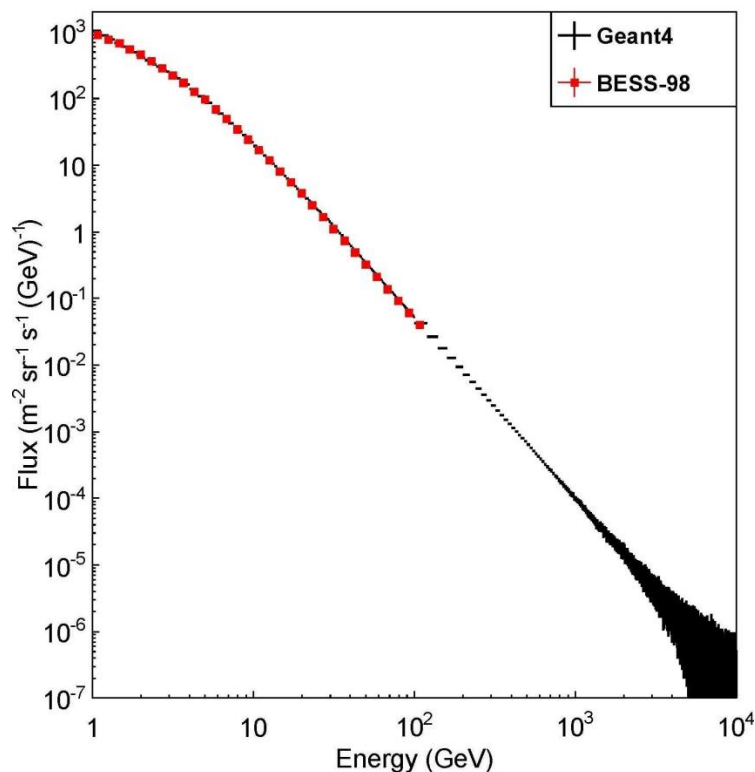


Figure 5.7. Energy spectra of the primary protons used in the simulation and the BESS measurement results [183]

It is known that the low energy part of the primary distribution depends on the geomagnetic cut-off rigidity (see Figure 2.20). The spectrum of the primaries given in the figure reflects the distribution of primaries at a low cut-off region with 0.4 GV. Therefore, distributions of the low energy primaries used in the simulations have been corrected according to the cut-off rigidities of each region given in Table 5.1.

The momentum distribution of the primary muons injected upon the rock and salt models has been resembled to the sea level measurements by Rastin [116] below 3 TeV/c. The distribution was extrapolated up to 20 TeV/c as shown in Figure 5.8 in order to study the muons with energies high enough to reach deep underground. Positively and negatively charged muons with momenta above 100 GeV/c have been

distributed by taking into account the muon charge ratio of ~ 1.3 . The threshold momentum of $100 \text{ GeV}/c$ is selected in order to increase the statistics by considering only the muons with enough energy that are able to reach the underground depth of interest.

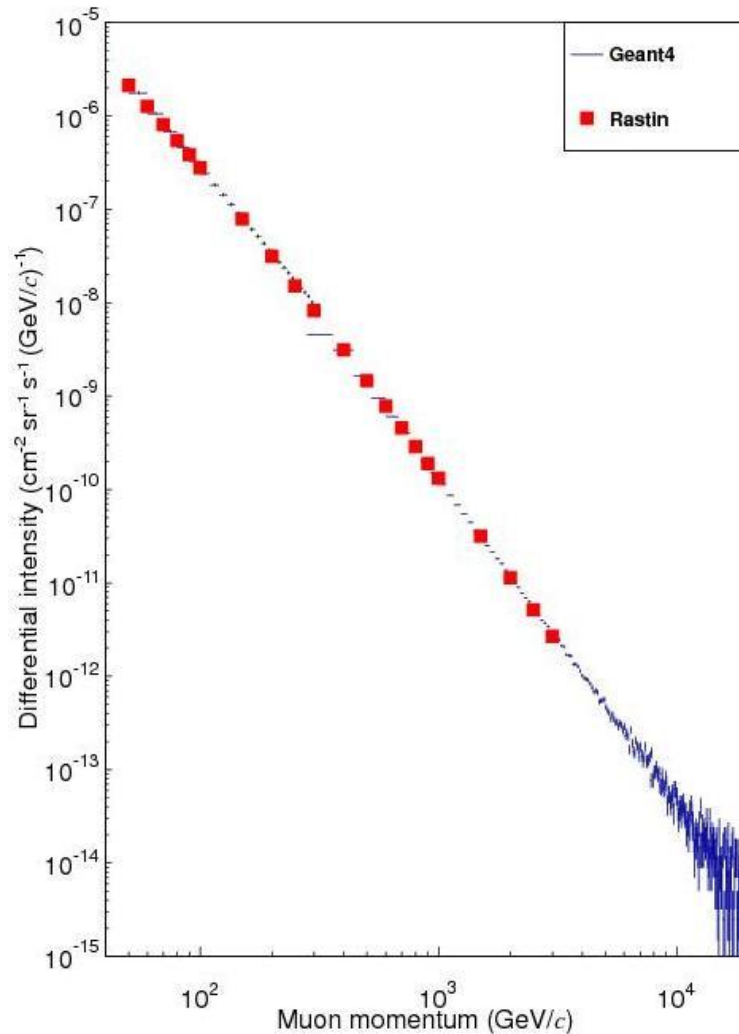


Figure 5.8. Ground level muon distributions; measurements by Rastin [116] and primaries used in the simulations

5.4. Physics Models

As it was previously discussed in Section 4.2.3, Geant4 offers a large variety of physics models handling the interactions of particles with matter in various energy ranges. In this study, *emstandard* model was used in order to handle the

electromagnetic interactions. For hadronic interactions, one of the three models, QGSP_BERT, FTFP_BERT and LHEP, has been utilized depending on several parameters, such as the type and the energy range of interest and the speed of the calculations.

Trajectories of the particles through the constructed model could be visualized in Geant4. This allows the user to test the simulation setup and debug the code. Cosmic ray shower induced by a primary proton injected upon the modeled atmosphere with the energy of 10 GeV is illustrated in Figure 5.9.

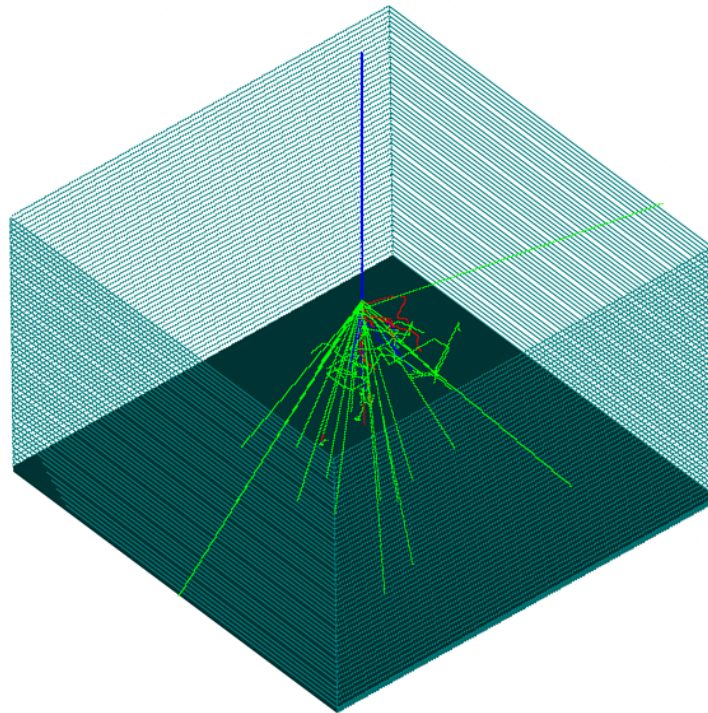


Figure 5.9. Visualization of the cosmic ray shower inside the modeled atmosphere

The blue (red) and green colored lines in the figure represent the positively (negatively) charged and the neutral particles' trajectories, respectively. For example, the vertical straight blue line represents the primary proton, the curved red lines are the trajectories of the negatively charged secondary particles like muon and the straight green lines are photons and neutrinos.

CHAPTER 6. RESULTS AND DISCUSSION

In this chapter, results of the simulations performed throughout this work are presented under three main categories. First, simulation results for the intensity, charge ratio and the angular dependence of the ground level muons are given. Then, variations of the abovementioned quantities with the increasing altitude are handled in another subsection. Finally, the muon distributions at various depths under the standard rock and salt samples are discussed separately.

6.1. Cosmic Muons at Ground Level

6.1.1. Muon spectrum and charge ratio

Vertical muon intensities at ground level have been investigated using Geant4 for two different geomagnetic locations, Lynn Lake and Tsukuba, with different cut-off rigidities, 0.4 GV and 11.4 GV, respectively. Given in Figure 6.1 is the simulated differential muon fluxes compared with the results of BESS 97-99 [119] and BESS-TeV 2002 [184] measurements made in abovementioned locations, respectively. Good agreement between the Geant4 simulation results and the experimental ones is seen for both regions, especially in high momentum regions. Muon events in the ranges of $\cos \theta \geq 0.90$ and $\cos \theta \geq 0.98$ were considered to contribute for the vertical flux for the BESS 97-99 and BESS-TeV 2002 measurements, respectively. This is because the East–West effect is not significant in regions with low cut-off, such as Lynn Lake, in contrast to the regions with high cut-off, like Tsukuba. Therefore, the abovementioned zenith angle cuts have also been applied in the simulations for Lynn Lake and Tsukuba.

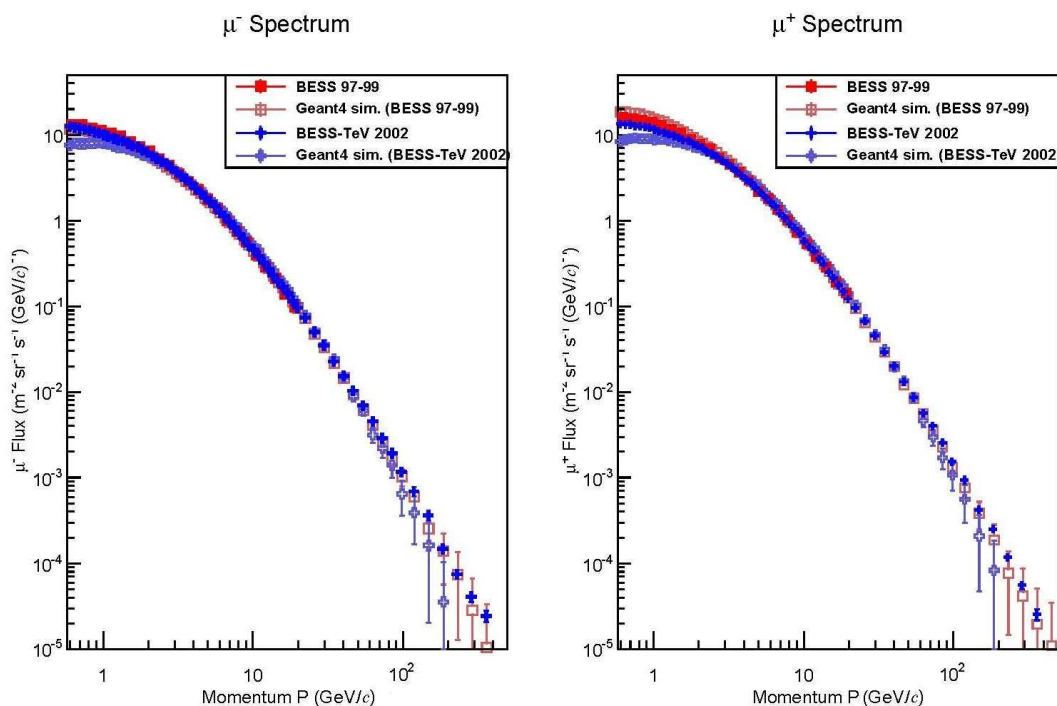


Figure 6.1. Geant4 simulation outputs for the vertical differential momentum spectra of muons in Lynn Lake and Tsukuba together with the experimental values [119, 184]

Simulation outputs have shown that the muon fluxes in Tsukuba and Lynn Lake are in good agreement with each other above ~ 4 GeV/c, and each distribution is also consistent with the corresponding BESS measurement. This finding agrees with the previous reported one that sea level muon distributions at momenta above 3.5 GeV/c are almost not affected by the geomagnetic cut-off rigidity [119]. The experimental data at lower momenta in Lynn Lake give slightly higher muon intensity than the data in Tsukuba due to the effects of the geomagnetic field. Although the Geant4 simulation outputs for Lynn Lake agree reasonably well with the experimental results, the ones for Tsukuba give slightly lower muon intensity than the experiment at low momentum region. The discrepancy of $\sim 20\%$ at lower momenta could be attributed to several reasons among which are the influences of the solar activity and of the atmospheric conditions.

Simulation output, together with the experimental data [184], for the muon charge ratio in Tsukuba is given in Figure 6.2 as a function of muon momentum. The simulated and the experimental momentum dependent muon charge ratios are clearly

seen to be good agreement with each other. The charge ratio increases with the increase in the muon momentum up to 10 GeV/c, and gets almost a constant value of ~ 1.3 at higher momenta.

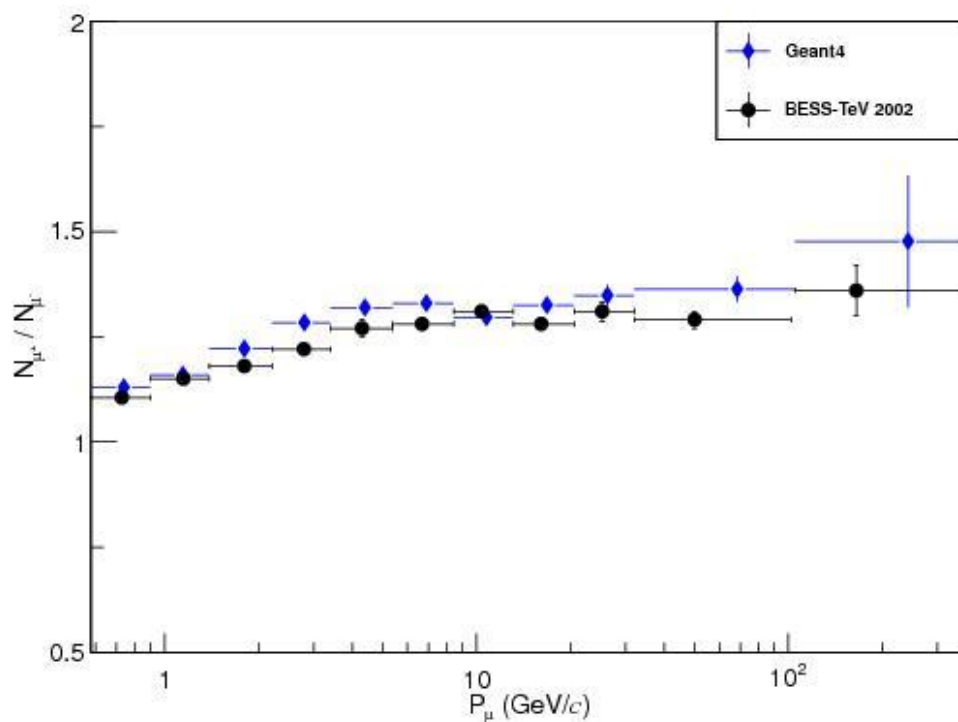


Figure 6.2. The simulated and experimental [184] muon charge ratios as a function of muon momentum in Tsukuba

6.1.2. Relation to the parent primaries

The consistence between the simulation and experimental results for the sea level muon distributions in Lynn Lake, discussed in previous section, consolidates the reliabilities of the atmosphere and physics models used in the simulation. Therefore, simulation data for the Lynn Lake have been utilized to estimate the angular and energy distributions for the parent primaries of the cosmic muons with different energies. Lynn Lake has been chosen because of its relatively low cut-off rigidity, which allows one to study the low energy primaries.

The relationship between the zenith angles of the primary protons (θ_p) and those of the sea level muons (θ_{μ}), produced by the interaction of such primaries, is illustrated

in Figure 6.3. On the left (right) panel of the figure, the relationship between the zenith angles of the muons with momenta, P_μ , above 1 GeV/c (10 GeV/c) and those of their parent primaries have been represented.

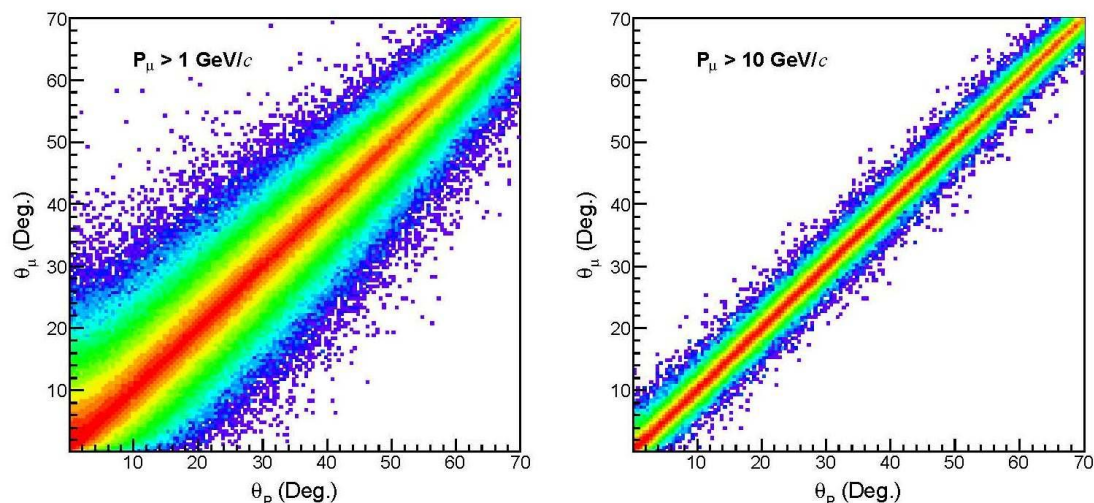


Figure 6.3. Interrelation between the zenith angles of the sea level muons and those of their parent primaries for threshold muon momenta 1 GeV/c (left) and 10 GeV/c (right) [185]

It can be seen from the figure that there is a direct proportion between the muons' and their parent protons' zenith angles. However, the relation for the muons with relatively small momentum threshold ($P_\mu > 1 \text{ GeV}/c$) has relatively large uncertainties as shown on the left panel of the figure. As the momentum increases, the uncertainty on the relation decreases, and a direct proportion between the angles could be seen more explicitly for the muons with the momenta above 10 GeV/c (see the right panel of the figure). As a result, the simulation results agree with the expectation that the secondary particles produced in the Earth's atmosphere travel almost in the same direction as their parent primaries [186].

The information on the interrelation between the energies of the cosmic muons at the ground or underground and those of the corresponding parent primaries could be acquired from the *response* or *coupling functions*. Such knowledge is important to study the variations in the intensities of primary radiations. The response function represents the parent nucleon energy distribution for muons with certain threshold energies, which correspond to specific underground depths, detected at sea level. The

response curves for sea level muons with threshold energies (E_μ) of 1 GeV, 14 GeV and 100 GeV obtained by using Geant4 are shown in Figure 6.4. The muon response calculated by Gaisser [187] for $E_\mu = 14$ GeV is also shown in the figure with the dashed line. It is seen that the result of the simulation for threshold energy of 14 GeV is quite compatible with that of the Gaisser's theoretical calculation at that energy threshold.

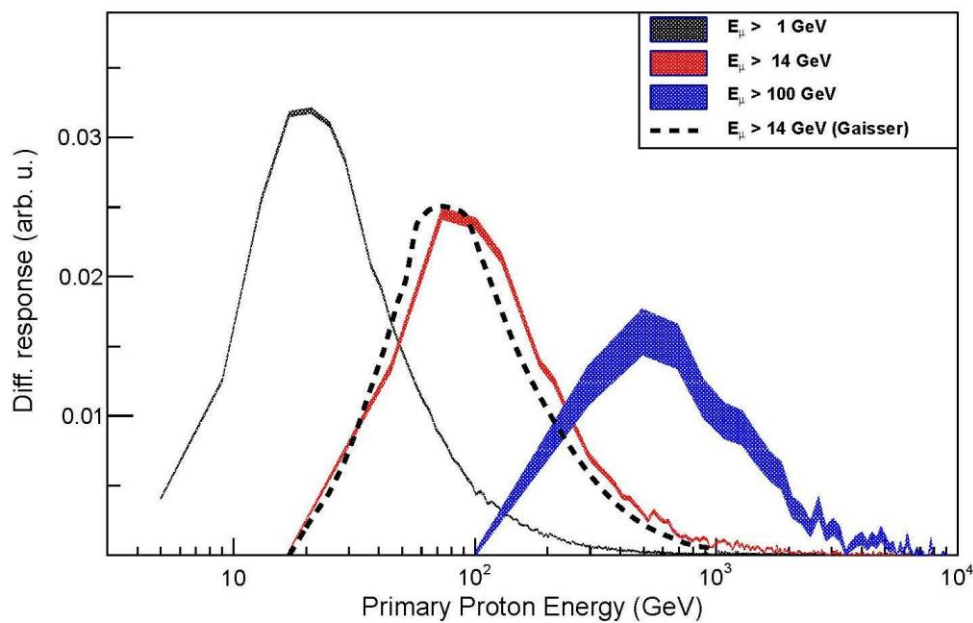


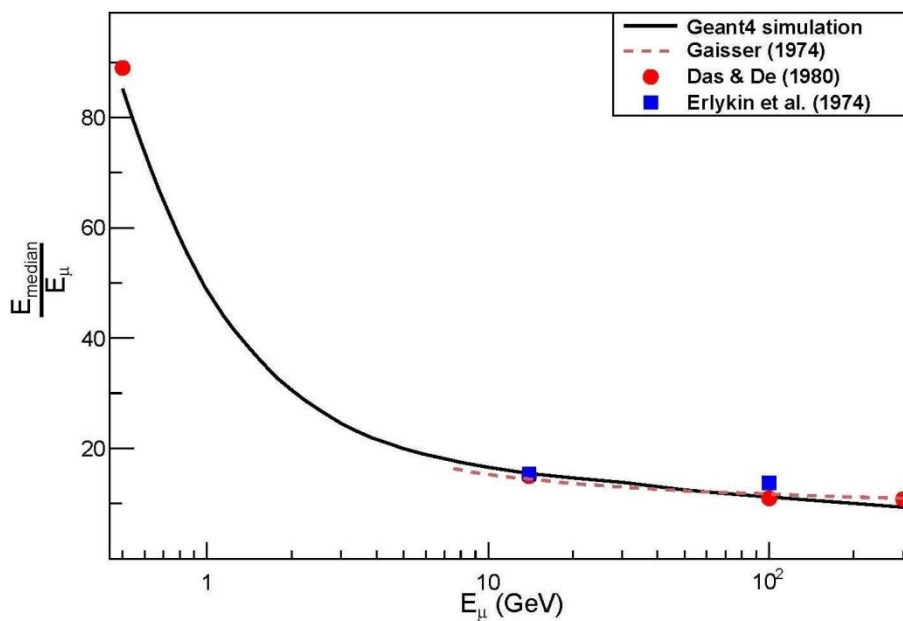
Figure 6.4. Response curves as a function of the primary proton energy for $E_\mu = 1$ GeV, 14 GeV and 100 GeV. The dashed line corresponds to Gaisser's theoretical calculation for $E_\mu = 14$ GeV [185]

The median energy (E_{median}) of response, which is an important quantity for the studies on the sidereal variation in muon flux [188], for the vertical muons with threshold energies in the range 0.5 – 300 GeV has also been investigated in this study. Muon events with zenith angles satisfying the condition of $0^\circ \leq \theta \leq 10^\circ$ in the simulation have been considered to have a vertical direction. E_{median} values of the primaries that are responsible for the vertical muons with different threshold energies, which correspond to specific underground depths, were previously calculated by several groups. The results of E_{median}/E_μ from the previous works and this study for $E_\mu = 14$ GeV and $E_\mu = 100$ GeV, corresponding to the underground depths of 125 m.w.e. and 400 m.w.e., respectively, are given in Table 6.1.

Table 6.1. Calculated and simulated $E_{\text{median}}/E_{\mu}$ ratios for two different muon threshold energies [185]

	E_{μ}	
	14 GeV	100 GeV
Gaisser [187]	~14	
Erlykin et al. [189]	15.4	13.8
Das and De [190]	15.0	11.0
Geant4	15.5	11.2

Result of the simulations for $E_{\text{median}}/E_{\mu}$ is illustrated in Figure 6.5 as a function of muon threshold energy for the range from 0.5 to 300 GeV. Also in the figure are shown the calculation results for several threshold energies from the studies cited in Table 6.1.

Figure 6.5. $E_{\text{median}}/E_{\mu}$ as a function of the threshold energy for the vertical muons [185]

Good agreement between the Geant4 simulation results from this study and those obtained from the previous works is seen in the figure. The results indicate that muons reaching the ground with energies around 0.5 GeV are produced by the interactions of parent primaries whose median energies are ~90 times greater than the threshold energy of the muons. The ratio ($E_{\text{median}}/E_{\mu}$) sharply decreases firstly with

the increasing muon energies up to ~ 5 GeV, at which its value is about 20. For the energies above 5 GeV, decrease in the ratio gets smoother such that it takes the value of ~ 10 at 300 GeV.

In addition to the vertical muons, the median energies of the parent primaries of the non-vertical muons have also been investigated for the energies in the range given above. $E_{\text{median}}/E_{\mu}$ for the muons with zenith angles in the intervals $40^{\circ} \leq \theta \leq 50^{\circ}$ and $60^{\circ} \leq \theta \leq 70^{\circ}$ are illustrated in Figure 6.6 together with the ones for vertical muons given in Figure 6.5.

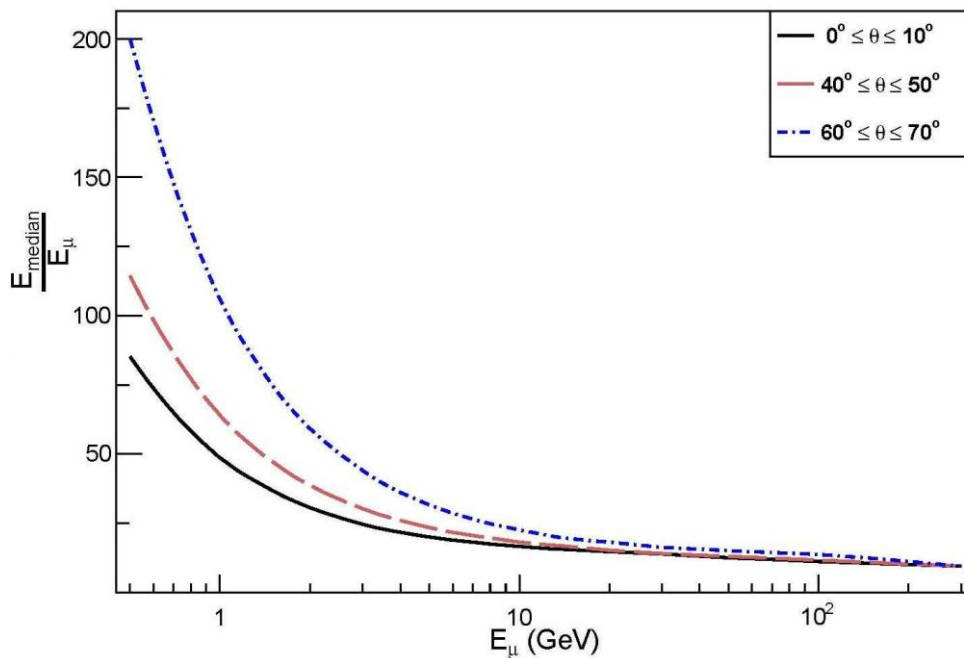


Figure 6.6. $E_{\text{median}}/E_{\mu}$ as a function of the threshold energies for the muons with different zenith angles [185]

It can be seen from the figure that the low energy muons with large zenith angles are produced by the interactions of the parent primaries with relatively higher energies, as opposed to the muons with narrower angles. For instance, the median energy values of the parent primaries of the muons with zenith angles $65 \pm 5^{\circ}$ are at least twice larger than those of the vertical muons for the muon energies below a few GeV. This means that among the muons reaching the ground with the same energies, the ones propagating with larger zenith angles have more energetic parents. This finding agrees with the basic information that cosmic muons with inclined

trajectories lose more energy than the vertical ones since the former interact more with the atmospheric gasses during their propagation towards the Earth's surface. However, median energies of the parent primaries that produce muons with different zenith angles converge to the same value for higher energies, especially above 100 GeV. The reason for the disappearance of the discrepancies shown in Figure 6.6 for higher muon energies is that amount of the energy loss in the atmosphere for the high energy muons is quite small compared to their energies. As a result, the energies of the parent primaries for the muons propagating with different zenith angles become almost independent of the zenith angle at muon energies above ~ 100 GeV.

6.1.3. Zenith angle dependence of the muon intensity

In this study, investigation of the zenith angle dependence of muon intensities at ground level of different geomagnetic locations has been made in two steps. Firstly, angular dependence of the integrated muon intensity has been obtained for Sakarya, Turkey after testing the reliability of the simulations with the measurements made using Berkeley Lab cosmic ray detector. Detailed information on the detector can be found in [191]. Then, the zenith angle dependence of differential muon intensities at the ground in the western, eastern, southern and northern azimuths have been investigated separately for Calcutta, India and Melbourne, Australia. Simulation results for these locations with significantly different geomagnetic cut-off rigidities have been compared with the experimental ones.

Using the Berkeley Lab cosmic ray detector, muon events have been measured for every 10° between the zenith angles 0° and 90° . The zenith angles of interest have been made eligible for the measurements by rotating the detector paddles. The rotation has been made in the northern direction in order to avoid the East–West effect. A slab of lead with a thickness of 2.2 cm was inserted between the paddles as an absorber during the measurements in order to minimize the contribution of the electromagnetic components, such as electrons and positrons. However, muons also lose energy while passing through the absorber. The total energy loss of the muons in the absorber and in the roof material (concrete) of the laboratory was estimated to be 200 MeV.

The measurements performed at each zenith angle have been simulated by taking into account the detector acceptance. Further details on the measurements and the detector acceptance are given in [192]. After distributing the primaries over the modeled atmosphere, muon events reaching the bottom, which is considered to be the ground level, with energies greater than 200 MeV have been recorded for each zenith angle. Results of the simulations normalized to those of the measurements are illustrated in Figure 6.7. Normalization has been made with respect to the counting rate at 0° . There is a very good agreement between the simulation and measurement results for $\theta < 70^\circ$ where the Earth's curvature can be neglected.

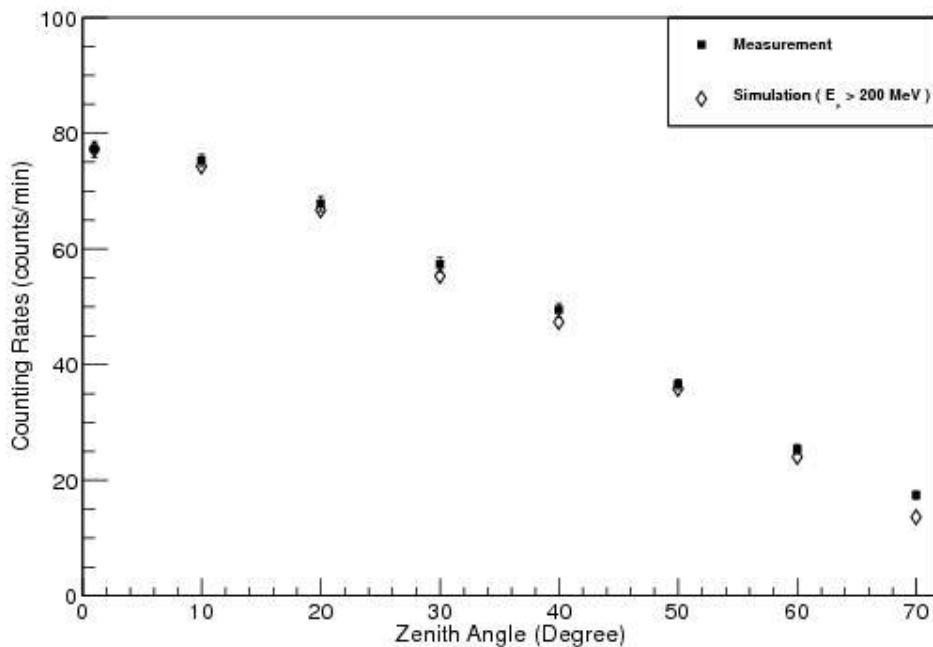


Figure 6.7. Muon counting rates measured using a Berkeley Lab cosmic ray detector and the normalized output from the Geant4 simulation [192]

The coincidence counts measured at each zenith angle are overlapped with the ones at neighboring angles due to the relatively large acceptance of the detector. Therefore, an exact determination of the counts at certain zenith angle using the abovementioned detector is impossible. There are several ways of decreasing the overlapping effect like increasing the separation of the scintillation plates [193] in order to decrease the detector acceptance. However, Geant4 simulations have been used in this study instead.

After acquiring the consistency of the simulation with the experiment, simulation study has been extended to investigate the zenith angle dependence of the muon events at ground level having the zenith angles from 0° up to 70° with 5° increment. Muon events with energies above 1 GeV are plotted as a function of zenith angle (Figure 6.8). In order to obtain the exponent n in the cosine power law (see Equation 3.8), the distribution plotted in the figure has been fit to the function $m\cos^n \theta$. The exponent for $E_\mu > 1$ GeV was found to have the value of $n = 1.95 \pm 0.08$, which is in good agreement with the value previously reported as $n = 1.85 \pm 0.11$ [194].

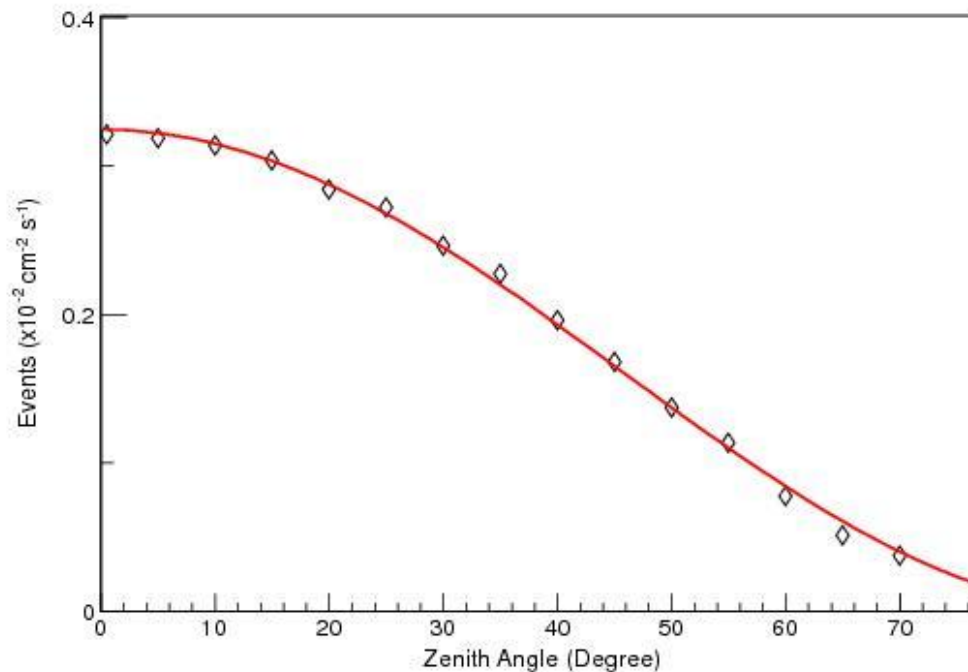


Figure 6.8. Geant4 simulation output for muon events as a function of the zenith angle [192]

In addition, the zenith angle dependence of differential muon intensity at ground level in the western, eastern, southern and northern azimuths have been investigated separately for Calcutta, India, and Melbourne, Australia, for muon momenta up to ~ 500 GeV/c. The exponent n was previously determined experimentally for different muon momenta and azimuth angles at these two locations, which significantly differ in geomagnetic cut-off rigidity. In the course of this work, Geant4 simulations have been performed for different azimuth angles and higher muon momenta in order to determine the azimuth angle and momentum dependent behavior of the exponent.

Muon counts obtained in the simulation for the western azimuth in Calcutta have been plotted in Figure 6.9 as a function of the zenith angle for different mean momenta from 1 GeV/c to 40 GeV/c. The left (right) panel in the figure illustrates the distributions of the muons having mean momenta between 1 GeV/c and 5 GeV/c (10 GeV/c and 40 GeV/c) with 1 GeV/c (10 GeV/c) increment.

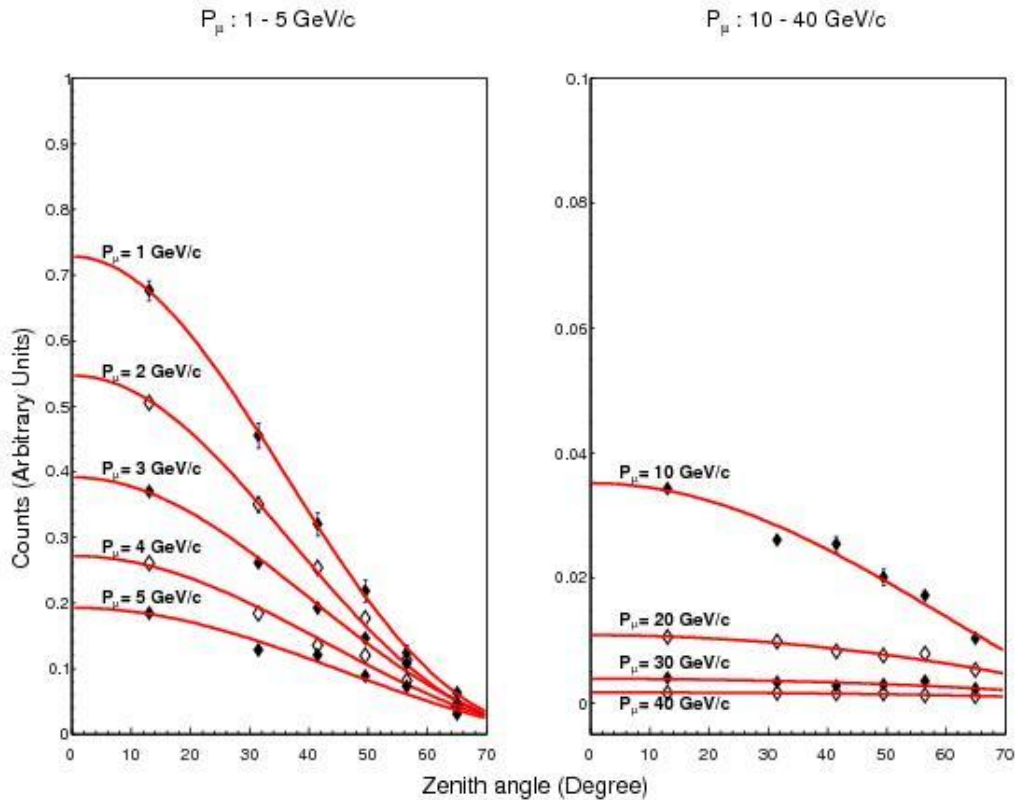


Figure 6.9. Simulation results for the muon counts as a function of the zenith angle for mean momenta 1–40 GeV/c in the western azimuth of Calcutta [195]

One can see from the figure that the spectra get flatter with the increase in the muon momentum such that counts become almost independent of the zenith angle for muon momenta at ~ 40 GeV/c. This indicates that the zenith angle dependence of the muon intensity decreases with the increase in the muon momentum as well. The red lines in the figure are the fit curves to the function $m \cos^n \theta$, which yields the exponent n for each mean momentum. The n values for the muons in the eastern, southern and northern azimuths have been obtained by applying the similar procedures. The simulated and available experimental values of the exponents for different azimuths in Calcutta are given in Table 6.2.

Table 6.2. Simulated and measured values of the exponent n for Calcutta in different azimuths [195]

Mom. interval (GeV/c)	Mean mom. (GeV/c)	Exponent (n)				
		Geant4 simulation				Meas.
		North	East	South	West	West
0.9–1.1	1	2.54±0.11	2.42±0.11	2.64±0.12	2.88±0.12	3.05±0.26
1.8–2.2	2	2.14±0.09	2.34±0.09	2.12±0.09	2.77±0.09	---
2.7–3.3	3	1.86±0.08	1.85±0.08	1.81±0.08	2.38±0.09	2.14±0.37
3.6–4.4	4	1.82±0.08	1.75±0.08	1.80±0.08	2.15±0.09	---
4.5–5.5	5	1.70±0.08	1.64±0.08	1.65±0.08	1.94±0.08	---
9.0–11.0	10	1.04±0.09	1.17±0.09	1.12±0.09	1.35±0.09	---
18.0–22.0	20	0.89±0.12	0.72±0.12	0.78±0.12	0.78±0.12	---
27.0–33.0	30	0.53±0.15	0.45±0.14	0.45±0.14	0.58±0.15	---
36.0–44.0	40	0.48±0.19	0.37±0.19	0.33±0.17	0.47±0.18	---

It is seen from the table that the exponent alters depending on the azimuthal direction. Namely, the exponent in the western azimuth is larger than the one in the eastern azimuth, especially for lower muon momenta. For the southern and northern azimuths, the exponent values are not much different from each other and they are in between the values of the ones in the eastern and western azimuths for most of the momentum bins. As the muon momentum increases, the difference among the exponent values diminish and they have similar values, within error, at higher muon momenta, independent of the azimuthal direction. The experimental values for the exponent obtained in Calcutta [196] for the western azimuth with the mean momenta of 1 GeV/c and 3 GeV/c have also been included in the table. The simulated and experimental exponents for this azimuth and the momentum bins given are, within the statistical uncertainty, consistent with each other. Since there are no measurements for the exponents in the other azimuths in Calcutta, comparison of the simulation results with the measurements is limited only by the western azimuth. The exponent values given in the table are plotted as a function of the muon momenta for

the western and eastern azimuths in Figure 6.10. The additional experimental point, which is not included in Table 6.2 since it has different binning, has also been inserted into the figure at 1.8 GeV/c.

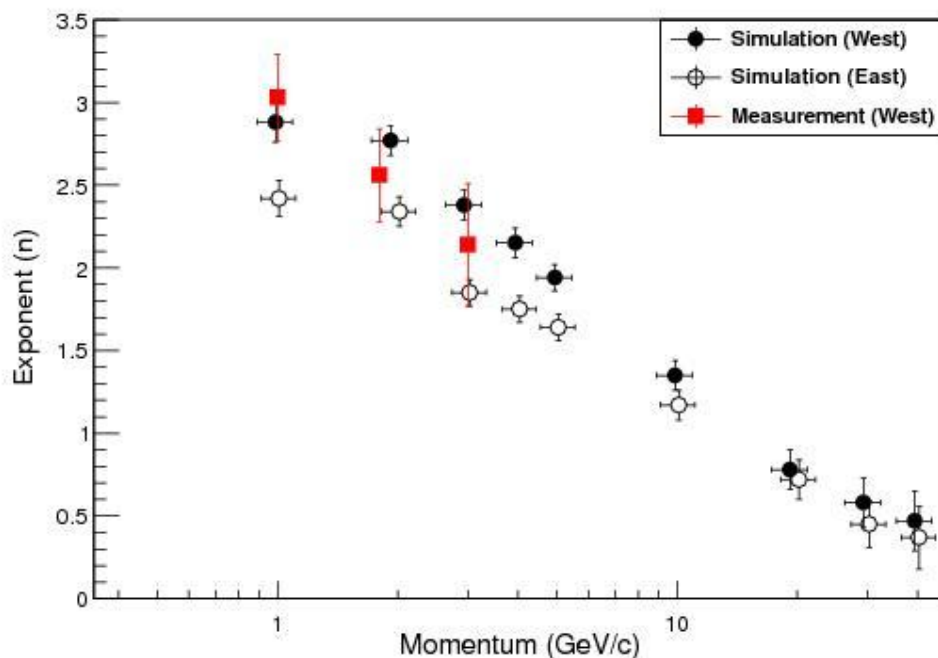


Figure 6.10. Simulated values of the exponent n for the western and eastern azimuths in Calcutta, together with the experimental ones for the West at the same location, as a function of the muon momentum [195]

It can be seen from the figure that the simulated n values, within error, are in good agreement with those from the experiment. The difference between the exponents belonging to the western and eastern azimuths at lower muon momenta diminishes with increasing momentum such that the exponent becomes independent of the azimuth angle for muons with momenta above 10 GeV/c. Based on this finding, no azimuth angle cut was applied during the investigation of the zenith angle dependence of higher energy muons. This provides a larger data set to be used without losing much information on the exponent. By fitting the integral intensity spectrum of the muons in the momentum interval 50–500 GeV/c with the function of $m \cos^n \theta$, the exponent has been found to be $n = 0.05 \pm 0.04$. This value of the exponent, which is very close to zero, indicates that the zenith angle dependence of cosmic muon intensity almost disappears for muon momenta above 50 GeV/c.

Therefore, it can be concluded from the simulation results that muons with momenta in the range from 50 GeV/c to 500 GeV/c reach the ground almost isotropically.

Similar procedure has been followed in order to investigate the zenith angle dependence of cosmic muon intensity in Melbourne, where the measurements were previously made both in the eastern and western azimuths [197]. Simulation results showing the zenith angle dependence of cosmic muon intensities for the western azimuth for different muon momenta are given in Figure 6.11 as an example.

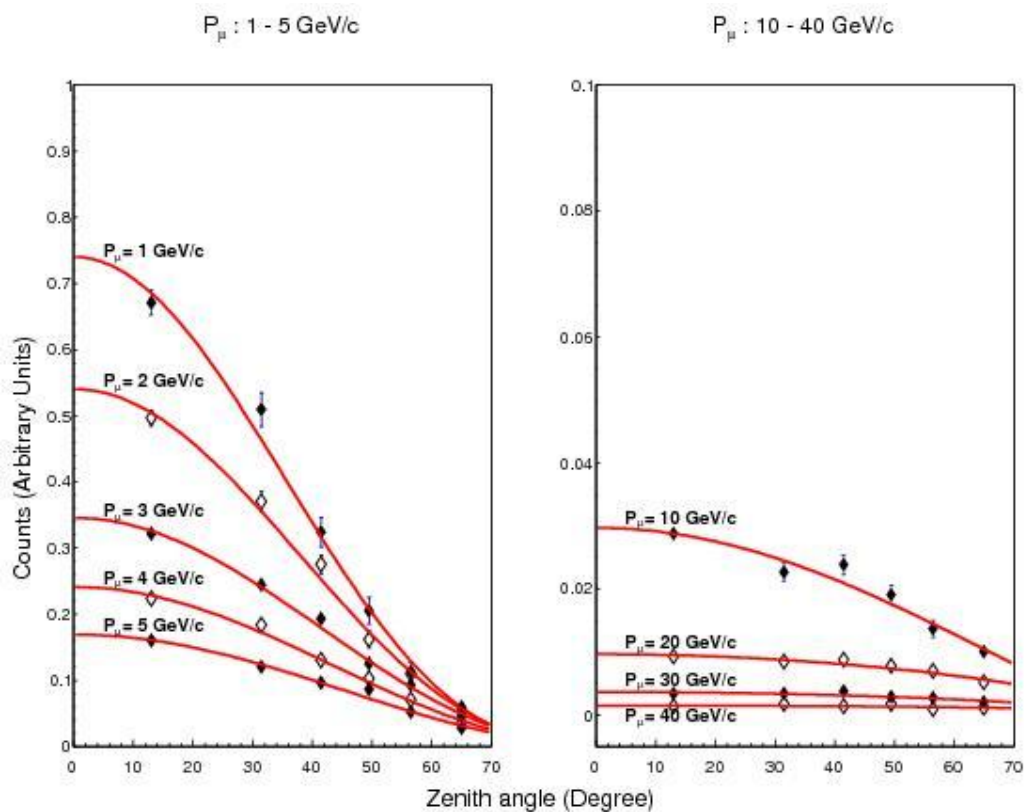


Figure 6.11. Simulation results for the muon counts as a function of zenith angle for mean momenta 1–40 GeV/c in the western azimuth of Melbourne [195]

As in Figure 6.9, on the left (right) panel of the figure are shown the muon counts as a function of the zenith angle for muons having a mean momentum between 1 GeV/c and 5 GeV/c (10 GeV/c and 40 GeV/c) with 1 GeV/c (10 GeV/c) increment. All the distributions, for western, eastern, southern and northern azimuths have been fit to the cosine power function. The exponent values from each fit for every momentum bin of interest and the available experimental ones for different azimuths in

Melbourne are given in Table 6.3. Momentum intervals are the same as those for Calcutta, given in Table 6.2.

Table 6.3. Simulated and measured values of the exponent n for Melbourne in different azimuths [195]

Mean mom. (GeV/c)	Exponent (n)					
	Geant4 simulation				Measurement	
	North	East	South	West	East	West
1	2.66±0.11	2.83±0.11	2.80±0.12	2.94±0.12	3.05	3.10
2	2.54±0.10	2.45±0.09	2.37±0.09	2.64±0.09	---	---
3	2.20±0.08	2.16±0.08	2.14±0.08	2.28±0.08	2.15	2.05
4	1.94±0.08	1.77±0.08	2.00±0.08	2.12±0.08	---	---
5	1.70±0.08	1.61±0.08	1.71±0.08	1.96±0.08	---	---
10	1.08±0.10	1.28±0.10	1.27±0.09	1.21±0.10	1.25	0.95
20	0.70±0.13	0.43±0.12	0.87±0.15	0.63±0.12	0.55	0.20
30	0.58±0.16	0.39±0.17	0.69±0.20	0.57±0.16	---	---
40	0.34±0.23	0.23±0.21	0.33±0.21	0.31±0.21	---	---

In contrast to their azimuth dependent behavior in Calcutta, the exponents are compatible with each other, for a particular muon momentum, at all azimuths in Melbourne. This is because the relatively low geomagnetic field component parallel to the Earth's surface affects the trajectories of the cosmic muons coming from the each azimuth almost equally. Therefore, the East–West effect is expected not to be as remarkable in Melbourne as the one in Calcutta. For this reason, the differences among the n values for each azimuth could be attributed to the statistical uncertainty in addition to the effect of the relatively low geomagnetic field component. The n values in the western and eastern azimuths are illustrated in Figure 6.12 as a function of the muon momentum.

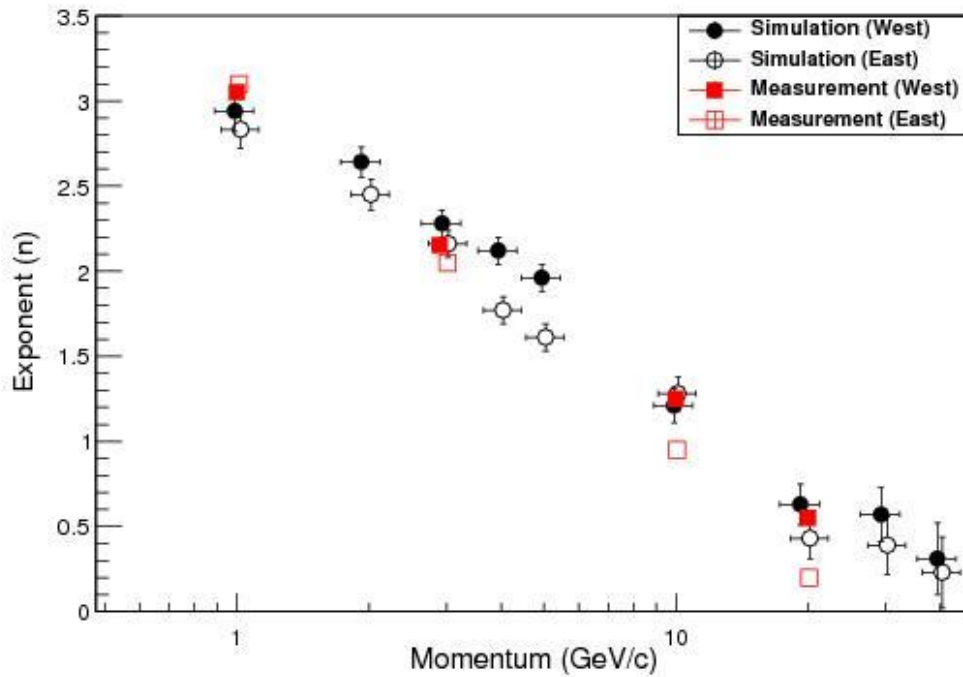


Figure 6.12. Simulated values of the exponent n for the western and eastern azimuths in Melbourne, together with the experimental ones for the same azimuths as a function of the muon momentum [195]

Although the errors on the experimental values shown in the figure were not given in [197], simulation results are in good agreement with them. As expected, the exponent gets smaller and approaches zero with the increase of muon momentum. Furthermore, the exponent values obtained for Melbourne are, within error, consistent with the ones for Calcutta for all the azimuths for cosmic muons with momenta above 10 GeV/c. Therefore, based on the simulation results it can be deduced that, in addition to the azimuth angle, the exponent is independent of the geomagnetic location for muons with momenta above 10 GeV/c. Moreover, for the muons reaching Melbourne with momenta above 50 GeV/c the exponent has been calculated to be $n = 0.08 \pm 0.04$, which is very consistent with the one in Calcutta for muons with the same momenta.

In conclusion, Geant4 simulation results illustrate that the zenith angle dependence almost disappears for the intensities of the muons with momenta between 50 GeV/c and 500 GeV/c. This finding suggests that cosmic muons with momenta above

50 GeV/ c and below 500 GeV/ c are approximately isotropic at the ground. Further studies with higher statistics are needed for investigation of the zenith angle dependence of muon flux at higher momenta.

6.1.4. Azimuth angle dependence of the muon charge ratio

Azimuthal angular dependence of the atmospheric muon charge ratio at Bucharest, Romania has been investigated in this study by Geant4 simulations. Bucharest was chosen as the location for the investigation since there already exist measurements [198] to be compared the results of the simulation. As discussed in Section 3.3.2, the muon charge ratio shows an azimuthal angular dependency, which is more distinctive at lower muon energies and larger zenith angles. Due to the effect of the geomagnetic field, the charge ratio gets larger (smaller) for the muons coming from the western (eastern) direction.

In this part of the study, muon events reaching the bottom of the modeled atmosphere with zenith angles in the interval of 30° and 40° and momenta below 1 GeV/ c have been taken into account. The charge ratio has been calculated for 12 different azimuth angles ranging from 0° to 330° with 30° increment and 5° uncertainty. Simulation results for the charge ratio of the ground level muons with a mean momentum of 0.5 GeV/ c have been illustrated in Figure 6.13 as a function of azimuth angle. Also in the figure are shown the measurement results obtained by different groups using different apparatuses, which are the WILLI detector in Bucharest [200, 201] and the OKAYAMA telescope at Okayama University, Japan [202].

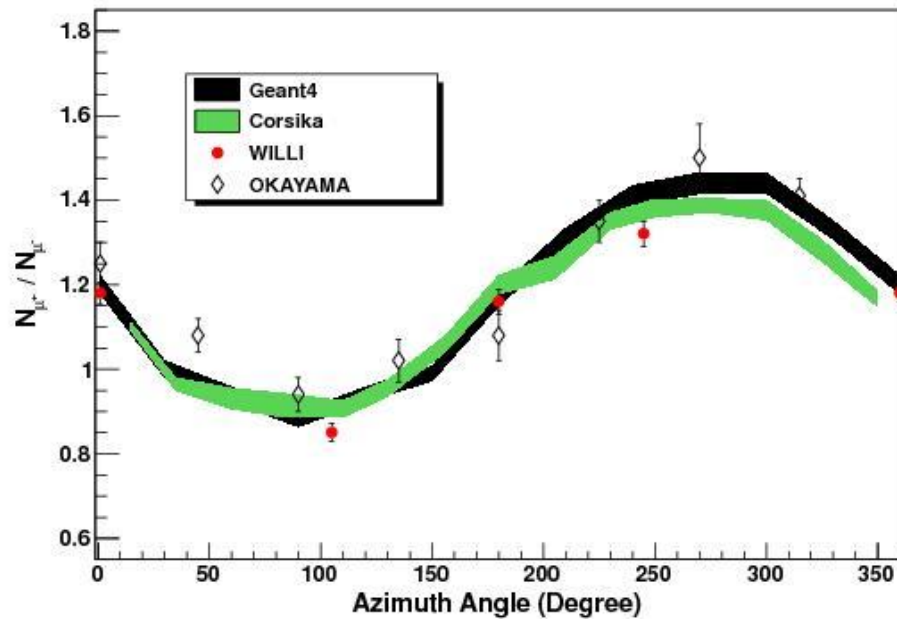


Figure 6.13. The simulated and experimental azimuth angle dependence of the charge ratio of low-energy cosmic muons reaching the ground with the mean momentum of 0.5 GeV/c [199]

It should be noted that the OKAYAMA measurements have been made in a region with a different geomagnetic cut-off rigidity and in a slightly higher momentum range (1.0 GeV/c–2.0 GeV/c). The WILLI group has also provided simulation outputs from CORSIKA, which is a program for detailed simulation of extensive air showers initiated by high energy cosmic ray particles [203]. One can see from the figure that Geant4 simulations have yielded quite compatible results with both the experiments and CORSIKA simulation.

Geant4 simulations have yielded the muon charge ratio of ~ 1.2 for the azimuth angles $\varphi = 0^\circ (= 360^\circ)$ and $\varphi = 180^\circ$, which correspond to the southern and northern azimuths, respectively. Namely, the charge ratio is the same for the muons reaching the ground from the North and South. This is because, the geomagnetic field, whose parallel component to the surface extends almost in the North-South direction, bends the trajectories of both positively and negatively charged muons coming from either North or South with almost the same amount. The muon charge ratios obtained for such directions are equal to each other and to the one from the vertical. However, the situation is different for the muons arriving to the ground from the East and West.

While the muon charge ratio has been found to have a minimum value of ~ 0.9 in the eastern azimuth ($\varphi = 180^\circ$), it increases as the direction gets closer to the West and reaches ~ 1.4 for $\varphi = 270^\circ$. The difference between the charge ratios of low energy muons decreases with the increase in the momentum as it is shown in Figure 6.14.

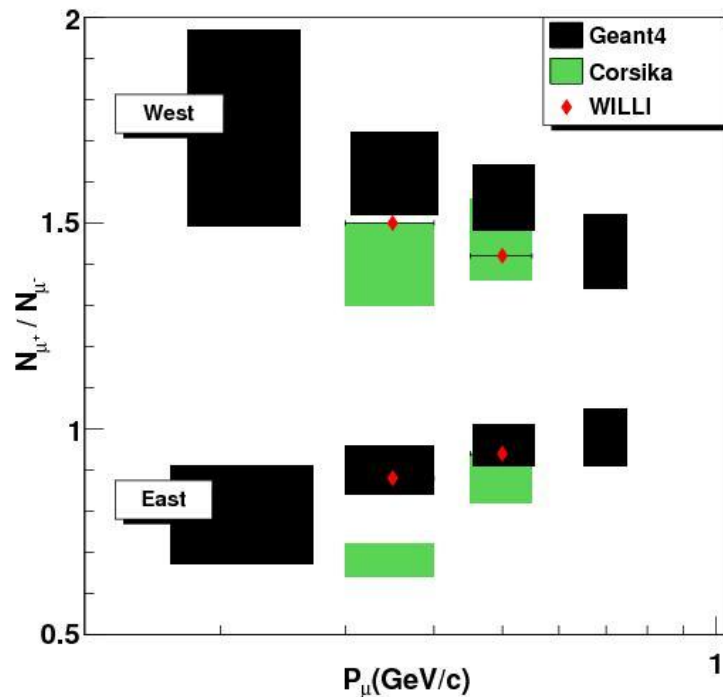


Figure 6.14. Muon charge ratio in the western and eastern directions below 1 GeV/c as a function of the muon momentum [199]

It can be seen from the figure that the muon charge ratios from this work reasonably agree with those from WILLI and CORSIKA. Although the WILLI group has provided the ratios for the muon momenta 0.35 GeV/c and 0.50 GeV/c, calculations in this study have been extended such that they cover two more momentum bins (0.22 GeV/c and 0.70 GeV/c) in order to see the behavior of the muon charge ratio from the western and eastern azimuths more clearly. As it is expected, the charge ratio from the western (eastern) azimuth decreases (increases) with increasing momentum within the momentum range of interest in such a way that it converges to the value for the vertical muons.

The East–West asymmetry of the muon charge ratio has also been calculated in this study using the equation

$$A_{EW} = \frac{(R_W - R_E)}{(R_W + R_E)}, \quad (6.1)$$

where R_W and R_E are the charge ratios from the western and eastern directions, respectively. Momentum dependence of the East–West asymmetry for muons with momenta below 1 GeV/c is illustrated in Figure 6.15.

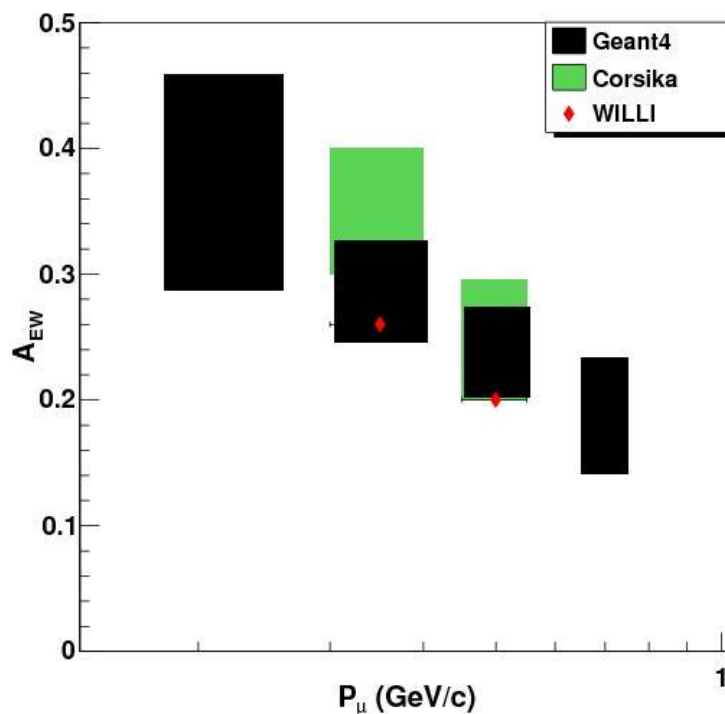


Figure 6.15. The East–West asymmetry of the muon charge ratio below 1 GeV/c as a function of the muon momentum [199]

The asymmetry decreases from ~0.37 to ~0.19 as the momentum increases from 0.22 to 0.70 GeV/c. The reason for the decrease in the asymmetry with the increase in muon momenta is that the effect of the geomagnetic field becomes less pronounced for higher muon momenta (or energies).

6.2. Cosmic Muons in the Atmosphere

It has been shown in Section 6.1.1 that the simulation yields consistent results for the sea level muon distribution in Tsukuba with the BESS measurements (see Figure 6.1 and 6.2). After having a consistency between the simulation and the experimental results, muon properties (spectra, charge ratios and zenith angular dependencies) at various atmospheric depths (100 g cm^{-2} , 200 g cm^{-2} , 270 g cm^{-2} , 550 g cm^{-2} , 710 g cm^{-2} and 920 g cm^{-2}) have been obtained using Geant4. Since, to our knowledge, there are no experiments performed at various altitudes in Tsukuba, simulation results cannot be compared with measurements.

6.2.1. Flux variations with the altitude

Momentum spectra of both negative and positive muons have been investigated in this study for the depth ranges mentioned above. Simulation results are plotted in Figure 6.16 such that each spectrum has been multiplied by the numbers given in the figure in order to view each spectrum without any intersection.

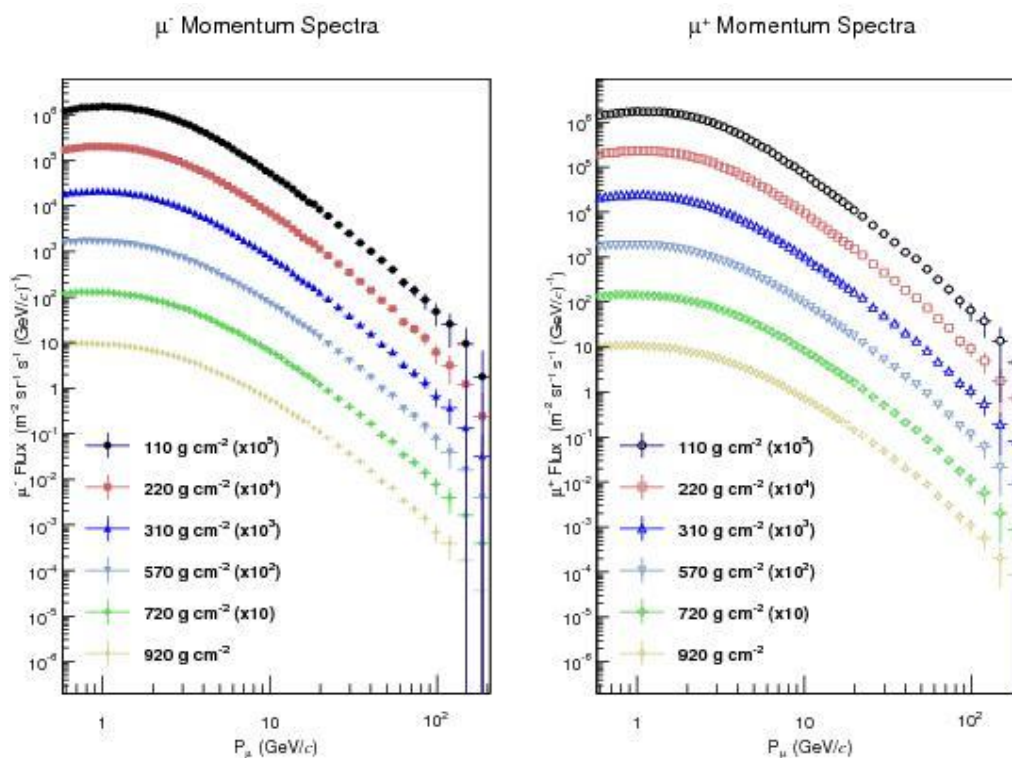


Figure 6.16. Momentum spectra of the atmospheric muons at various atmospheric depths

It is seen that the muon spectra are parallel to each other above a few GeV/c. This is consistent with the knowledge that the muon spectrum above 2 GeV/c follows the power law with an altitude independent spectral index [204]. However, the shape of the spectra changes in the lower momentum range depending on the atmospheric depth.

In addition to the spectral variations, change in the integrated muon intensities has been studied for the atmospheric depths of interest. The fluxes of negative and positive muons travelling in vertical directions with momenta above 0.58 GeV/c are illustrated in Figure 6.17 as a function of the atmospheric depth.

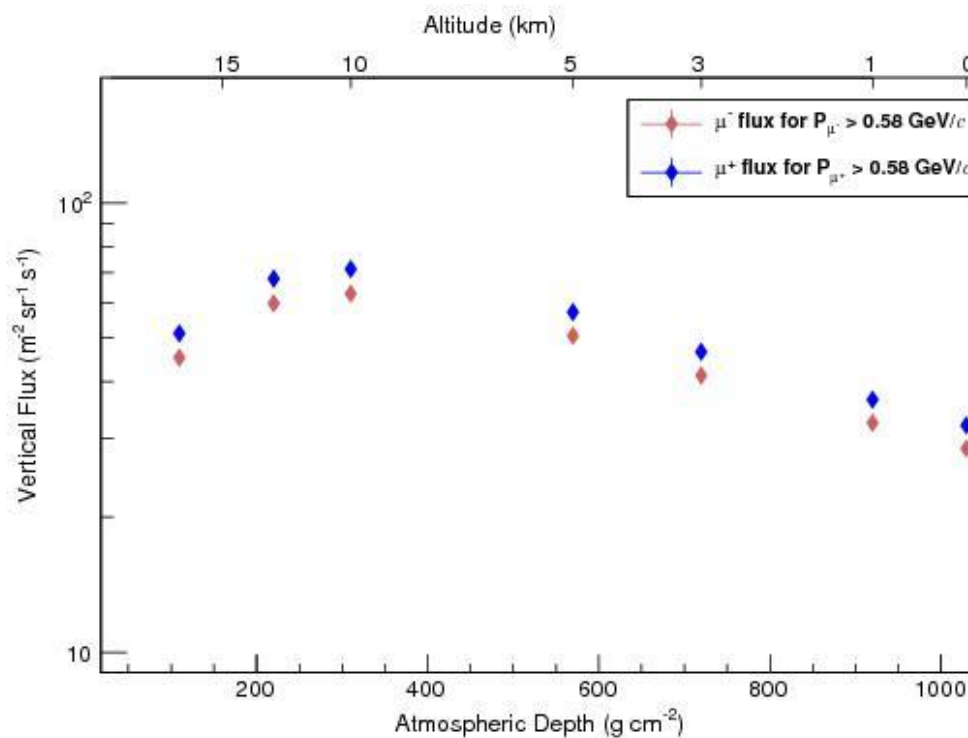


Figure 6.17. Fluxes of vertical muons above 0.58 GeV/c as a function of the atmospheric depth

The figure illustrates that the fluxes increase as the atmospheric depth decreases (or the altitude increases) and reach the maximum around 200 – 250 g cm⁻². Then the fluxes have a tendency to decrease for greater altitudes. This altitude dependent behavior of the flux investigated in this study is consistent with the measurement results given in Figure 2.14 although the measurements have been made in regions with lower cut-off.

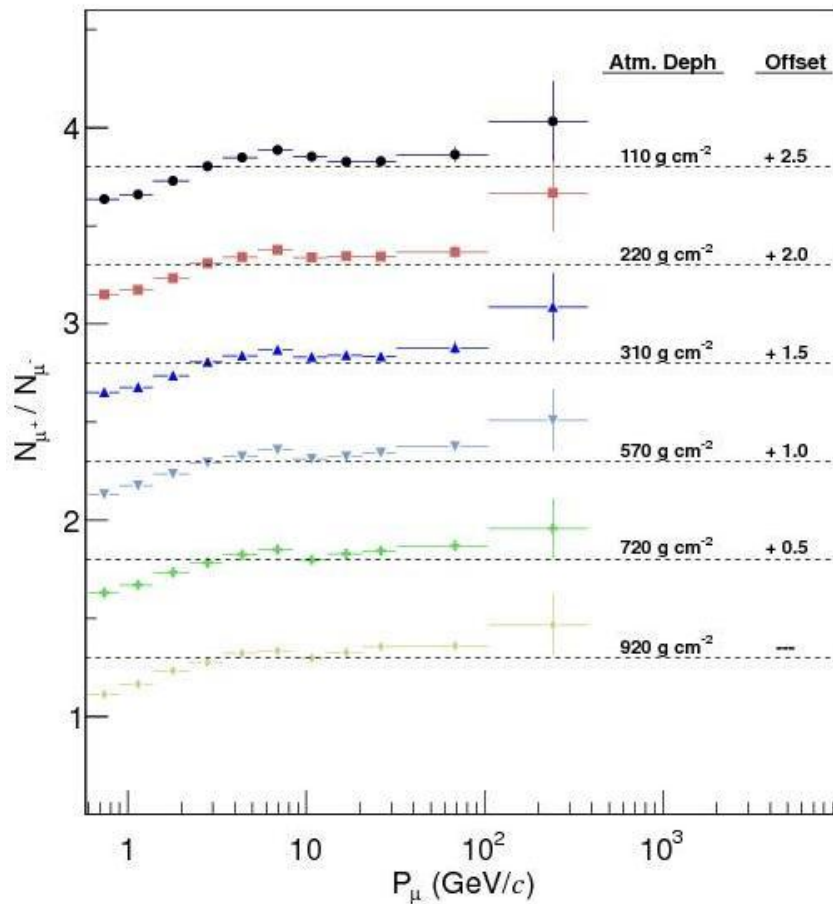


Figure 6.18. Muon charge ratios at various atmospheric depths as a function of the muon momentum

Muon charge ratios at each depth of interest have also been obtained as a function of the muon momentum (see Figure 6.18). It is seen that the momentum dependent behavior of the charge ratio is almost the same for all the altitudes up to 110 g cm^{-2} . Charge ratios for two different momentum intervals ($0.58 - 1.0 \text{ GeV}/c$ and $1.0 - 400 \text{ GeV}/c$) are illustrated in Figure 6.19 as a function of atmospheric depth.

Charge ratios for muons with momenta between $1 \text{ GeV}/c$ and $400 \text{ GeV}/c$ seem to be almost independent of the atmospheric depth. For muons with lower momenta, in the range of $0.58 - 1.0 \text{ GeV}/c$, the charge ratio slightly changes with the atmospheric depth. However, the changes are not significant to determine the depth dependent behavior of the charge ratio. Therefore, no clear correlation of the muon charge ratio with the atmospheric depth has been noticed in this study just as the observations in previous experiments [133–137].

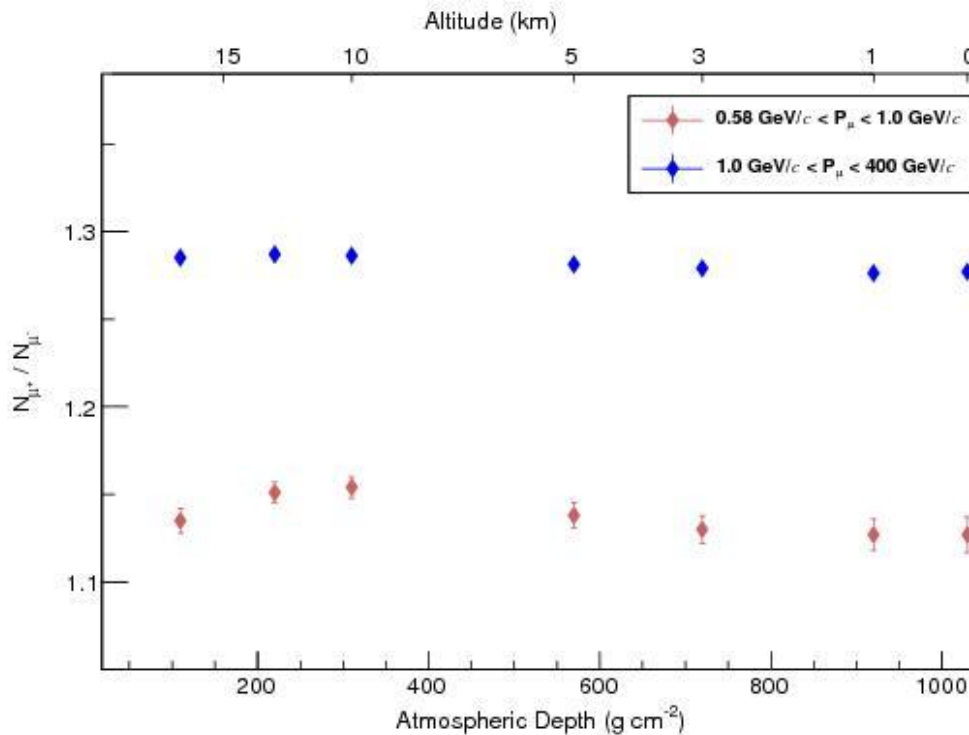


Figure 6.19. Muon charge ratios for two momentum intervals as a function of atmospheric depth

6.2.2. Zenith angle dependences in the atmosphere

Zenith angle dependence of the integrated muon intensities at the abovementioned atmospheric depths have been investigated for muon momenta above 0.58 GeV/c, 1.0 GeV/c, 5.0 GeV/c, 10.0 GeV/c, and 50.0 GeV/c separately. For this purpose, the integral intensities have been plotted as a function of the zenith angle up to 70°. In order to avoid influences of the East–West effect on the zenith angular dependence, muon events arriving at the level of interest from the northern and southern directions, within the azimuth angle $(\varphi - 20^\circ) < \varphi < (\varphi + 20^\circ)$, have only been taken into account. Each one of the distributions has been fit to the function of $m \cos^n \theta$ in order to determine the exponent n . Eventually, a set of n values for the integral intensities of the muons with different momenta at various atmospheric depths have been obtained. The n values are illustrated in Figure 6.20 as a function of the atmospheric depth for muon momenta above 0.58 GeV/c, 1.0 GeV/c, 5.0 GeV/c, 10.0 GeV/c and 50.0 GeV/c. The lines connecting the markers have been used to lead the eye.

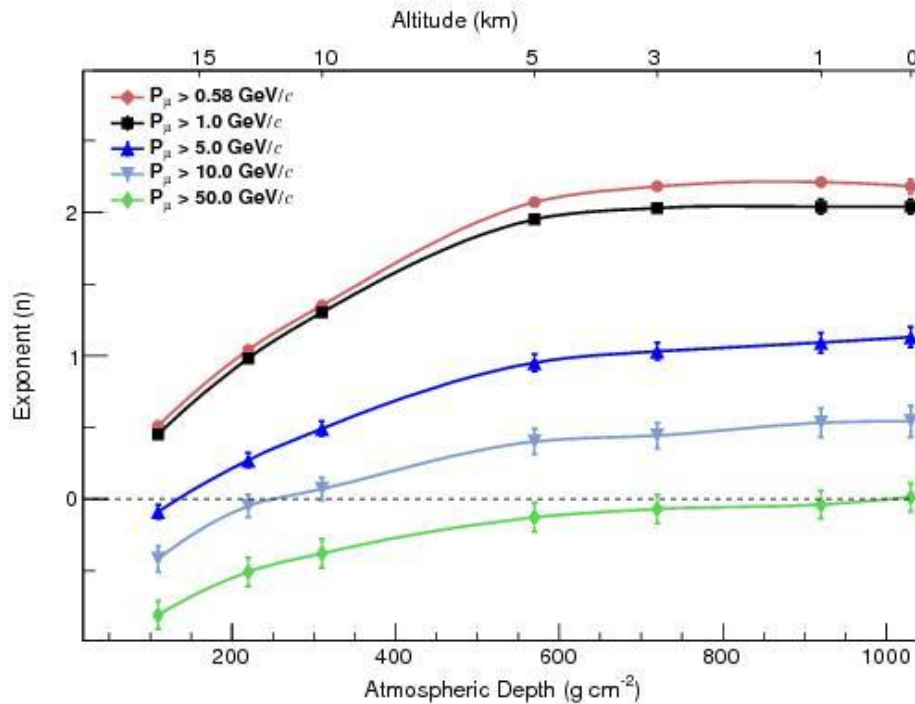


Figure 6.20. The exponent n as a function of the atmospheric depth for different muon momenta

The exponent for the muons reaching the ground level in Tsukuba with momenta above $1 \text{ GeV}/c$ has been found to be 2.03 ± 0.05 . This value is in very good agreement with the value of 1.95 ± 0.08 , which has been calculated for Sakarya (see Section 6.1.3). Moreover, the exponent seems to be nearly zero for the ground level muons with momenta above $50 \text{ GeV}/c$ as it has been previously discussed in Section 6.1.3. The previously discussed decrease trend of the exponent with increasing muon momenta for a certain atmospheric depth can also be noticed from the figure. For each of the muon momentum thresholds of the interest, the exponent has a tendency to decrease as the altitude increases below the depth of 600 g cm^{-2} , above which its change is very slow. This is because difference between the energy losses of the muons propagating in vertical and inclined directions diminishes with the increase in the altitude. As the atmospheric depth reduces significantly, intensities of the muons with inclined directions converge to that of the vertical ones, which yields a smaller exponent. Furthermore, several negative exponent values are seen in the figure, especially for greater altitudes and muon momenta. Based on the simulation results, one can conclude that the angular distribution of the muons with momenta above $50 \text{ GeV}/c$ obeys to $\sec \theta$ distribution as the altitude increases.

6.3. Underground Muons

6.3.1. Muon intensities in a salt mine

In this part of the study, muon fluxes at various depths in the salt mine of Slanic, Romania have been simulated using the Geant4 simulation package, and the results have been compared with the measurements made over there. As the first step, the threshold momenta (P_{th}) of the muons capable of reaching the particular depths have been determined. Knowledge of the threshold energy is important since taking into account only the muons with enough energy to penetrate the interested depths helps the user to obtain higher statistics. For this purpose, the vertical primary muons have been injected upon the salt model and the initial momenta of the muons reaching the depths of 154 m (the ceilings of Unirea), 188 m (Level 8 of Cantacuzino) and 300 m (top of the proposed excavation for LAGUNA) have been recorded. The results are illustrated in Figure 6.21 together with the primary muon distribution at ground level.

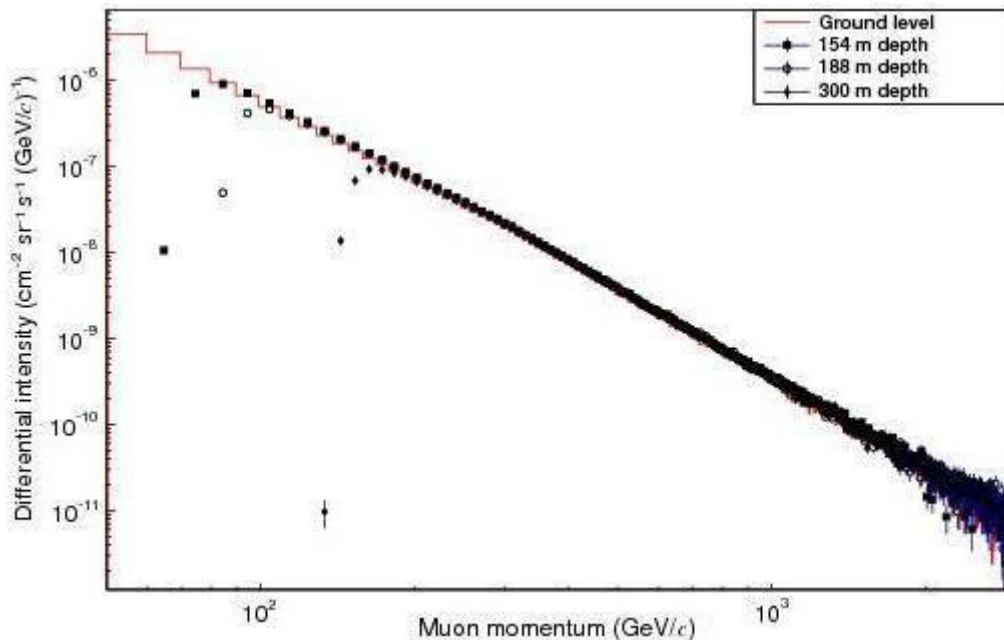


Figure 6.21. Ground level momentum distributions of the muons reaching various depths in salt [205]

P_{th} for Unirea, Cantacuzino (Level 8) and LAGUNA site have been found to be 65 GeV/c, 85 GeV/c and 145 GeV/c, respectively. As it is expected, peaks of the

distributions given in the figure shift towards higher muon momenta with increasing depth. Having figured out the P_{th} for each depth of interest, muons with momenta greater than P_{th} have been isotropically distributed over the salt mine models with a zenith angle cut of $\theta < 70^\circ$.

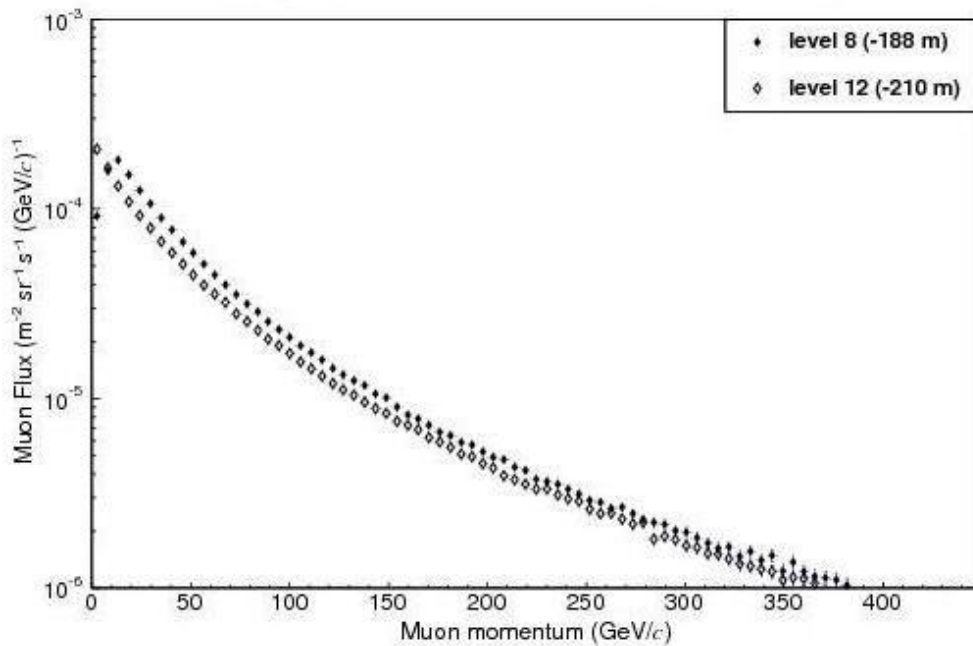


Figure 6.22. Flux of nearly vertical muons at two different levels of the Cantacuzino mine [206]

Geant4 simulation results for the differential flux of the vertical muons ($\theta < 10^\circ$) at different levels of the Cantacuzino mine have been illustrated in Figure 6.22. The spectra given in the figure are consistent with the ones [207] previously obtained using the MUSIC simulation code [208]. There is a peak appearing at 15 GeV/c in the spectrum of the muons reaching Level 8 of the Cantacuzino mine although the distribution at Level 12 of the same mine, which has a depth of 210 m, does not show a peak. This slight shape difference between the spectra at relatively low momentum region is considered to be due to the difference between the depths (22 m) of the levels. Moreover, muon fluxes at these depths get closer to each other with the increasing momenta such that the difference almost disappears for momenta especially above ~ 350 GeV/c.

Vertical ($\theta < 10^\circ$) muon spectrum in the Unirea salt mine is shown in Figure 6.23. It is seen that the distribution is similar to that of the Cantacuzino mine (Level 8) except for the peak position at ~ 30 GeV/c. The similarity between these distributions could be attributed to their similar depths in m.w.e. The depths of the Unirea and Level 8 of the Cantacuzino mine are reported in [207] to be 610 ± 11 m.w.e. and 601 ± 21 m.w.e., respectively.

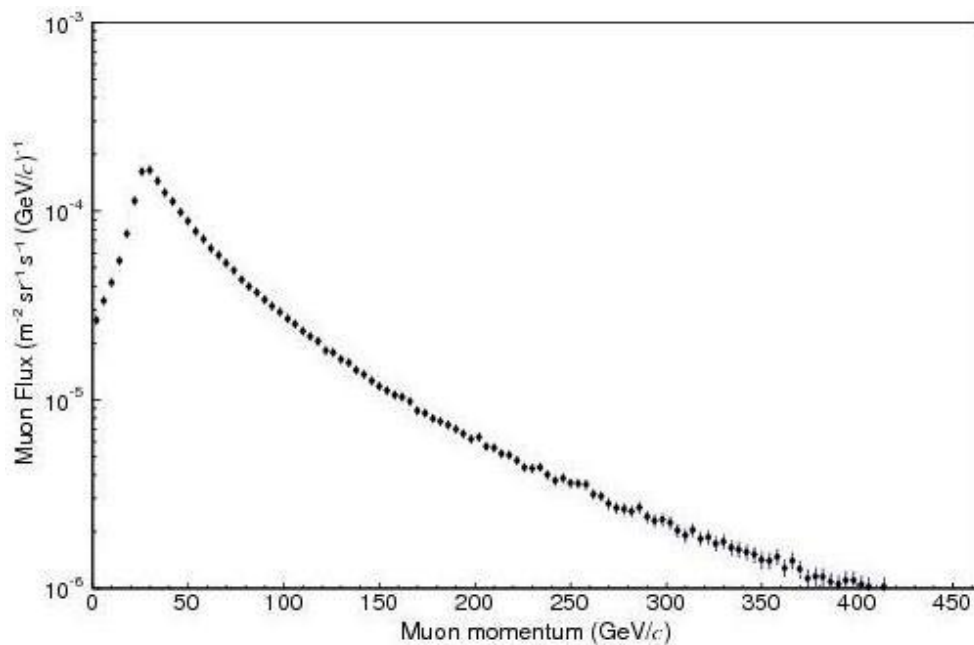


Figure 6.23. Flux of nearly vertical muons at the Unirea mine [206]

To be able to compare the results of the simulations with those from the measurements [207] performed at the two levels of the Cantacuzino mine and at the Unirea mine for muons with $\theta \leq 60^\circ$, fluxes of the muons arriving at the bottom of the each salt mine model within the same zenith angle range have also been calculated. Simulated and measured fluxes at the mentioned sites are given in Table 6.4.

Table 6.4. Simulated and measured fluxes at the Unirea mine and at the two levels of the Cantacuzino mine [206]

Location (mine)	Muon flux ($\text{m}^{-2} \text{s}^{-1}$)	
	Measurement	Simulation
Unirea	0.18 ± 0.01	0.14 ± 0.02
Cantacuzino – Level 8	0.19 ± 0.02	0.15 ± 0.02
Cantacuzino – Level 12	0.09 ± 0.01	0.10 ± 0.02

It is seen from the table that the simulation results, within the statistical error, are in good agreement with the measurements especially for Level 12 of the Cantacuzino mine. The discrepancy between the results of the simulation and those from the measurements made inside Unirea could mainly be attributed to the approximation excluding the additional gaps above the mines. In addition, ignoring the overburden, which is mainly composed of soil, over the salt in the simulations could also be considered to be among the possible reasons for the discrepancies even though its effect is expected to be small.

6.3.2. Zenith angle dependence of muon intensities in a salt mine

In this subsection, the simulated zenith angle dependence of the muon intensities in the Unirea and Cantacuzino (Level 8) mines, as well as in the proposed excavation for LAGUNA, are presented. For this purpose, muon intensities at each depth in the mine have been plotted as a function of the zenith angle, and each of the distributions has been fit with the function $m \cos^n \theta$ in order to determine the exponent n for each situation. The values for Unirea, Cantacuzino and the proposed excavation of LAGUNA have been found to be $n_U = 2.86 \pm 0.09$, $n_C = 2.53 \pm 0.10$ and $n_L = 2.65 \pm 0.16$, respectively (see Figure 6.24).

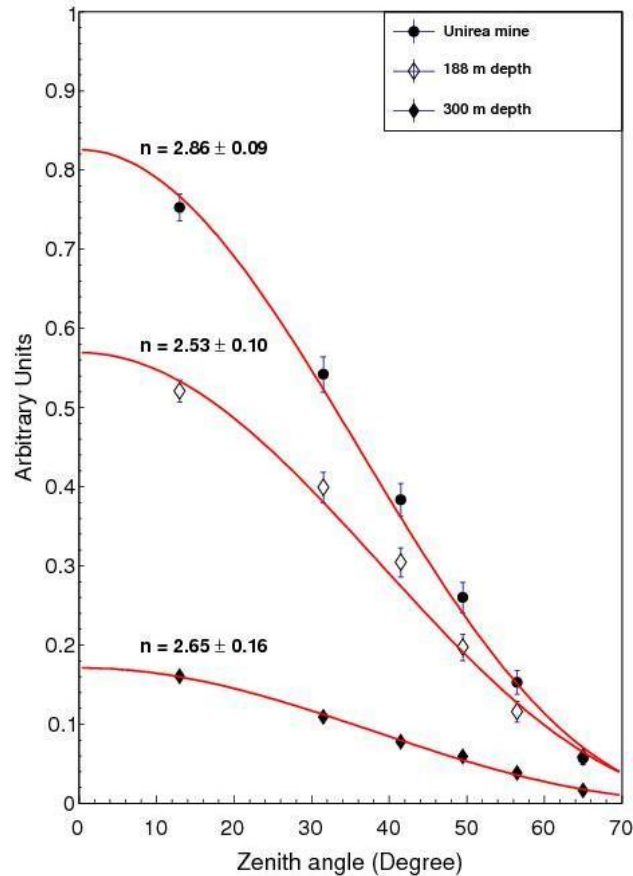


Figure 6.24. Muon intensities for each site of the Slanic salt mine as a function of the zenith angle [206]

One can see that the exponent n_L is larger than n_C . This finding is consistent with the expectation that the exponent increases with the increase in depth. Moreover, n_U has been found to be larger than both n_C and n_L . However, the Unirea mine has a shallower depth than the LAGUNA site. Therefore, n_L is expected to be larger than n_U , but it is not the case in simulation results. The reason for that contradiction is that the large corridors in Unirea allow the muons with narrower angles to reach the basement of the mine without losing much energy. Namely, the fraction of the cavities on the way of the muons travelling from the ground to the detector in Unirea mine with low zenith angles is significantly large due to the large dimensions of the corridors. On the other hand, the cavity fraction is smaller for the muons with large zenith angles in comparison with the paths of the muons in the salt. Because of this fact and the similar depths of the Cantacuzino and Unirea mines, difference between the muon intensities in both mines decreases with the increase in the zenith angle such that the large angle muon intensities converge to the same value.

6.3.3. Muon intensities at various depths in standard rock

Both differential and integral intensities of underground muons reaching several depths have been calculated up to 10000 m.w.e. and they have been compared with the measurements performed by different groups. The upper limit of 10000 m.w.e. was selected for the depth since for the deeper sites the neutrino-induced muons start to contribute to the muon intensity dominantly.

The simulated normalized local spectrum, which has been obtained by dividing the differential energy spectrum to the corresponding integrated intensity, of underground muons are illustrated in Figure 6.25 for various depths in standard rock. Behavior of the normalized local spectrum for each depth underground is consistent with the one in the literature (see Figure 3.17).

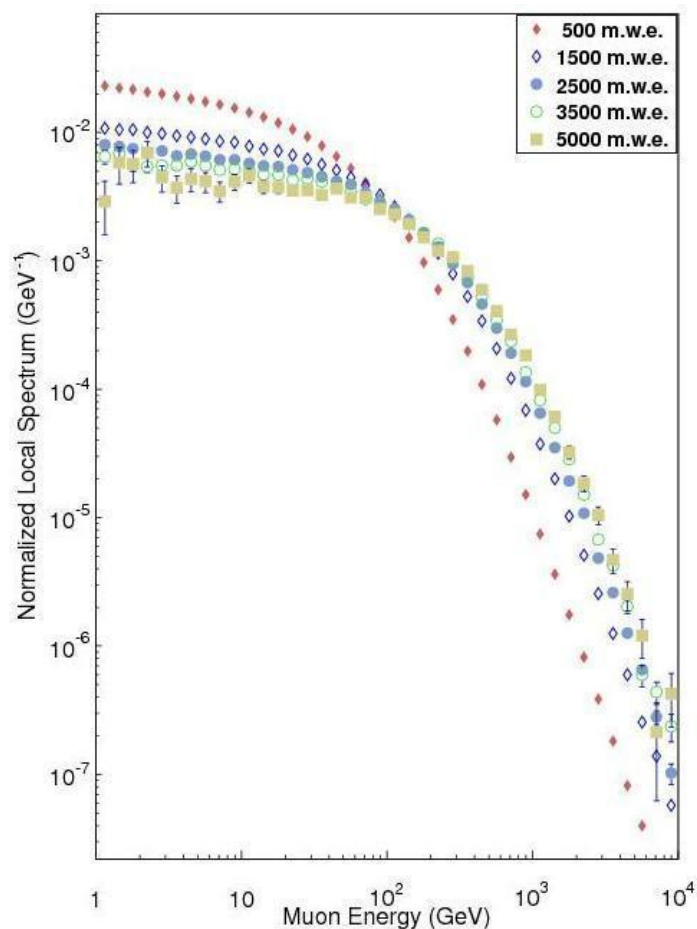


Figure 6.25. The simulated normalized local spectra of the underground muons in various depths of standard rock [209]

It is seen from the figure that the relatively low energy part of the spectrum, especially below ~ 100 GeV, gets flatter with the increase in depth such that the normalized local spectra become almost constant for the levels deeper than 2500 m.w.e. In addition, higher energy parts of the spectra (above ~ 500 GeV) are parallel to the each other and to that of the ground level muon spectrum. It should also be noted that shape of the spectrum seems to become independent of the depth above 2500 m.w.e.

The simulated integral intensities of the underground muons, together with the ones from various experiments [140, 210, 211], are illustrated in Figure 6.26 as a function of depth.

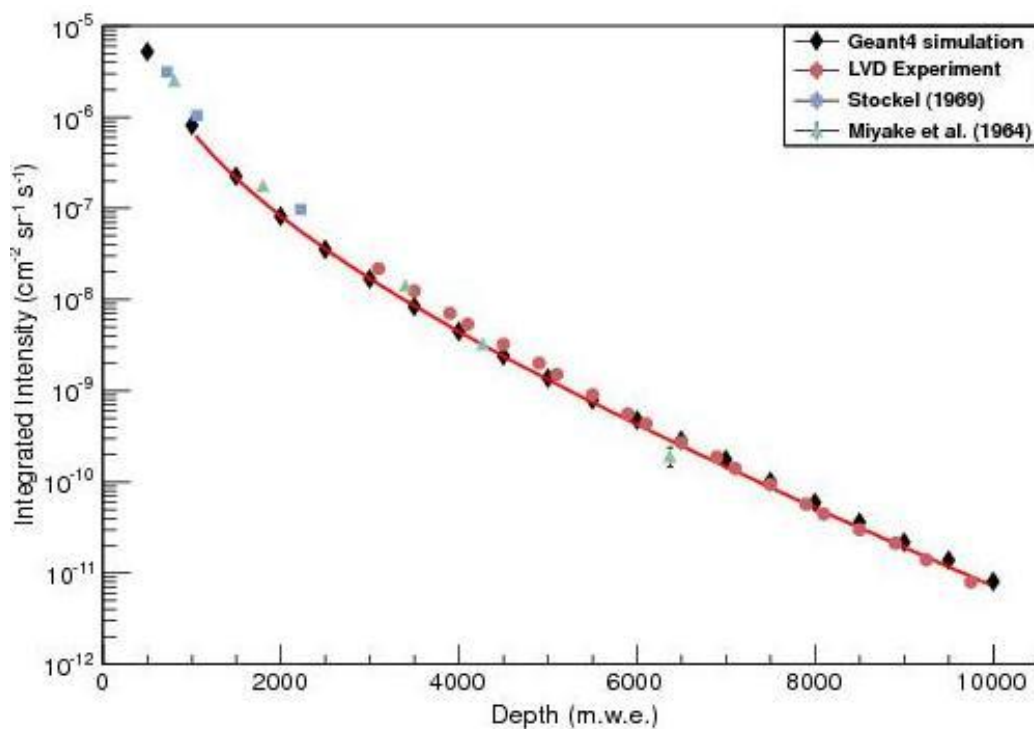


Figure 6.26. Integrated intensity of the underground muons in standard rock as a function of depth [209]

Comparison of the simulated and experimental underground muon intensities indicate that Geant4 simulations are successful in the representation of the depth dependent behavior of the underground muon intensity. The intensity decreases with increasing depth up to the level at which the neutrino induced muons start to dominate. A good agreement between the results of the simulation and those of the

experiments, especially for the depths greater than 4000 m.w.e., draws the attention. For shallower depths, the simulation yields slightly smaller intensities than those from the experiments. In addition, the red line in the figure is the fit curve for the Fréjus function, which is given in Equation 3.10. The parameters A and X_0 , extracted from the fit to the simulation results, are given in Table 6.5 in addition to the ones from various experiments. The reason for the difference between the simulated and experimental fit values is the relatively small discrepancy between the integrated intensities obtained from the simulations and the measurements.

Table 6.5. The experimental and simulated parameters obtained from the fits to the Fréjus function [209]

Experiment	A ($\times 10^{-6} \text{ cm}^{-2} \text{ s}^{-1} \text{ sr}^{-1}$)	X_0 (m.w.e.)
Fréjus 1989 [148]	1.96 ± 0.09	1184 ± 8
Fréjus 1996 [212]	2.18 ± 0.05	1127 ± 4
MACRO 1995 [213]	1.81 ± 0.06	1231 ± 1
LVD 1995 [214]	1.77 ± 0.02	1211 ± 3
Geant4	0.89 ± 0.07	1307 ± 3

6.3.4. Zenith angle dependence of muon intensities in standard rock

Zenith angle dependence of the underground muon intensities in standard rock has been investigated for every 500 m.w.e. up to 6500 m.w.e. depth. The study has been limited by this depth since, at the deeper sites, the cosine power law behavior of the zenith angle distribution is disturbed by the contribution of the neutrino induced muons. The zenith angular distribution of the underground muons at each level has been fit to the function of $m \cos^n \theta$ for $\theta \leq 40^\circ$ and the exponent n has been extracted. The obtained values of n have been plotted in Figure 6.27 as a function of the depth. In the figure are also shown the exponent values from two experiments [140, 210] and a red line that represents the function previously given in Equation 3.12.

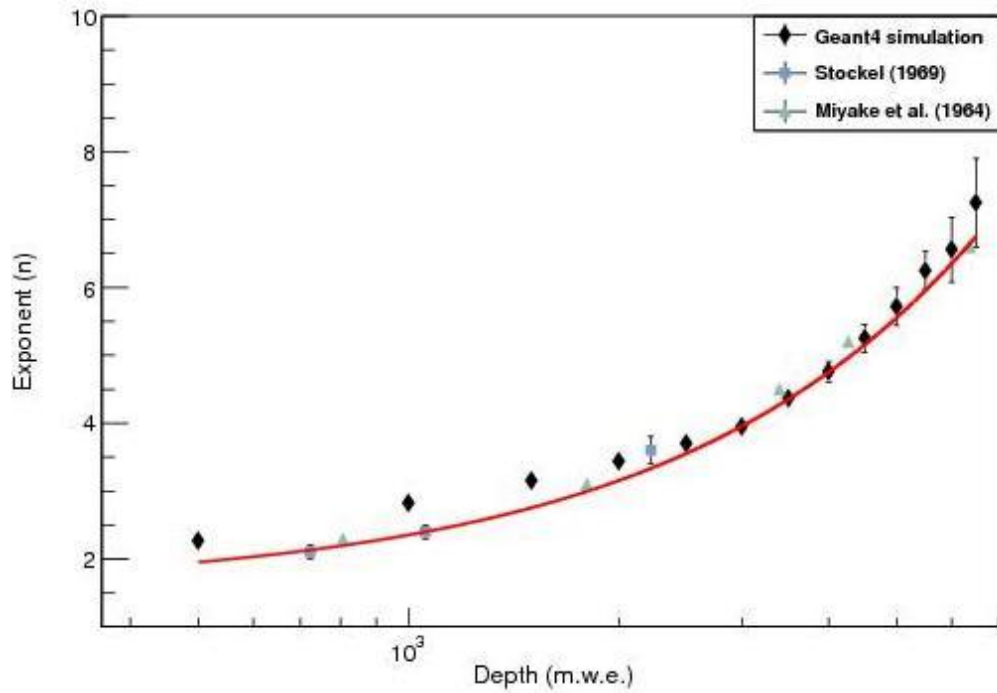


Figure 6.27. The exponent n as a function of the depth in standard rock [209]

By comparing the values obtained from the simulation and the ones from the measurements, one can conclude that the simulation gives very consistent results with the experimental ones, especially above ~ 2000 m.w.e. depth. For shallower depths, the simulation yields slightly larger exponent values than those from the experiments. Moreover, the results of this study are quite compatible with the theoretical curve shown in the figure.

CHAPTER 7. CONCLUSION

In this dissertation, cosmic muon properties in the Earth's atmosphere, at sea level and underground have been investigated using the Geant4 simulation package. Simulation results obtained in each part of the study have been compared with the available experimental ones. In general, very good agreement is seen between the simulation and the experimental results, which confirms the reliability of the models, including the Earth's atmosphere, its crust and physics. Furthermore, the simulations have been extended to investigate the cases that have not been covered by the experiments yet.

Ground level muon spectra for two regions with different cut-off rigidities, Tsukuba and Lynn Lake, have been obtained as the first part of this study. The simulated muon spectra and charge ratios have been found to be in very good agreement with the measurement made by the BESS. Then, the simulated muon spectrum obtained for Lynn Lake has been utilized to estimate the angular and energy distributions for parent primaries of the muons with different energies. Simulation results confirm the expectation that secondary particles produced in the Earth's atmosphere travel almost in the same direction as their parent primaries. For threshold muon energies (E_μ) of 14 GeV and 100 GeV, the median primary energies have been found to be $15.5 E_\mu$ and $11.2 E_\mu$, respectively. In addition, the zenith angle dependence of the integral and differential muon intensities have been investigated for several geomagnetic locations. The exponent in the cosine power law for $E_\mu > 1$ GeV has been found to have the value of $n = 1.95 \pm 0.08$, which is in good agreement with the ones in the literature. The exponent has been determined to decrease with the increasing muon momenta such that it converges to zero for muon momenta above 50 GeV/c. Therefore, the simulation results suggest that the zenith angle dependence almost disappears for the intensities of the muons with momenta between 50 GeV/c and

500 GeV/c. Moreover, the charge ratio for the low energy muons has been found to be the azimuth angle dependent in such a way that it has a larger (smaller) value for the western (eastern) direction compared to the one from the southern or northern azimuth. As the momentum increases, the charge ratio in the western (eastern) direction decreases (increases) and converges to the value for the northern and southern directions.

In addition, the spectrum, charge ratio and zenith angular dependences of muon intensities at various atmospheric depths have also been obtained in this study. Muon flux has been found to have a tendency to increase with the increasing altitude up to 12 – 14 km and then to decrease for greater altitudes. However, no clear correlation between the muon charge ratio and the atmospheric depth has been noticed in this study. Furthermore, the zenith angle dependence of the integrated muon intensities at different atmospheric depths has been investigated for various threshold muon momenta, and the exponent in the cosine power law for each case has been determined. It has been concluded that the exponent decreases with the increase in the altitude in such a way that its diminution is relatively small up to the depth of 600 g cm^{-2} and sharper for greater altitudes.

Lastly, underground muon intensities and their zenith angular dependence have been investigated for underground muons at various depths in salt and standard rock. Geant4 simulation results for the vertical muon fluxes at different levels of a salt mine in Romania are quite compatible with the ones from the measurements and the simulations performed using another simulation program. Results of the simulated zenith angle dependence of the muon intensities at different levels of the mine can possibly be checked against the results to be obtained from the future experiments to be performed at the site. Moreover, the simulated integral intensities up to 10000 m.w.e. and the exponent in the zenith angular distribution up to 6500 m.w.e. in standard rock have been shown to be very consistent with the experimental data reported in the literature.

REFERENCES

- [1] GAISSER, T.K., Cosmic rays and particle physics, Cambridge University Press, USA, 1990.
- [2] BIRD, D.J. et al., Evidence for correlated changes in the spectrum and composition of cosmic rays at extremely high energies, Phys. Rev. Lett., vol. 71, no: 21, 1993.
- [3] The accelerators at CERN, available online at; “<http://home.web.cern.ch/about/accelerators>”, 2014.
- [4] WILSON, C.T.R., On the leakage of electricity through dust-free air, Proc. Cambridge Philos. Soc., vol. 11, 32, 1900.
- [5] ELSTER, J., and GEITEL, H., Weitere versuche über die elektricitäts zerstreung in abgeschlossenen luftmengen (Further experiments on electricity dispersal in enclosed air volumes), Physik. Z., vol. 2, 560–563, 1901.
- [6] WULF, T., Beobachtungen über die strahlung hoher durchdringungsfähigkeit auf dem Eiffelturm (Observations of the radiation of high penetration capacity on the Eiffel tower), Physik. Z., vol. 11, 811-813, 1910.
- [7] De ANGELIS, A., Cosmic Rays: studies and measurements before 1912, Nucl. Phys. B-Proc. Sup., vol. 239–240, 3–10, 2013.
- [8] HESS, V.F., Über Beobachtungen der durchdringenden strahlung bei sieben freiballonfahrten (Observations about the penetrating radiation at seven balloon rides), Physik. Z., vol. 13, 1084-1091, 1912.
- [9] The official web site of the Nobel Prize, available online at; “http://www.nobelprize.org/nobel_prizes/physics/laureates/1936/press.html”, 2014.
- [10] KOLHORSTER, W., Messungen der durchdringenden strahlung im freiballon in größeren höhen (Measurements of the penetrating radiation in a free balloon at higher altitudes), Physik. Z., vol. 14, 1153–1156, 1913.
- [11] WALTER, M., Early cosmic ray research with balloons, Nucl. Phys. B-Proc. Sup., vol. 239–240, 11–18, 2013.

- [12] MILLIKAN, R.A. and CAMERON G.H., High frequency rays of cosmic origin III. measurements in Snow-Fed lakes at high altitudes, *Phys. Rev.*, vol. 28, 851–868, 1926.
- [13] CLAY, J., Penetrating radiation, *Proc. R. Acad. Amsterdam*, 30, 1115–1127, 1930.
- [14] ROSSI, B., On the magnetic deflection of cosmic rays, *Phys. Rev.*, vol. 36, 606–606, 1930.
- [15] JOHNSON, T.H., The azimuthal asymmetry of the cosmic radiation, *Phys. Rev.*, vol. 43, 834–835, 1933.
- [16] ALVAREZ, L. and COMPTON, A. H., A positively charged component of cosmic rays, *Phys. Rev.*, vol. 43, 835–836, 1933.
- [17] ROSSI, B., Directional measurements on the cosmic rays near the geomagnetic equator, *Phys. Rev.*, vol. 45, 212–214, 1934.
- [18] AUGER, P. et al., Extensive cosmic-ray showers, *Rev. Mod. Phys.*, vol. 11, 288–291, 1939.
- [19] SCHEIN, M. et al., The nature of the primary cosmic radiation and the origin of the mesotron, *Phys. Rev.*, vol. 59, 615–615, 1941.
- [20] FREIER, P. et al., Evidence for heavy nuclei in the primary cosmic radiation, *Phys. Rev.*, vol. 74, 213–217, 1948.
- [21] FREIER, P. et al., The heavy component of primary cosmic rays, *Phys. Rev.*, vol. 74, 1818–1827, 1948.
- [22] MEYER, P. and VOGT, R., Electrons in the primary cosmic radiation, *Phys. Rev. Lett.*, vol. 6, 193–196, 1961.
- [23] ANDERSON, C.D., The positive electron, *Phys. Rev.*, vol. 43, 491–494, 1933.
- [24] DIRAC, P.A.M., The quantum theory of the electron, *Proc. R. Soc. Lond. A*, vol. 117, 610–624, 1928.
- [25] GRIFFITHS, D., *Introduction to elementary particles*, WILEY-VCH, Germany, 2004.
- [26] SWORDY, S.P., The energy spectra and anisotropies of cosmic rays, *Space Sci. Rev.*, vol. 99, 85–94, 2001.
- [27] MATTHIAE, G., The cosmic ray energy spectrum as measured using the Pierre Auger Observatory, *New J. Phys.*, vol. 12, 075009, 2010.

- [28] KULIKOV, G.V. and KHRISTIANSEN, G.B., On the size spectrum of extensive air showers, *Sov. Phys. J. Exp. Theor. Phys. (Zh. Éksp. Teor. Fiz.)*, vol. 35, 635–640, 1958.
- [29] LINSLEY, J., Evidence for a primary cosmic-ray particle with energy 10^{20} eV, *Phys. Rev. Lett.*, vol. 10, 146–148, 1963.
- [30] BIRD, D.J., Evidence for correlated changes in the spectrum and composition of cosmic rays at extremely high energies, *Phys. Rev. Lett.*, vol. 71, 3401–3404, 1993.
- [31] NAKAMURA, K. et al. (Particle Data Group), Review of particle physics, *J. Phys. G: Nucl. Part. Phys.*, vol. 37, 075021, 2010.
- [32] ANTONI, T. et al., KASCADE measurements of energy spectra for elemental groups of cosmic rays: Results and open problems, *Astropart. Phys.*, vol. 24, 1-25, 2005.
- [33] GREISEN, K., End to the cosmic-ray spectrum?, *Phys. Rev. Lett.*, vol. 16, 748–750, 1966.
- [34] ZATSEPIN, G.T. and KUZ'MIN, V.A., Upper limit of the spectrum of cosmic rays, *JETP Letters*, vol. 4, 78–80, 1966.
- [35] AHARONIAN, F.A. and CRONIN, J.W., Influence of the universal microwave background radiation on the extragalactic cosmic-ray spectrum, *Phys. Rev. D*, vol. 50, 1892–1900, 1994.
- [36] BAHCALL, J.N. and WAXMAN, E., Has the GZK suppression been discovered?, *Phys. Lett. B*, vol. 556, 1–6, 2003.
- [37] TAKEDA, M. et al., Energy determination in the Akeno Giant Air Shower Array experiment, *Astropart. Phys.*, vol. 19, 447–462, 2003.
- [38] UBBASI R.U. et al. (High Resolution Fly's Eye Collaboration), First observation of the Greisen-Zatsepin-Kuzmin suppression, *Phys. Rev. Lett.*, vol. 100, 101101, 2008.
- [39] ABRAHAM, J. et al. (The Pierre Auger Collaboration), Observation of the suppression of the flux of cosmic rays above 4×10^{19} eV, *Phys. Rev. Lett.*, vol. 101, 061101, 2008.
- [40] SIMPSON, J.A., Elemental and isotopic composition of the galactic cosmic rays, *Ann. Rev. Nucl. Part. Sci.*, vol. 33, 323–382, 1983.
- [41] WIEBEL-SOOTH, B., Cosmic rays VII. Individual element spectra: prediction and data, *Astron. Astrophys.*, vol. 330, 389–398, 1998.

- [42] ICHIMURA, M. et al., Observation of heavy cosmic-ray primaries over the wide energy range from ~ 100 GeV/particle to ~ 100 TeV/particle: Is the celebrated “knee” actually so prominent?, *Phys. Rev. D*, vol. 48, 1949–1975, 1993.
- [43] BEREZINSKY, V. et al., On astrophysical solution to ultrahigh energy cosmic rays, *Phys. Rev. D*, vol. 74, 043005, 2006.
- [44] BEREZHKO, E.G., Composition of cosmic rays accelerated in active galactic nuclei, *Astrophys. J. Lett.*, vol. 698, L138–L141, 2009.
- [45] WIEDENBECK, M.E. and GREINER, D.E., A cosmic-ray age based on the abundance of ^{10}Be , *Astrophys. J.*, vol. 239, L139–L142, 1980.
- [46] FRIEDLANDER, M.W., *A thin cosmic rain: Particles from outer space*, Harvard University Press, 40, USA, 2000.
- [47] FORBUSH, S.E., On the effects in cosmic-ray intensity observed during the recent magnetic storm, *Phys. Rev.*, vol. 51, 1108–1109, 1937.
- [48] FERMI, E., On the origin of the cosmic radiation, *Phys. Rev.*, vol. 75, 1169–1174, 1949.
- [49] ACKERMANN, M., Detection of the characteristic pion-decay signature in supernova remnants, *Science*, vol. 339, no. 6121, 807–811, 2013.
- [50] COCCONI, G., Intergalactic space and cosmic rays, *Il Nuovo Cimento*, series 10, vol. 3, issue 6, 1433–1442, 1956.
- [51] HORANDEL, J.R., Cosmic rays at the highest energies, *Prog. Part. Nucl. Phys.*, vol. 64, 351–359, 2010.
- [52] HORANDEL, J.R., The origin of galactic cosmic rays, *Nucl. Instrum. Meth. A*, vol. 588, 181–188, 2008.
- [53] PFOTZER, G., Dreifachkoinzidenzen der ultrastrahlung aus vertikaler richtung in der stratosphäre (Triple coincidences of cosmic rays from the vertical direction in the stratosphere), *Physik. Z.*, vol. 102, 23–40, 1936.
- [54] ZATSEPIN, G.T. and ROGANOVA, T.M., Cosmic ray investigations, *Phys.-Usp.*, vol. 52, no. 11, 1139–1146, 2009.
- [55] BERINGER, J. et al. (Particle Data Group), Review of particle physics, *Phys. Rev. D*, vol. 86, 010001, 2012.
- [56] WEBBER, W.R., Sudden intensity increases and radial gradient changes of cosmic ray MeV electrons and protons observed at Voyager 1 beyond 111 AU in the heliosheath, arXiv:1112.3590 [physics.space-ph], 2011.

- [57] PARKER, E.N., *Interplanetary dynamical processes*, Interscience Monographs and Texts in Physics and Astronomy, John Wiley and Sons New York – London, 1963.
- [58] OWENS, M.J. and FORSYTH, R.J., *The heliospheric magnetic field*, *Living Rev. Solar Phys.*, vol. 10, 5, 2013.
- [59] MAVROMICHALAKI, H. et al., *Athens Neutron Monitor Data Processing Center – ANMODAP Center*, *Adv. Space Res.*, vol. 44, 1237–1246, 2009.
- [60] MORAAL, H., *Cosmic ray modulation studies in the outer heliosphere*, *Nucl. Phys. B-Proc. Sup.*, vol. 33, 161–178, 1993.
- [61] SCHWABE, M., *Die Sonne. Von Herrn Hofrath Schwabe (The Sun. From Mr. Councilor Schwabe)*, *Astron. Nachrichten*, vol. 20, 283–286, 1843.
- [62] KANE, R.P., *Some implications using the group sunspot number reconstruction*, *Sol. Phys.*, vol. 205, 383–401, 2002.
- [63] HOWE, R. et al., *A note on the torsional oscillation at solar minimum*, *Astrophys. J. Lett.*, vol. 701, L87–L90, 2009.
- [64] HALE, G.E. and NICHOLSON, S.B., *The law of Sun-spot polarity*, *Astrophys. J.*, vol. 62, 270–300, 1925.
- [65] VAN ALLEN, J.A., *On the modulation of galactic cosmic ray intensity during solar activity cycles 19, 20, 21, 22 and early 23*, *Geophys. Res. Lett.*, vol. 27, 2453–2456, 2000.
- [66] SINGH, M. et al., *Solar modulation of galactic cosmic rays during the last five solar cycles*, *J. Atmos. Sol.-Terr. Phys.*, vol. 70, 169–183, 2008.
- [67] PICOZZA, P., et al., *Cosmic ray study with the PAMELA experiment*, *J. Phys.: Conf. Ser.*, vol. 409, 012003, 2013.
- [68] GARRET, H., *Guide to modeling Earth’s trapped radiation environment*, Atmospheric and Space Environments Committee on Standards, USA, 1999.
- [69] SMART, D.F. and SHEA, M.A., *Geomagnetic cut-offs: A review for space dosimetry applications*, *Adv. Space Res.*, vol. 36, issue 10, 787–796, 1994.
- [70] CASOLINO, M. et al., *Two years of flight of the Pamela experiment: Results and perspectives*, *J. Phys. Soc. Jpn.*, vol. 78, 35–40, 2009.
- [71] *United Nations Scientific Committee on the Effects of Atomic Radiation, Sources and Effects of Ionizing Radiation, UNSCEAR 2008 report*, United Nations Publications, USA, 2008.

- [72] VUKOVIĆ, B. et al., Measurements of the dose due to cosmic rays in aircraft, *Nucl. Instrum. Meth. A*, vol. 562, 517–520, 2006.
- [73] CUCINOTTA, F.A., Space radiation organ doses for astronauts on past and future missions, NASA Technical Reports Server, Document ID: 20070010704, 2007.
- [74] FUJITAKA, K., High-level doses brought by cosmic rays, *Int. Congr. Ser.*, vol. 1276, 124–128, 2005.
- [75] RAFNSSON, V. et al., Cosmic radiation increases the risk of nuclear cataract in airline pilots: A population-based case-control study, *JAMA Archives of Ophthalmology*, vol. 123, 1102-1105, 2005.
- [76] KRANE, K.S., *Introductory nuclear physics*, John Wiley and Sons Inc., USA, 1987.
- [77] SVENSMARK, H., Influence of cosmic rays on Earth's climate, *Phys. Rev. Lett.*, vol. 81, 5027–5030, 1998.
- [78] SLOAN, T. and WOLFENDALE, A.W., Testing the proposed causal link between cosmic rays and cloud cover, *Environ. Res. Lett.*, vol. 3, 024001, 2008.
- [79] GUREVICH, A.V. et al., Kinetic theory of runaway breakdown in inhomogeneous thundercloud electric field, *Phys. Lett. A*, vol. 282, 180–185, 2001.
- [80] ZIEGLER, J.F. and LANFORD, W.A., Effect of cosmic rays on computer memories, *Science*, vol. 206, 776-788, 1979.
- [81] ADAMS, L., Cosmic ray effects in microelectronics, *Microelectron. J.*, vol. 16, 17–29, 1985.
- [82] SCHLAEPFER, H., *Cosmic Rays*, (SPATIUM) International Space Science Institute, no11, 2003.
- [83] SCHRIMPF, R.D. et al., Radiation effects in new materials for nano-devices, *Microelectron. Eng.*, vol. 88, 1259–1264, 2011.
- [84] GEORGE, E.P., Cosmic rays measure overburden of tunnel, *Commonwealth Engineer*, July 1, 455–457, 1955.
- [85] ALVAREZ, L.W. et al., Search for hidden chambers in the pyramids, *Science*, vol. 167, 832–839, 1970.
- [86] NAGAMINE, K., Geo-tomographic observation of inner-structure of volcano with cosmic-ray muons, *J. of Geography*, vol. 104, 998–1007, 1995.

- [87] TANAKA, H.K.M. et al., Detecting a mass change inside a volcano by cosmic-ray muon radiography (muography): First results from measurements at Asama volcano, Japan, *Geophys. Res. Lett.*, vol. 36, L17302, 2009.
- [88] BOROZDIN, K. et al., Cosmic ray radiography of the damaged cores of the Fukushima Reactors, *Phys. Rev. Lett.*, vol. 109, 152501, 2012.
- [89] LEE, H.S. et al., Development of a cosmic-ray muon radiography system with plastic scintillators, *J. Korean Phys. Soc.*, vol. 54, 2076–2081, 2009.
- [90] GAISSER, T.K. and HONDA, M., Flux of atmospheric neutrinos, *Ann. Rev. Nucl. Part. Sci.*, vol. 52, 153–199, 2002.
- [91] YUKAWA, H., On the Interaction of elementary particles, *Proc. Phys. Math. Soc. Jap.*, vol. 17, 48, 1935.
- [92] NEDDERMEYER, S.H. and ANDERSON, C. D., Note on the nature of cosmic-Ray particles , *Phys. Rev.*, vol. 51, 884–886, 1937.
- [93] STREET, J.C. and STEVENSON, E.C., New evidence for the existence of a particle of mass intermediate between the proton and electron, *Phys. Rev.*, vol. 52, 1003–1004, 1937.
- [94] NEDDERMEYER, S.H. and ANDERSON, C. D., Cosmic-ray particles of intermediate mass, *Phys. Rev.*, vol. 54, 88–89, 1938.
- [95] ROSSI, B., The Disintegration of Mesotrons, *Rev. Mod. Phys.*, vol. 11, 296–303, 1939.
- [96] WILLIAMS, E. J. and ROBERTS, G. E., Evidence for transformation of mesotrons into electrons, *Nature*, vol. 145, 102-103, 1940.
- [97] RASETTI, F., Disintegration of slow mesotrons, *Phys. Rev.*, vol. 60, 198–204, 1941.
- [98] MILLIKAN, R.A., Mesotron as the name of the new particle, *Phys. Rev.*, vol. 55, 105–105, 1939.
- [99] BHABHA, H.J., The Fundamental length introduced by the theory of the Mesotron (Meson)*, *Nature*, vol. 143, 276–277, 1939.
- [100] CONVERSI, M., PANCINI, E., and PICCIONI, O., On the disintegration of negative mesons, *Phys. Rev.*, vol. 71, 209–210 ,1947.
- [101] FERMI, E., TELLER, E. and WEISSKOPF, V., The decay of negative mesotrons in matter , *Phys. Rev.*, vol. 71, 314–315 ,1947.

- [102] MARSHAK, R.E. and BETHE, H.A., On the Two-Meson Hypothesis, *Phys. Rev.*, vol. 72, 506–509, 1947.
- [103] LATTES, C.M.G., OCCHIALINI, G.P.S. and POWELL, C.F., Observations on the tracks of slow mesons in photographic emulsions*, *Nature*, vol. 160, 453–456, 1947.
- [104] BROWN, R. et al., observations with electron-sensitive plates exposed to cosmic radiation, *Nature*, vol. 163, 47–51, 1949.
- [105] The official web site of the Nobel Prize, available online at; “http://www.nobelprize.org/nobel_prizes/physics/laureates/1949/press.html”, 2014.
- [106] BARDON, M. et al., Measurement of the momentum spectrum of positrons from muon decay, *Phys. Rev. Lett.*, vol. 14, 449–453, 1965.
- [107] HUGHES, V.W. et al., Formation of Muonium and observation of its Larmor Precession, *Phys. Rev. Lett.*, vol. 5, 63–65, 1960.
- [108] MEASDAY, D.F., The nuclear physics of muon capture, *Phys. Rep.*, vol. 354, 243–409, 2001.
- [109] ROSSI, B., *High-energy particles*, Prentice–Hall, New York – USA, 1952.
- [110] SUZUKI, T. et al., Total nuclear capture rates for negative muons, *Phys. Rev. C*, vol. 35, 2212–2224, 1987.
- [111] CECCHINI, S. and SPURIO, M., Atmospheric muons: experimental aspects, arXiv:1208.1171 [astro-ph.EP], 2012.
- [112] GROOM, D.E. et al., Muon stopping power and range tables 10 MeV – 100 TeV, *Atomic Data and Nuclear Data Tables*, vol. 78, 183–356, 2001.
- [113] ROSSI, B. and HALL D.B., Variation of the rate of decay of mesotrons with momentum, *Phys. Rev.*, vol. 59, 223, 1941.
- [114] FRISCH, D.H. and SMITH, J.H., Measurement of the relativistic time dilation using μ -mesons, *Am. J. Phys.*, vol. 31, 342–355, 1963.
- [115] De PASCALE, M.P. et al., Absolute spectrum and charge ratio of cosmic ray muons in the energy region from 0.2 GeV to 100 GeV at 600 m above sea level, *J. Geophys. Res.*, vol. 98, 3501–3507, 1993.
- [116] RASTIN, B.C., An accurate measurement of the sea-level muon spectrum within the range 4 to 3000 GeV/c, *J. Phys. G: Nucl. Phys.*, vol. 10, 1609–1628, 1984.

- [117] GAISSER, T.K., Outstanding problems in particle astrophysics, arXiv: astro-ph/0501195, 2005.
- [118] AJIMA, Y. et al. (BESS Collaboration), A superconducting solenoidal spectrometer for a balloon-borne experiment, *Nucl. Instrum. Meth. A*, vol. 443, 71–100, 2000.
- [119] MOTOKI, M. et al., Precise measurements of atmospheric muon fluxes with the BESS spectrometer, *Astropart. Phys.*, vol. 19, 113–126, 2003.
- [120] FUTAGAMI, T. et al. (Super-Kamiokande Collaboration), Observation of the East-West anisotropy of the atmospheric neutrino flux, *Phys. Rev. Lett.*, vol. 82, 5194–5197, 1999.
- [121] LIPARI, P., The East–West effect for atmospheric neutrinos, *Astropart. Phys.*, vol. 14, 171–188, 2000.
- [122] DIEP, P.N. et al., Measurement of the East–West asymmetry of the cosmic muon flux in Hanoi, *Nucl. Phys. B*, vol. 678, 3–15, 2004.
- [123] TSUJI, S. et al., Measurements of muons at sea level, *J. Phys. G: Nucl. Part. Phys.*, vol. 24, 1805–1822, 1998.
- [124] ACHARD, P. et al. (L3 Collaboration), Measurement of the atmospheric muon spectrum from 20 to 3000 GeV, *Phys. Lett. B*, vol. 598, 15–32, 2004.
- [125] RASTIN, B.C., A study of the muon charge ratio at sea level within the momentum range 4 to 2000 GeV/c, *J. Phys. G: Nucl. Phys.*, vol. 10, 1629–1638, 1984.
- [126] ADAMSON, P. et al. (MINOS Collaboration), Measurement of the atmospheric muon charge ratio at TeV energies with the MINOS detector, *Phys. Rev. D*, vol. 76, 052003, 2007.
- [127] WADA, T. et al., Atmospheric muon measurements using the OKAYAMA telescope, *Nucl. Phys. B-Proc. Sup.*, vol. 151, 465–468, 2006.
- [128] CRITCHFIELD, C.L. et al., Soft Radiation at balloon altitudes, *Phys. Rev.*, vol. 85, 461–467, 1952.
- [129] CONVERSI, M., Experiments on cosmic-ray mesons and protons at several altitudes and latitudes, *Phys. Rev.*, vol. 79, 749–, 1950.
- [130] QUERCIA, I.F. and RISPOLI, B., Altitude and geomagnetic effects of positive and negative penetrating particles of cosmic radiation, *Il Nuovo Cimento*, vol. 10, issue 8, 1142–1171, 1953.

- [131] BOEZIO, M. et al., Energy spectra of atmospheric muons measured with the CAPRICE98 balloon experiment, *Phys. Rev. D*, vol. 67, 072003, 2003.
- [132] BOEZIO, M. et al., Measurement of the flux of atmospheric muons with the CAPRICE94 apparatus, *Phys. Rev. D*, vol. 62, 032007, 2000.
- [133] BELLOTTI, R. et al., Balloon measurements of cosmic ray muon spectra in the atmosphere along with those of primary protons and helium nuclei over midlatitude, *Phys. Rev. D*, vol. 60, 052002, 1999.
- [134] BASINI, G. et al., Measurement of the cosmic ray muon spectrum and charge ratio in the atmosphere from ground level to balloon altitudes, 24th International Cosmic Ray Conference, vol. 1, 585–588, 1995.
- [135] CIRCELLA, M. et al. (WiZard Collaboration), The WiZard collaboration cosmic ray muon measurements in the atmosphere, *Nucl. Phys. B-Proc. Sup.*, vol. 85, 355–360, 2000.
- [136] COUTU, S. et al., Energy spectra, altitude profiles, and charge ratios of atmospheric muons, *Phys. Rev. D*, vol. 62, 032001, 2000.
- [137] BEATTY, J.J. et al., New measurement of the altitude dependence of the atmospheric muon intensity, *Phys. Rev. D*, vol. 70, 092005, 2004.
- [138] BERGER, Ch. et al., The Fréjus nucleon decay detector, *Nucl. Instrum. Meth. A*, vol. 262, 463–495, 1987.
- [139] AMBROSIO, M. et al. (MACRO Collaboration), High energy cosmic ray physics with underground muons in MACRO. I. Analysis methods and experimental results, *Phys. Rev. D*, vol. 56, 1407–1417, 1997.
- [140] MIYAKE, S. et al., Cosmic-ray intensity measurements deep underground at depths of (800÷8400) m.w.e., *Il Nuovo Cimento, Series 10*, vol. 32, 1505–1523, 1964.
- [141] CASTAGNOLI, C. et al., Measurements on the cosmic radiation intensity in the Mont Blanc Tunnel, *Il Nuovo Cimento, Series 10*, vol. 35, 969–976, 1965.
- [142] RUDDICK, K., Some notes on underground muons, *PDK Notes*, no: 435, 1990.
- [143] BARRETT, P.H. et al., Interpretation of cosmic-ray measurements far underground, *Rev. Mod. Phys.*, vol. 24, 133–178, 1952.
- [144] REINES, F. et al., Evidence for high-energy cosmic-ray neutrino interactions, *Phys. Rev. Lett.*, vol. 15, 429–433, 1965.

- [145] ACHAR, C.V. et al., Detection of muons produced by cosmic ray neutrinos deep underground, *Phys. Lett.*, vol. 18, 196–199, 1965.
- [146] CROUCH, M.F. et al, Cosmic-ray muon fluxes deep underground: Intensity vs depth, and the neutrino-induced component, *Phys. Rev. D*, vol. 18, 2239–2252, 1978.
- [147] GAISSER, T.K. and STANEV, T., Neutrino-induced muon flux deep underground and search for neutrino oscillations, *Phys. Rev. D*, vol. 30, 985–990, 1984.
- [148] BERGER, Ch. et al. (Fréjus Collaboration), Experimental study of muon bundles observed in the Fréjus detector, *Phys. Rev. D*, vol. 40, 2163–2171, 1989.
- [149] GIUSTI, P. et al. (LVD Collaboration), Atmospheric single muon flux measured over five decades of intensity by LVD at Gran Sasso laboratory, 24th International Cosmic Ray Conference, vol. 1, 548–551, 1995.
- [150] CASSIDAY, G.L. et al., Calculation of the stopping-muon rate underground, *Phys. Rev. D*, vol. 7, 2022–2031, 1973.
- [151] MENON, M.G.K. et al., Muon intensities and angular distributions deep underground, *Proc. Phys. Soc.*, vol. 90, 649–656, 1967.
- [152] CROOKES, J.N. and RASTIN, B.C., The absolute intensity of muons at 31.6 hg cm⁻² below sea-level, *Nucl. Phys. B*, vol. 58, 93–109, 1973.
- [153] BADGER, L., Lazzarini's Lucky Approximation of π , *Math. Mag.*, vol. 67, 83–91, 1994.
- [154] METROPOLIS, N., The beginning of the Monte Carlo method, *Los Alamos Science*, Special Issue vol. 15, 125-130, 1987.
- [155] METROPOLIS, N. and ULAM, S., The Monte Carlo Method, *J. Am. Statist. Assoc.*, vol. 44, 335–341, 1949.
- [156] ECKHARDT, R., Stan Ulam, John von Neumann, and the Monte Carlo method, *Los Alamos Science*, Special Issue vol. 15, 131-137, 1987.
- [157] BIELAJEW, A.F., Fundamentals of the Monte Carlo method for neutral and charged particle transport, The University of Michigan, USA, 2001.
- [158] BATTISTONI, G. et al., The FLUKA code: Description and benchmarking, *AIP Conference Proceeding*, vol. 896, 31–49, 2007.
- [159] MCNP web site, available online at;

- “<https://mcnp.lanl.gov>”, 2014.
- [160] AGOSTINELLI, S. et al., Geant4—a simulation toolkit, *Nucl. Instrum. Meth. A*, vol. 506, 250–303, 2003.
- [161] ALLISON, J. et al., Geant4 developments and applications, *IEEE T. Nucl. Sci.*, vol. 53, 270–278, 2006.
- [162] GIANI, S. et al., Geant4: An object-oriented toolkit for simulation in HEP, CERN Report CERN-LHCC-98-044, Geneva, Switzerland, 1998.
- [163] BRUN, R. et al., GEANT detector description and simulation tool, CERN Program Library Long Write-up W5013, CERN, Geneva, Switzerland, 1993.
- [164] Geant4 web site, available online at; “<http://geant4.cern.ch>”, 2014.
- [165] APOSTOLAKIS, J. et al., Geometry and physics of the Geant4 toolkit for high and medium energy applications, *Radiat. Phys. Chem.*, vol. 78, 859–873, 2009.
- [166] IVANCHENKO, V.N., Geant4: physics potential for HEP instrumentation, *Nucl. Instrum. Meth. A*, vol. 494, 514–519, 2002.
- [167] APOSTOLAKIS, J. et al., Progress in hadronic physics modelling in Geant4, *J. Phys.: Conf. Ser.*, vol. 160, 012073, 2009.
- [168] IVANCHENKO, V. et al. Hadronic physics in Geant4: Improvements and status for LHC start, *PoS (ACAT08) 111*, 2008.
- [169] APOSTOLAKIS, J. et al., Geant4 Physics Lists for HEP, Nuclear Science Symposium Conference Record 2008 (NSS 08), 833–836, 2008.
- [170] YARBA, J. (on behalf of the Geant4 Hadronic Group), Recent developments and validation of Geant4 hadronic physics, *J. Phys.: Conf. Ser.*, vol. 396, 022060, 2012.
- [171] BANERJEE, S. (on behalf of Geant4 Hadronic Group), Validation of Geant4 hadronic physics models at intermediate energies, *J. Phys.: Conf. Ser.*, vol. 219, 032002, 2010.
- [172] LUTGENS, F.K., TARBUCK, E.J. and TASA, D., *The Atmosphere: An introduction to meteorology* (12th Edition), Pearson Education, USA, 2013.
- [173] BEAMER-DOWNIE, D., Considering the unthinkable—A review and discussion of current international law and suggestions regarding how we deal with a catastrophic incident in space, *Acta Astronautica*, vol. 92, 255–262, 2013.

- [174] NASA, U.S. Standard Atmosphere, U.S. Government Printing Office, Washington D.C., 1976.
- [175] FINLAY, C.C. et al., International Geomagnetic Reference Field: the eleventh generation, *Geophys. J. Int.*, vol. 183, 1216–1230, 2010.
- [176] National Geophysical Data Center Magnetic Field Calculator: available online at; “<http://www.ngdc.noaa.gov/geomag-web/#igrfwmm>”, 2014.
- [177] ALEXEYENKO, V.V. et al., Short perturbations of cosmic ray intensity and electric field in atmosphere, *Proceedings of the 19th International Conference on Cosmic Rays*, vol. 5, 352–355, 1985.
- [178] BEKTASOGLU, M. and ARSLAN, H., Estimation of the effects of the Earth's electric and magnetic fields on cosmic muons at sea level by Geant4, *J. Atmos. Sol-Terr. Phys.*, vol. 74, 212–216, 2012.
- [179] REICHENBACHER, J. and DE JONG J., Calculation of the underground muon intensity crouch curve from a parameterization of the flux at surface, *Proceeding of the 30th International Cosmic Ray Conference, Mexico City*, (arXiv:0706.1110), 2007.
- [180] CRISTACHE, C. et al., Epithermal neutrons activation analysis, radiochemical and radiometric investigations of evaporitic deposits of Slanic-Prahova (Romania) salt mine, *Radiochim. Acta*, vol. 97, 333–337, 2009.
- [181] RUBBIA, A., The Laguna design study-towards giant liquid based underground detectors for neutrino physics and astrophysics and proton decay searches, *Acta Phys. Pol. B*, vol. 41, 1727–1732, 2010.
- [182] MARGINEANU, R. et al., The Slanic-Prahova (ROMANIA) underground low-background radiation laboratory, *Appl. Radiat. Isotopes*, vol. 66, 1501–1506, 2008.
- [183] SANUKI, T. et al., Precise measurement of cosmic-ray proton and helium spectra with the BESS Spectrometer, *Astrophys. J.*, vol. 545, 1135–1142, 2000.
- [184] HAINO, S. et al., Measurements of primary and atmospheric cosmic-ray spectra with the BESS-TeV spectrometer, *Phys. Lett. B*, vol. 594, 35–46, 2004.
- [185] ARSLAN, H. and BEKTASOGLU, M., Angular and energy distribution for parent primaries of cosmic muons at sea level using Geant4, *Nucl. Instrum. Meth. A*, vol. 778, 1–5, 2015.

- [186] MITTAL, V.K., VERMA, R.C. and GUPTA, S.C., Introduction to nuclear and particle physics, PHI Learning Pvt. Ltd., New Delhi, 352–353, 2009.
- [187] GAISSER, T.K., Calculation of Muon yields, response functions, and sea level integral energy spectrum using recent accelerator data and Feynman scaling, *J. Geophys. Res.*, vol. 79, 2281–2286, 1974.
- [188] DAS, A.K. and DE, A.K., Coupling functions for muon telescopes at sea level and underground, *J. Phys. G: Nucl. Phys.*, vol. 5, 133–138, 1979.
- [189] ERLYKIN, A.D. et al., Relationship of the spectrum of sea level muons to that of the primary cosmic rays, *J. Phys. A: Math. Nucl. Gen.*, vol. 7, 2074–2084, 1974.
- [190] DAS, A.K. and DE, A.K., Energy distribution of parent nucleons for muons observed at sea level and underground, *J. Phys. G: Nucl. Phys.*, vol. 6, 539–546, 1980.
- [191] BEKTASOGLU, M. and TONGUC, B.T., Estimation of the most probable muon energy at sea level using two-paddle cosmic ray detectors, *Arab. J. Sci. Eng.*, vol. 37, 197–200, 2012.
- [192] BEKTASOGLU, M. and ARSLAN, H., Investigation of the zenith angle dependence of cosmic-ray muons at sea level, *Pramana – J. Phys.*, vol. 80, 837–846, 2013.
- [193] LIN, J.W. et al., Measurement of angular distribution of cosmic-ray muon fluence rate, *Nucl. Instrum. Meth. A*, vol. 619, 24–27, 2010.
- [194] BHATTACHARYYA, D., Absolute sea-level integral muon spectra at zenith angles 45° W and 60° W near the geomagnetic equator in the momentum range (0.4–3) GeV/c, *Il Nuovo Cimento B, Series 11*, vol. 24, 78–84, 1974.
- [195] ARSLAN, H. and BEKTASOGLU, M., Geant4 simulation for the zenith angle dependence of cosmic muon intensities at two different geomagnetic locations, *Int. J. Mod. Phys. A*, vol. 28, 1350071, 2013.
- [196] BHATTACHARYYA, D., Absolute differential sea level muon spectra at zenith angles 45 degrees W and 60 degrees W near the geomagnetic equator, *J. Phys. A: Math. Nucl. Gen.*, vol. 7, 158–166, 1974.
- [197] MORONEY, J.R. and PARRY, J.K., Momentum distribution and charge ratio of μ -mesons at zenith angles in the East-West plane, *Aust. J. Phys.*, vol. 7, 423–438, 1954.

- [198] BRANCUS, I.M. et al., WILLI – a scintillator detector setup for studies of the zenith and azimuth variation of charge ratio and flux of atmospheric muons, Nucl. Phys. B-Proc. Sup., vol. 175–176, 370–373, 2008.
- [199] ARSLAN, H. and BEKTASOGLU, M., Azimuthal angular dependence study of the atmospheric muon charge ratio at sea level using Geant4, J. Phys. G: Nucl. Part. Phys., vol. 39, 055201, 2012.
- [200] MITRICA, B. et al., Investigation of cosmic ray muons with the WILLI detector compared with the predictions of theoretical models and with semi-analytical formulae, Nucl. Phys. B-Proc. Sup., vol. 196, 462–465, 2009.
- [201] BRANCUS, I.M. et al., The East-West effect of the muon charge ratio at energies relevant to the atmospheric neutrino anomaly, Nucl. Phys. A, vol. 721, C1044–C1047, 2003.
- [202] TSUJI, S. et al., Measurements of muons at sea level, J. Phys. G: Nucl. Part. Phys., vol. 24, 1805–1822, 1998.
- [203] HECK, D. et al., CORSIKA: A Monte Carlo program to simulate extensive air showers, Forschungszentrum Karlsruhe Report FZKA, 6019, 1998.
- [204] BELLOTTI, R. et al., Measurement of the negative muon spectrum between 0.3 and 40 GeV/c in the atmosphere, Phys. Rev. D, vol. 53, 35–43, 1996.
- [205] BEKTASOGLU, M. and ARSLAN, H., Simulation of the zenith angle dependence of cosmic muon intensity in slanic salt mine with Geant4, Rom. J. Phys., vol. 59, number 1–2, 131–139, 2014.
- [206] BEKTASOGLU, M., ARSLAN, H. and STANCA, D., Simulations of muon flux in Slanic Salt Mine, Adv. High Energy Phys., vol. 2012, article ID 751762, 2012.
- [207] MITRICA, B. et al., A mobile detector for measurements of the atmospheric muon flux in underground sites, Nucl. Instrum. Meth. A, vol. 654, 176–183, 2011.
- [208] KUDRYAVTSEV, V.A., Muon simulation codes MUSIC and MUSUN for underground physics, Comput. Phys. Commun., vol. 180, 339–346, 2009.
- [209] ARSLAN, H. and BEKTASOGLU, M., Geant4 Simulation Study of Deep Underground Muons: Vertical Intensity and Angular Distribution, Adv. High Energy Phys., vol. 2013, article ID 391573, 2013.
- [210] STOCKEL, C.T., A study of muons deep underground. I. Angular distribution and vertical intensity, J. Phys. A: Gen. Phys., vol. 2, 639–649, 1969.

- [211] AGLIETTA, M. et al. (LVD Collaboration), Muon “depth-intensity” relation measured by the LVD underground experiment and cosmic-ray muon spectrum at sea level, *Phys. Rev. D*, vol. 58, 092005, 1998.
- [212] RHODE, W. et al. (Fréjus Collaboration), Limits on the flux of very high energy neutrinos with the Fréjus detector, *Astropart. Phys.*, vol. 4, 217–225, 1996.
- [213] AMBROSIO, M. et al. (MACRO Collaboration), Vertical muon intensity measured with MACRO at the Gran Sasso laboratory, *Phys. Rev. D*, vol. 52, 3793–3802, 1995.
- [214] AGLIETTA, M. et al. (LVD Collaboration), Neutrino-induced and atmospheric single-muon fluxes measured over five decades of intensity by LVD at Gran Sasso Laboratory, *Astropart. Phys.*, vol. 3, 311–320, 1995.

RESUME

Halil ARSLAN (born in K.Maras, Turkey) graduated from S. Demirel Science High School in 1998 and the Physics Department of Bogazici University in 2003. After the graduation, he has worked as a physics teacher at various private education institutions for six years. In 2009, he was accepted as a teaching assistant by the Department of Physics at Sakarya University. He received master's degree in physics in 2011 with a thesis entitled "Investigation of the effect of the Earth's electric and magnetic fields on cosmic muon flux using Geant4" and was enrolled in the Doctor of Philosophy Program of the department in the same year under supervision of Prof. Mehmet Bektasoglu.